Investigating carrier-based methods and permeabilization strategies to efficiently deliver extracellular cargo into stem cells

By

Saman Modaresi

Submitted to the Bioengineering program and the Graduate Faculty of the University of Kansas in partial fulfillment of the degree requirements for the degree of Doctor of Philosophy

Committee members:

Dr. Stevin Gehrke, Committee chair

Dr. Arghya Paul, Co-Chair

Dr. Cory Berkland

Dr. Sara Wilson

Dr. Andras Czirok

July 31, 2019

Date Defended

The Dissertation Committee for Saman Modaresi certifies that this is the approved version of the following dissertation:

Investigating carrier-based methods and permeabilization strategies to efficiently deliver extracellular cargo into stem cells

Committee Chair

Dr. Stevin Gehrke, Committee Chair

Dr. Arghya Paul, Co-Chair

Date Approved

ABSTRACT

Intracellular delivery of extracellular cargo into stem cells is an active area of research with enormous potential in field of regenerative medicine. Different types of cargo can be delivered, including genetic materials (DNA, RNA, siRNA), proteins, and small molecules that are not permeable to the cell membrane. Based on the macromolecule delivered, it is possible to directly control stem cell gene expression, activate specific intracellular pathways, or induce the secretion of therapeutic growth factors. Over the years, several strategies have been investigated to promote efficient internalization of external cargos, and they can be subdivided into two main groups according to the method of delivery. In the first category, we commonly include carrier-based approaches where the physical and chemical properties of the carrier dictate the route of internalization and the delivery efficiency. Aside from the carrier, the cell microenvironment can also impact the process of internalization when using these strategies. Additionally, several parameters such as chemistry, stiffness, and topography of the cell-substrate need to be properly selected for efficient delivery of the external cargo.

The second group consists of all the other possible carrier-free based strategies that aim to promote intracellular delivery by increasing the permeability of the cell membrane. Transient pores can be induced in the cell membrane by using different physical and mechanical methods that enable the passive diffusion of extracellular cargo. In this case, the method of permeabilization should not be harmful to the cell and should not elicit any permanent damage to the plasma membrane.

Based on these scientific premises, which will be discussed in detail in **Chapter 1**, the aim of this thesis was to investigate both types of delivery methods to identify novel approaches for effective intracellular delivery of genes as well as small polar molecules into stem cells using human adipose-derived stem cells (hASCs) as a model cell line. The overall work of this thesis is

subdivided into two separate sections based on the strategy adopted for the delivery of the external cargo.

The first part of the thesis, discussed in **Chapter 2**, aimed to investigate the modulatory role of substrate stiffness in the transfection of stem cells by using conventional lipid-based carriers complexed with plasmid DNA (lipoplexes). Precisely, we investigated whether the changes in cellular morphology and cytoskeletal rearrangement, induced by a variation in the stiffness of the cell-substrate, had any significant impact on the process of transfection. The findings of this work are important to advance the understanding of how the physical properties of the cell microenvironment can be controlled to enhance the efficacy of conventional carrier-based strategies for the transfection of stem cells.

The second part of the thesis, discussed in **Chapter 3** and **4**, was focused on the design of a novel carrier-free approach for the intracellular delivery of small polar molecules, such as trehalose. Trehalose is a cryoprotecting agent (CPA) that could be used as a replacement of more toxic molecules such as dimethylsulfoxide (DMSO). However, the poor permeability of trehalose through cell membranes limits its applicability as a CPA for stem cell banking applications. Therefore, to promote efficient intracellular delivery of trehalose, we fabricated and optimized a microfluidic device that could create temporary pores in the cell membranes to enable the uptake of extracellular cargo without the use of any carrier. The safety and efficiency of this new platform were tested by studying several parameters, including cell viability, apoptosis, cellular morphology, and differentiation potential of hASCs loaded with trehalose after cryopreservation. Overall, the results and findings of this final section of the thesis provide a novel valuable strategy for the internalization of trehalose to promote efficient cryopreservation of stem cells without the use of DMSO.

TABLE OF CONTENTS

LIST OF FIGURES

Chapter 1.

Chapter 2.

Chapter 3.

Chapter 4.

LIST OF TABLES

Chapter 2.

Chapter 3.

LIST OF ABBREVIATIONS

Abl tyrosine kinases-1 (ABL1)
actin (ACTA1)
adeno-associated viruses (AAV)
alkaline phosphatase (ALP)
basic fibroblast growth factor (bFGF)
bovine serum albumin (BSA)
bovine serum albumin (BSA)
carbon nanotubes (CNT)
caveolin 1 (CAV1)
Chinese hamster ovary (CHO-K1)
Clustered regularly interspaced palindromic repeats-CRISPR associated protein 9 (CRISPR-Cas9)
cryoprotecting agent (CPA)
Cytochalasin D (Cyto D)
Dextran Fluorescein Isothiocyanate (Dex-FITC)
Diamidino-2-phenylindole dilactate (DAPI)
dimethyl sulfoxide (DMSO)
dioleoyl phosphatidylethanolamine (DOPE)
dioleoyl-phosphatidylethanolamine (DOPE)
Dulbecco's Modified Eagle Medium (DMEM)
dynamic light scattering (DLS)
1,2-dioleoyl-3-trimethylammonium propane (DOTAP)

enhanced green fluorescent protein (EGFP)
extracellular matrix (ECM)
fetal bovine serum (FBS)
Filamin A (FLNA)
focal adhesion kinases (FAK)
Fourier transform traction microscopy (FTTM)
glucose-6-phosphate (G6P)
glucose-6-phosphate dehydrogenase (G6P-DH)
Green fluorescent protein (GFP)
hexamethyldisilazane (HMDS)
human adipose-derived stem cells (hASCs)
human mesenchymal stem cells (hMSCs)
Human umbilical vein endothelial cells (HUVECs)
hyaluronic acid (HA)
lipoprotein lipase (LPL), adipocyte protein 2 (aP2)
mean fluorescent intensity (MFI)
Minimum essential medium alpha modification (α-MEM)
multivesicular bodies (MVBs)
myosin II (MYH2)
nicotinamide-adenine dinucleotide phosphate (NADPH)
peroxisome proliferator-activated receptor gamma-2 (PPARγ-2)
phosphate buffered saline (PBS)
poly(ethylenimine) (PEI)
Poly(l-lysine) (PLL)
poly(methylmethacrylate) (PMMA)
polydimethylsiloxane (PDMS)
polyethylene glycol (PEG)
polymeric self-assembled monolayers (SAMs)
polyurethane (PU)
propidium iodide (PI)
quantum dots (QDs),
Ras homolog gene family member A (RhoA)
reticuloendothelial system (RES)
severe combined immunodeficiency (SCID)
transporter 1 (TRET 1)
Trehalose fluorescein isothiocyanate (Trehalose-FITC)
trimethylchlorosilane (TMCS)
vascular endothelial growth factor (VEGF)
β1 Integrin (ITGB1)

CHAPTER 1. Introduction to the thesis

1. Background

The plasma membrane is a selective barrier that defines the cell boundaries and maintains a precise balance between the cytoplasm and the extracellular environment. It is essentially composed of a lipid bilayer that provides the basic fluid structure, which is generally permeable to gases, and few solvents such as water, ethanol, and dimethylsulfoxide. The permeability across the membrane strictly depends on the properties of the membrane such as thickness, lipid composition, presence of proteins, as well as the size and charge of the cargo delivered [1, 2].

The functions of the cell membrane are dictated by its structure and basic components. The main categories of lipids commonly found in the plasma membrane are glycerophospholipids, sphingolipids, and sterols. Cholesterol is the main sterol present in the plasma membranes of mammalian cells that serves the role as a filler to stiffen and thicken the plasma membrane [3]. The lipid composition of the bilayer is highly regulated, displaying both an asymmetrical distribution of phospholipids between the intracellular and extracellular layers, as well as the presence of specific lipid domains [4]. The lipid bilayer is also a dynamic system, normally defined as two-dimensional fluid, and its asymmetrical composition regulates the transmission of extracellular signals into intracellular ones. For example, the cytosol layer of the membrane is generally enriched with the negatively charged phosphatidylserine, and many cytosolic proteins bind to this side of the bilayer to initiate a cascade of intracellular signals. Aside from the phospholipids, proteins make up for 50% of the weight of a plasma membrane. Proteins, such as receptors, transporters, and enzymes, regulate most of the functions of the cell membrane including

regulation of the intracellular ionic concentration of Na^+ and K^+, transport of polar molecules, and catalysis of membrane-associated reactions such as the synthesis of adenosine triphosphate.

Understanding the structure and functions of the plasma membrane is essential to design efficient intracellular delivery strategies [5]. In this introductory chapter, we will discuss two of the main approaches that have been investigated by researchers to deliver extracellular cargo into the cell and bypass the selective barrier offered by the plasma membrane. These two methods, which have been the main object of investigation in this thesis, include carrier-based and carrier-free strategies (**Figure 1.1**).

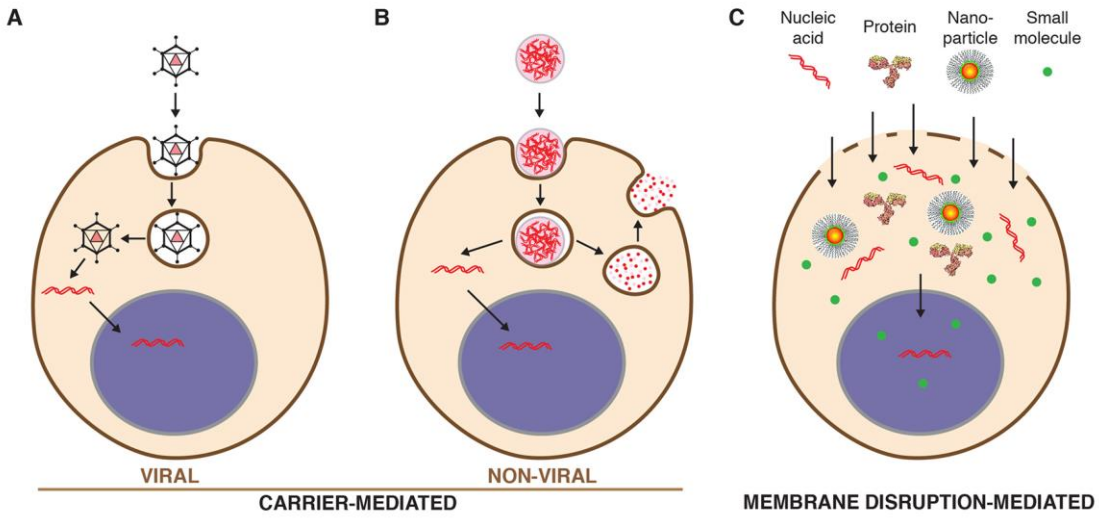

Figure 1.1 Schematic summarizing the main strategies to promote internalization of extracellular cargo. Carrier-based and membrane disruption methods are the two main categories for effective intracellular delivery Reprinted with permission from [142]. Copyright (2018) American Chemical Society.

The former approach involves the use of a carrier that can be internalized by cells through endocytosis pathways. Firstly, we will discuss the different steps a carrier undergoes when internalized into the cytosol with an emphasis on the delivery of genetic material. We will also

provide an overview of the available carrier-based strategies for gene delivery into stem cells, highlighting the key parameters that need to be considered for efficient transfection.

Next, the focus will be shifted towards the second strategy of this thesis by describing the physical and mechanical methods that are commonly used to disrupt the cell membrane and facilitate the delivery of extracellular cargo (proteins, DNA and polymers) without the use of any carrier.

1.1 Intracellular delivery of genetic materials

The modulation of gene expression in stem cells is commonly carried out by introducing exogenous nucleic acids such as DNA (plasmid DNA), RNA, small interfering RNA (siRNA), and microRNA (mRNA) [6]. To be effectively expressed, these genetic macromolecules should reach the nucleus after passing through the plasma membrane [7]. The ideal carrier should deliver an appropriate amount of genetic material into the nucleus of the host cell without causing toxicity. However, the relatively large size and negative charge of the genetic material pose a significant hurdle on the successful internalization and intracellular trafficking to the nuclueus. Their internalization can be achieved using different types of carriers that will be discussed more in detail in section 1.2 of this chapter. However, irrespective of the type of carrier used for the delivery of genes the whole process can be subdivided into five common steps which are: 1) binding of the carrier to the cell membrane; 2) endocytosis, 3) endosomolysis, 4) cytosolic transport toward the nucleus, and 5) nucleus entry. An efficient carrier system for gene delivery must overcome all the obstacles encountered after internalization and guide the translocation of the genetic material to the nucleus to guarantee a successful gene expression.

1.1.1 Cell binding to the cell membrane

Carriers for intracellular gene delivery can be designed to promote selective binding to receptors or establish non-specific interactions with the cell membrane by taking advantage of its superficial properties. For example, the extracellular side of many plasma membranes is glycosylated, meaning that lipids and proteins of the membranes are covalently bound to carbohydrate chains to form glycolipids and glycoproteins, respectively. The role of this carbohydrate layer is to protect the cell against mechanical damage, to avoid cell-cell interactions or to establish direct contact with other proteins of the extracellular matrix. One of the most negatively charged components of the cell surface is represented by sulfated proteoglycans that covalently bind to one or more sulfated glycosaminoglycans present in the extracellular matrix. These highly anionic chains are the target site for carriers with a net positive charge, such as lipoplexes and polyplexes [8].

Cationic carriers transporting DNA or RNA have been extensively used to bind electrostatically to the highly anionic proteoglycans present on the cell surface. In one study, pre-treating of HeLa cells with glycosaminoglycan sulfation inhibitors such as sodium chlorate suppressed the luciferase reporter gene expression up to 70% compared to the untreated cells [9]. In another study, it was shown that Raji cells, which lack proteoglycans, could not be transfected by lipoplexes unless the cells were modified to express the proteoglycan, syndecan-1[10]. The authors also suggested that the transfection efficiency was highly dependent on a net positive charge of the lipoplex. Overall, these evidence suggests that the presence of proteoglycan can mediate the first step of cell binding and that modulation of proteoglycan expression is one of the key targets to enhance the process of gene transfection using cationic carriers.

1.1.2 Activation of specific endocytosis pathways

After the initial binding step on the cell surface, carriers are generally internalized into cells via different endocytosis pathways. The size of the lipoplexes and polyplexes dictates the main pathway of internalization, which can occur through clathrin or caveolae-mediated endocytosis (**Figure 1.2**).

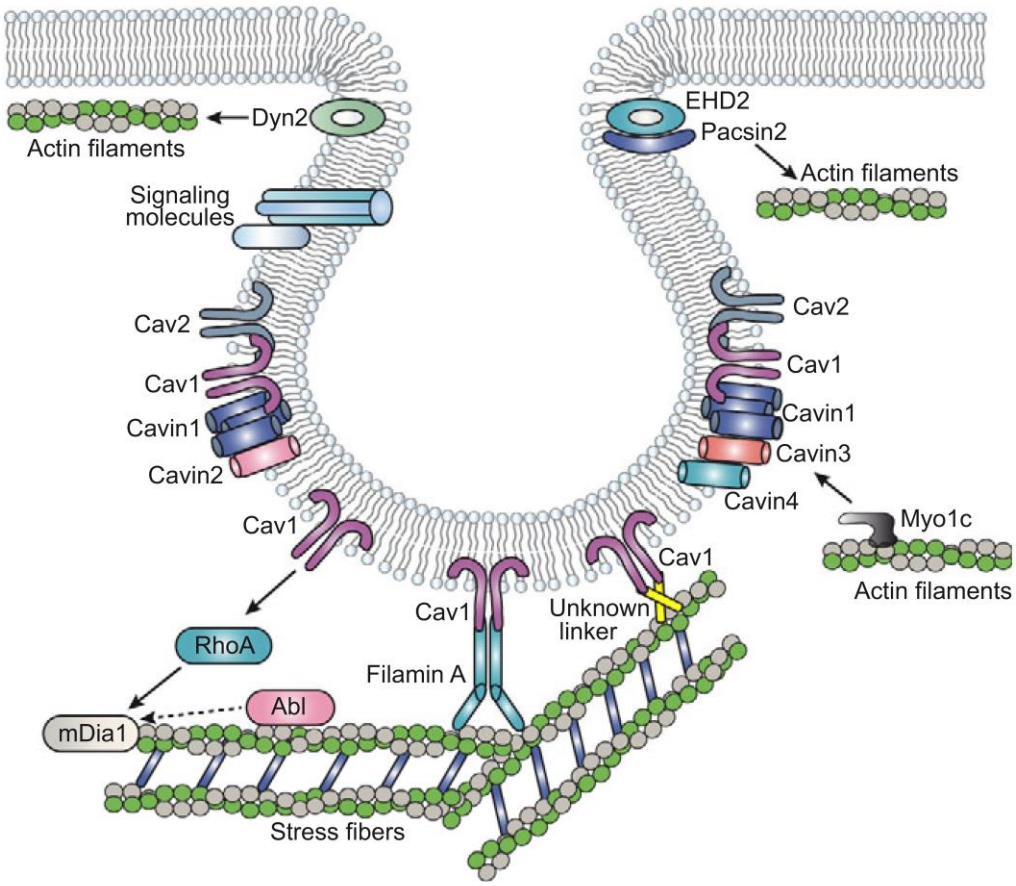

Figure 1.2 Schematic representing the main components of the caveolae machinery necessary to promote endocytosis. Reprinted with permission from [20].

Clathrin-mediated endocytosis is activated in the case of carriers that require specific binding to transmembrane receptors [11]. The binding process triggers the localization of clathrin structures on the intracellular layer of the plasma membrane, which leads to the formation of clathrin-coated

pits. The main components of these pits are heavy and light chains of clathrin proteins which are assembled into three-legged triskelions commonly linked to adapter proteins [12]. Subsequently, the coated pit starts to pinch off from the plasma membrane by the guanidine triphosphates GTPase, dynamin. An ATP-dependent enzyme is then responsible for uncoating the vesicles [13]. It has been shown that nanocarriers with a diameter of less than 200 nm are mainly endocytosed via this pathway in non-phagocytic cells. On the contrary, nanomaterials with a diameter of about 500 nm are commonly internalized by caveolae-mediated endocytosis [14]. Aside from the size, the net charge, and the final configuration of the complex also play essential roles in defining the main selected pathway for the endocytosis of lipoplexes and polyplexes [15]. For instance, Billiet *et al.* showed that positively charged lipoplexes are mainly internalized by clathrin pathway, while negatively charged lipoplexes enter myoblasts via caveolae-mediated endocytosis [16].

This alternative pathway is mediated by the presence of caveolae, which are invaginations in the plasma membrane displaying transmembrane proteins named as caveolins. These flask-shaped invaginations are also rich in cholesterol and sphingolipids and are found on the surface of different type of cells, including muscle cells, endothelial cells, and adipocytes [12, 17]. Caveolae formation is modulated by caveolins with the help of another group of proteins termed as cavins [18]. Caveolae-mediated endocytosis is a microtubule and actin-dependent process. Caveolae are stabilized on the cell surface by cortical actin filaments. Disruption of these filaments by latrunculin A enhances the internalization of caveolar vesicles and their subsequent intracellular transportation [19]. Organization and trafficking of caveolae are influenced by actin stress fibers, which are composed of contractile actomyosin bundles. The linkage between caveolae and actin stress fibers require the presence of Ras homolog gene family member A (RhoA), actin cytoskeleton, and filamin A (an actin-binding protein) [20, 21]. The fate of the pinched off caveola

is cell type-dependent. In non-endothelial cells, the cargo is delivered to endolysosomal compartments whereas in endothelial cells, especially *in vivo*, the cargo may be transferred across the cells to reach the underlying tissue [22].

1.1.3 Fusion with endosomes and endosomal escape mechanisms

Once the cargo is internalized following a preferential route of endocytosis, the vesicles are delivered to endosomes. The cargo is then either sorted back to the cell surface or transported into other compartments such as multivesicular bodies (MVBs) or lysosomes for degradation [18]. An efficient carrier should provide a mechanism to escape from endosomes, circumvent lysosomal degradation, and effectively transfer the DNA into the cytosol.

Different endosomal escape mechanisms can be observed based on the type of carrier internalized in the cytosol. In the case of lipid-based carriers, the process of endosomal escape can occur through two distinct mechanisms: inverted hexagonal configuration and a flip flop model. An example of the first mechanism is commonly observed with the internalization of lipoplexes containing the neutral phospholipid dioleoyl-phosphatidylethanolamine (DOPE). DOPE has been reported to destabilize endosomes, causing the escape of the cargo. Precisely, DOPE can induce a change in the configuration of the lipoplex into an unstable inverted hexagonal configuration, which can rapidly fuse to anionic vesicles and release the DNA into the cytosol [23-25].

The second mechanism of lipoplex fusion and release of DNA is explained by a “flip-flop” model. In this model, the release of DNA is facilitated through four sequential steps: 1) the lipoplex is endocytosed in the endosome membrane, 2) the membrane is destabilized by inducing the anionic lipids, which face the cytoplasm, to orient themselves towards the endosomal lumen known as

"flipping effect"; 3) the anionic lipids form a neutral net charge with the cationic lipids of the lipoplex, and 4) the DNA is displaced and released into the cytoplasm [26].

Finally, in the case of polyplexes, the endosomal mechanism of escape can be explained by a "proton sponge" model. Polyplexes made of cationic polymers such as polyethyleneimine (PEI) can be easily protonated during endosome acidification due to the presence of amine groups. As a result, passive chloride influx causes osmotic swelling and eventually rupture of the endosome with subsequent release of the polyplex [8, 27]. However, the release of polyplexes into the cytoplasm can hinder the efficiency of the transfection, especially if the DNA cannot easily dissociate from the carrier. Several strategies have been proposed to enhance the dissociation of DNA from the polyplex. For instance, reducible Poly(l-lysine) (PLL) can be degraded once in the intracellular environment, and thus induce the release of DNA for subsequent gene expression [28].

1.1.4 Cytosol trafficking and nuclear entry

After dissociating from the polyplexes and lipoplexes, the DNA must travel through the viscous and crowded cytoplasm to reach the nucleus. Small DNAs (less than 2000 bp in size) have been shown to diffuse in the cytoplasm, whereas larger DNA molecules are unable to diffuse and require active methods of transport [29]. The only possible mechanism of DNA translocation to the nucleus is the active transportation mediated by microtubules and molecular motors proteins known as dynein [30, 31]. A recent study supported this hypothesis by demonstrating that a decrease in gene expression is generally observed when the microtubules assembly and dynein activity are inhibited by the co-administration of the drug nocodazole and antibodies against dynein [32]. By contrast, the same study proved that the translocation of DNA into the nucleus is

an independent actin process since no change in gene expression was detected when actin polymerization was inhibited.

Finally, the nuclear entry of plasmid DNA is regulated by a passive transport mechanism occurring during cell division. At this stage, the nuclear membrane is temporarily disassembled, which enables the DNA to enter [33]. Aside from passive transportation, several strategies have been investigated to enhance the nuclear entry of plasmid DNA. One of them consists of utilizing a gene containing a single nuclear localization signal peptide that can facilitate nuclear entry [34]. Similarly, specific DNA sequences can be designed to bind to transcription factors in the cytoplasm to form efficient protein-DNA complexes that can enter the cell nucleus by protein transporters [35].

In the next section of Chapter 1, we will discuss the main viral and non-viral carriers available for efficient delivery of exogenous genes with an emphasis on the advantages and limitations of each strategy. Finally, we will highlight how the cell microenvironment and the intrinsic features of the cell machinery can impact the efficiency of internalization of genetic material.

1.2 Carrier-based strategies for intracellular delivery: Viral vectors

Viral vectors such as adenoviruses, adeno-associated viruses, retroviruses, and lentiviruses can be used as a delivery vehicle for both transient and permanent expression of specific genes in stem cells [36]. These vectors enable the design of specific cell-based therapies to treat a large variety of metabolic disorders, cardiovascular diseases, as well as different types of cancer. They can be subdivided into two main categories based on the type of genetic material they deliver.

1.2.1 DNA-based viruses

Adenoviruses have been under investigation for over 20 years in many clinical trials [37]. This type of viruses possesses double-strand DNA in their genome with a packaging capacity of 7.5 kbp of foreign DNA. Adenoviruses enable transient episomal expression of a target gene in a broad range of host cells. Since the adenovirus DNA does not integrate into the genome of the host cells, this type of viruses is considered to be safe. However, the first generation of these viruses has been shown to cause a robust immune response. Hence, implementing these viruses as viral vectors in gene delivery required the modification of the virus genome. This process can be achieved by the partial or complete deletion of the genetic information to generate the so-called "gutless" vectors with a packaging capacity of 30 kbp [38]. Despite the increased safety of these vectors, their use in gene therapy and regenerative medicine is limited. For instance, one of the main challenges still unresolved is their inactivation by the blood components such as proteins of the coagulation cascade or complement proteins when administered systemically [39].

Another important class of DNA viral vectors is represented by adeno-associated viruses (AAV). AAV are single-stranded DNA viruses that possess an extremely low risk of pathogenicity because of their inability to integrate into the genome of the host cell. These viruses need a helper virus such as adenoviruses for replicating and completing their life cycle [37]. Since AAVs are stable in the blood, there is a limited risk of a severe systemic inflammatory response associated with the administration of these viruses [40]. However, one limitation of AAV is that their transfection efficiency decreases rapidly in dividing cells, and they are more suitable for the transfection of slowly dividing cells such as cardiomyocytes [36].

1.2.2 RNA-based viruses

Viruses carrying RNA are also widely investigated as an important tool for the design of gene therapies to transfect stem cells. One example is represented by retroviruses which are capable of reverse transcription of their RNA into DNA. Thus, retroviruses can integrate their DNA copy into the genome of the host cells. Before the discovery of clustered regularly interspaced palindromic repeats-CRISPR associated protein 9 (CRISPR-Cas9), retroviruses represented the only possible strategy to modify a single gene in patients. This type of viruses can accommodate up to 8 kb of RNA foreign inserts, and they can induce permanent gene expression. Retroviruses have been successfully used to transfect stem cells, or early precursors of blood cells *ex vivo* to treat several conditions, including severe combined immunodeficiency (SCID) [40, 41]. However, the application of these viruses has been associated with a possible risk of oncogenesis [42]. The other drawback of retroviruses is that they are inefficient in infecting nondividing cells [36].

A more appealing alternative is represented by lentiviruses, which is one of the best options for therapeutic applications when a long-term expression is required. Lentiviruses belong to the family of retroviruses that include HIV. These viruses can infect both dividing and non-dividing cells with a lower risk of genotoxicity due to the absence of preferential integration in the host genome close to the onset of transcription units [40, 43]. Lentiviruses have been implemented in several clinical trials for the treatment of a variety of diseases such as X-linked adrenoleukodystrophy and Thalassemia major. Precisely, patients treated with hematopoietic stem cells transfected *ex-vivo* with lentiviruses showed significant improvement and decreased the need for blood transfusion [44]. Although successful in many applications, the possible risks of oncogenesis still remains a big concern for their application in the clinic.

Overall, viral vectors have significantly advanced the field of gene therapy in both clinical and non-clinical applications due to their high efficiency. However, safety concerns and limitations, including carcinogenesis, immunogenicity, difficulty in vector design, and restricted DNA packaging capacity, make them less ideal candidates for gene delivery [45-47]. For these reasons, non-viral vectors are an equally attractive option for gene therapy applications, and great efforts are directed towards the synthesis of more safe gene carriers that rely on organic or inorganic materials.

1.3 Carrier-based methods: non-viral carriers

Non-viral carriers can be fabricated from inorganic, or organic materials, including polymers and lipids. Their size, surface charge distribution, and loading efficiency can be controlled and customized due to the type of material used for their synthesis and process of fabrication. This great versatility in their design combined with their superior biological safety compared to viral vectors are the main reasons these carriers have been the subject of large investigation for gene-based therapies. Non-viral carriers can find applicability for the intracellular delivery of exogenous genetic materials in the form of small DNA, large DNA (plasmid DNA), siRNA, and mRNA. Similar to viral vectors, non-viral carriers have been investigated in many clinical trials to treat a wide variety of diseases, including cystic fibrosis, multiple myeloma, ovarian, and bladder cancer [6]. The following discussion will highlight the available strategies for intracellular gene delivery using carrier-based methods. In particular, different classes of non-viral vectors will be discussed, including inorganic and organic-based nanomaterials as well as lipid and polymer-based carriers for efficient gene delivery.

1.3.1 Inorganic and organic nanomaterials

Inorganic materials such as calcium phosphate, silica, gold, and quantum dots have been widely investigated for the fabrication of nanocarriers with potential applications for gene delivery [48]. The shape, porosity, size and surface charge of the inorganic nanocarriers can be precisely designed to prevent the degradation or denaturation of the entrapped or adsorbed payload (e.g., DNA and mRNA) [49]. Additionally, inorganic nanomaterials offer several advantages such as biocompatibility, low cytotoxicity, and ease of functionalization, which are essential characteristics to formulate efficient gene-based therapies [50, 51].

For instance, the surface of gold nanoparticles can be functionalized with polar functional groups to enable the complexation of DNA. A possible strategy is to modify gold nanoparticles with pH-responsive chemical groups that can allow the intracellular delivery of genetic material. Specifically, a pH-responsive dynamic system based on intercalated motif (i-motif) DNA was conjugated covalently to a surface of gold nanoparticles. The i-motif DNA was linked to a therapeutic siRNA for silencing the *PLK1* gene, which is involved in genome stability and mitosis. Upon intracellular delivery, the gold particles were internalized in endosomes. The lower pH caused a conformational change in the structure of i-motif DNA, which led to the aggregation of the gold nanoparticles. This process facilitated the endosomal escape of the gold nanoparticles determining the release of siRNA into the cytosol [52].

Another interesting option is represented by quantum dots (QDs), which are semiconductor nano-meter sized (2-10 nm in diameter) particles. QDs possess many advantages, such as narrow and symmetric emission, strong absorption, and high photostability. Due to these distinct properties, QDs have been used in bioimaging, biosensing, and particularly in gene delivery applications [53-55]. In one study, multiple QDs coated with poly(ethylenimine) (PEI) were fabricated to facilitate

the binding of green fluorescence protein (GFP) plasmid DNA. These complexes were effectively delivered into human mesenchymal stem cells (hMSCs). The results from this study demonstrated that PEI-coated bundled QDs nanoparticles had higher transfection efficiency when compared to naked QDs [56]. In another study, plasmid DNA was conjugated to QDs for long-term intracellular and intranuclear tracking in Chinese hamster ovary (CHO-K1) cells. Specifically, plasmid DNA was complexed with phospholipid-coated QDs by a peptide nucleic acid–N-succinimidyl-3-(2-pyridylthio) propionate linker. This complex yielded 62% transfection efficiency, which was comparable to the control group (unconjugated plasmid DNA) [57]. Although QDs have shown promising potential in various applications, they can be costly to fabricate and can induce toxicity to cells due to the possible release of heavy metals [58].

Calcium phosphate is another important inorganic compound that can be used to synthesize biocompatible nanoparticles for gene delivery. These nanomaterials, due to the presence of calcium, can easily establish ionic bonds with phosphate groups present in the nucleic acid backbone [59]. The DNA-calcium phosphate complex can be internalized across the cell membrane through ion channel transportation. The procedure to create a nano-complex between DNA and calcium phosphate is straightforward. The process consists of a simple mixture of calcium chloride with DNA, followed by the addition of a phosphate-buffered saline solution [60]. However, this conventional method for the formation of a DNA-calcium phosphate complex has several significant limitations such as low gene expression, insufficient endosomal escape mechanism, limited protection of the DNA from degradation in the cytosol, uncontrolled crystal growth, and finally low nuclear uptake [61, 62]. To overcome these issues, Sololova *et al*., added another layer of calcium phosphate to the DNA-calcium phosphate core complex that protected the DNA from degradation by lysosomes in different cell lines [63]. This additional layer also

prevented crystal growth by the absorption of DNA on the outer layer on the surface of calcium phosphate nanoparticles. Furthermore, other studies have reported how other parameters, such as the concentration of $CaCl_2$ and DNA, temperature, pH value, and the time of complexation can modulate the efficiency of calcium phosphate-based transfection methods [64]. Although calcium phosphate is an effective, simple, and well-known delivery method for *in vitro* transfection, its efficacy is hampered *in vivo* due to their rapid aggregation and risk of precipitation [51].

Aside from inorganic material, carbon-based nanomaterials have been explored for gene delivery. For example, single-walled and multi-walled carbon nanotubes (CNT) have found applications in this field of study owing to their special structural, mechanical, electrical, and chemical characteristics [65-68]. These tubes are chemically inert, and their surface can be easily functionalized with biological molecules such as proteins, peptides, and nucleic acids [69, 70]. Surface functionalization of CNTs as gene delivery vehicles can be achieved by hydrophobic or π-π interaction between the CNTs and the polar ring of the DNA backbone [71]. In one study, ammonium functionalized CNTs were bound to plasmid DNA by electrostatic interactions, and the complex was successfully internalized into HeLa cells [72]. In another investigation, the surface of multi-walled CNTs was modified with PEI through electrostatic interactions. This strategy was used to securely immobilize DNA on to the surface of CNTs by noncovalent bonding [73]. All these non-covalent approaches for binding DNA to CNTs have the advantage of releasing the DNA more favorably compared to strategies that rely on the covalent linkage of DNA. Aside from all the benefits that CNTs provide, there are shortcomings associated with the use of these carries in cells. For instance, CNTs are not degradable inside cells, and hence, they can be cytotoxic to them. However, the level of toxicity depends on the structure of CNTs, and it can be reduced by introducing water-soluble functionalities on the surface of CNTs [68, 74].

1.3.2 Lipid-based carriers

Another important class of carriers for gene delivery that has been used extensively both *in vitro* and *in vivo* is the one derived from lipids. The physical properties of lipid-based carriers such as stability in solution, superficial charge, and loading efficiency strictly depend on the chemistry of the lipid used for their fabrication. A specific class of lipid carriers is represented by liposomes, which are made of phospholipids. These compounds are amphiphilic molecules composed of a cationic, anionic, or neutral head group and a hydrophobic tail that assemble into bilayered spherical structures with sizes ranging from 20 nm to a few microns [33]. Liposomes displaying a cationic superficial charge have been used extensively for intracellular delivery of DNA due to their ability to form a stable electrostatic complex with the phosphate groups of DNA [75-80]. The size of the lipid/DNA (lipoplex) complexes vary from 100 nm to 1 μm, which is based on the type of lipid structure selected to fabricate the liposomes [81]. Liposomes composition can also be modified by the addition of neutral lipids that facilitate the release of DNA from endosomes by hexagonal phase formation mechanism, as discussed in section 1.1.3 [51]. Commonly used neutral lipids are cholesterol, dioleoyl phosphatidylethanolamine (DOPE), and 1,2-dioleoyl-3-trimethylammonium propane (DOTAP) that provide the fabrication of versatile lipid-based gene carriers.

The use of liposomes as gene delivery carriers offers substantial advantages compared to other types of vectors. Firstly, their fabrication is relatively simple, with limited costs of production. Secondly, they do not trigger adverse immune responses and present negligible levels of cytotoxicity. Moreover, they can be used to deliver large pieces of DNA, as large as chromosomes, and they can protect the DNA from nucleases-mediated degradation [82]. Different types of liposome-based gene delivery systems have shown promising results in clinical trials to treat

several diseases such as cystic fibrosis, advanced oral squamous cell carcinoma, solid tumors, and melanoma [83-86]. However, several challenges limit their efficacy *in vivo,* including their limited stability and poor transfection efficiency. These problems arise from the fact that the lipoplexes can be sequestered by circulating proteins in the serum, which greatly reduces their efficacy compared to viral vectors.

1.3.3 Polymer-based carriers

Similar to lipid-based nanomaterials, the physical and chemical properties of polymer-carriers can be finely controlled and modulated based on the type of polymer selected. Polymers can be of synthetic or natural origin; they can display a variety of chemical functionalities in their repetitive units and possess different molecular weights. These set of parameters can be selected to design polymer-carriers that have great potential for gene delivery [87].

Ideally, the polymeric nanocarrier should establish electrostatic interaction with plasmid DNA to form a complex that protects the genetic material from degradation. Additionally, the polymeric carrier should be stable in physiological conditions and should not promote any protein aggregation once administered [75]. A possible solution to this problem is the modification of the surface of the polymeric particles with polyethylene glycol (PEG) to create stable polymeric carriers that do not establish protein interactions and are characterized by limited clearance by the reticuloendothelial system (RES) when used *in vivo* [88-90]. Finally, upon internalization, the delivery of the genetic material to the nucleus strictly depends on the ability of the polymer carrier to avoid degradation of the DNA induced by lysosomes.

Based on these criteria, several polymers have been investigated for the design of efficient nanocarriers for gene delivery. For instance, one of the most used polymers for this purpose is PEI

due to its ability to form polyplexes with DNA by establishing electrostatically interactions between the positively charged primary amine groups and the phosphate groups of DNA [91, 92]. PEI can be synthesized in a linear and a branched configuration, which displays different chemical properties [93]. Branched PEI is more reactive due to the presence of primary amine groups and can form smaller DNA/PEI polyplexes. However, linear PEI is less toxic and has a higher transfection efficiency [94]. Irrespective of its configuration, PEI also possesses a high pH buffering capacity, and it can act as a "proton sponge," which commonly leads to the endosomal escape of PEI-carriers from lysosomes. Specifically, PEI-based nanocarriers once internalized within a lysosome (pH 4.5-5.0) can uptake protons that are pumped into this acidic intracellular compartment. As a result, passive diffusion of chloride ions occurs within the vesicle leading to water influx. Finally, due to the increased osmotic swelling, the endosome ruptures and the PEI-DNA complex is released into the cytoplasm [95]. This proton sponge hypothesis enables PEI-based nanocarriers to escape from lysosomes avoiding the degradation caused by them. Similarly, the same pH buffer capacity of PEI is responsible for the inhibition of lysosomal nucleases, which are the main enzymes responsible for the cleavage of phosphodiester bonds of DNA [95]. Despite all these advantages, one of the challenges associated with the use of PEI-based carriers is their low transfection efficiency and cytotoxicity induced by the presence of numerous positive charges [96]. A possible strategy adopted to reduce the cytotoxicity of PEI is to coat the PEI/DNA polyplex with disulfide-modified hyaluronic acid (HA-SS-COOH). This modification has been shown to promote higher cell viability combined with a 14-fold increase in transfection efficiency compared to PEI/DNA without any modification [97].

Another example of cationic polymer widely used in gene delivery application is poly-L-lysine (PLL) that has the advantage of being biodegradable when used for *in vivo* applications. PLL has

been tested for pancreatic cancer treatment and hormone stimulation in melanoma cells [98, 99]. Similar to PEI, PLL can form electrostatic complexes with plasmid DNA or RNA efficiently. However, PLL has a relatively lower transfection efficiency compared to PEI [100]. One solution to this problem is the design of particles consisting of PLL conjugated with targeting moieties of endosomolytic agents such as fusogenic peptides that can promote endosomal escape and prevent DNA degradation [101]. Additionally, to overcome lysosomal degradation, PLL has been modified with histidine residues, and the transfection efficiency of histidylated PLL was 3-4.5 orders of magnitude when compared to PLL alone [102].

1.4 Strategies to enhance gene delivery by modifying the cell microenvironment

As described earlier, the intracellular delivery of genetic material can be controlled by the proper selection of a specific carrier. However, the biological and physical cues that define the cellular microenvironment have a similar impact on the delivery efficiency and corresponding transfection. Precisely, cells actively interact with the extracellular environment by sensing physical, biological, and mechanical stimuli. Cells respond to these cues by converting them into intracellular signaling cascade that commonly leads to significant changes in cell morphology, proliferation, and expression of key proteins [103, 104]. Understanding the role of these cues can be useful to augment the efficacy of gene-based strategies. In this section, we will examine the possible chemical and physical approaches that have been explored so far to modify the cell-substrate and modulate intracellular uptake of gene carriers discussed in the previous sections.

1.4.1 Chemical modification of the substrate to enhance gene delivery to adhering cells

The cell microenvironment directly controls various cellular responses such as morphology, adhesion, and proliferation. Precisely, cells adhere to a substrate by establishing focal adhesions through the presence of specific transmembrane receptors called integrins that recognize specific domains of the proteins of the extracellular matrix (ECM). The extent of these anchorage points and the corresponding rearrangement in the cellular cytoskeleton can directly impact gene delivery and transfection efficiency [105].

One of the avenues explored to enhance the internalization of genetic cargo is by controlling the formation of anchorage points on a cell-substrate. For instance, several proteins present in the ECM, including fibronectin, laminin, collagen I/IV, and vitronectin, can be adsorbed as coatings on the surface of synthetic substrates to enhance gene transfection [105]. Dhaliwal *et al*. examined and compared the effect of collagen I and fibronectin coatings on the transfection efficiency of bone marrow-derived mesenchymal stem cells (MSCs) using PEI as a non-viral vector. Cells cultured on fibronectin-coated substrates exhibited higher transfection, although higher internalization of PEI/DNA polyplexes was observed for the collagen I group [106].

Based on these results, the same authors investigated in another study the role of Rho-GTPases activity in mouse mesenchymal stem cells seeded on the same types of substrates. Rho-GTPase proteins are involved in the modulation of cytoskeletal dynamics, including cellular contractility and stress fiber formation. Stem cells cultured on fibronectin-coated substrates expressed higher amount of Rac1, cdc42, and RhoA compared to the cells cultured on collagen I. Additionally, after inhibition of these regulators a decrease in transfection efficiency was observed suggesting that actin stress fiber formation is the main responsible for intracellular trafficking. Overall, these results indicated that transfection of stem cells seeded on fibronectin-coated substrates is directly

controlled by integrin binding, cytoskeletal dynamics (stress fibers), and RhoGTPases activity [107].

Polysaccharides found in the ECM can also be used to modulate the cytoskeletal rearrangement and influence intracellular gene delivery. For example, hyaluronic acid (HA) is a high molecular weight polysaccharide found in soft connective tissues that can be conjugated with other polymers. These conjugates can be implemented as interactive coatings that can affect the cellular morphology and modulate the delivery of genes. In one study, murine adipose-derived adult stem cells were cultured on glass slides coated with chitosan and chitosan modified with HA. Cells were subsequently transfected with naked DNA, and the level of transfection efficiency was compared to cells seeded on tissue culture plates without any coating. Cells seeded on chitosan and chitosan-HA coated surfaces formed spheroids and displayed a higher transfection efficiency. The change in cytoskeletal rearrangement was associated with an upregulation of RhoA gene, which controls the assembly of focal adhesions and actin stress fibers [108]. Upregulation of RhoA could be the reason for the increased endocytosis, and higher internalization of the plasmid DNA observed in the cells cultured on chitosan and chitosan-HA groups [109].

Aside from natural polymers, synthetic coatings can be used to bind proteins and regulate change in cell morphology for efficient intracellular delivery. Specifically, polymeric self-assembled monolayers (SAMs) can be homogenously manufactured and subsequently added to the substrate to allow protein and cell adhesion [110]. For example, gold substrates have been coated with different SAMs displaying methyl or carboxyl groups. NIH-3T3 fibroblasts were seeded on these coated substrates, and the cells were transfected with GFP plasmid using Lipofectamine2000 and branched PEI. Irrespective of the carrier used, higher transfection efficiency was observed for the fibroblasts seeded on the substrate coated with SAMs modified with carboxylic groups [111].

Another interesting alternative to enhance gene delivery is known as substrate-mediated gene delivery. This strategy consists of immobilizing naked or complexed nucleic acids on a substrate so that the cargo is available for cellular uptake after seeding [112]. This process is also known as "reverse transfection", which is accomplished by electrostatically or covalently immobilizing DNA onto substrates [113-115]. In one study, tissue culture well plates were coated with different serum and ECM proteins, including bovine serum albumin (BSA), fetal bovine serum (FBS), fibronectin, collagen I, and laminin. Subsequently, branched PEI/DNA complexes were electrostatically adsorbed on the protein-coated substrate to facilitate gene uptake by NIH-3T3 cells [116]. The lipoplexes uptake was significantly higher on the substrate coated with fibronectin and collagen I. However, the transfection efficiency was significantly enhanced in the fibronectin group compared to all the other protein coatings. It was concluded that the augmented cellular focal adhesion expression and cytoskeletal rearrangement induced by the presence of fibronectin was the main reason for the increased endocytosis and intracellular trafficking of the immobilized lipoplexes.

1.4.2 Physical modification of the cell-substrate to enhance gene delivery to adhering cells

Aside from the chemical modification of the cell-substrate, cellular responses can be controlled by altering the physical properties of the microenvironment [117, 118]. Several studies have shown that a change in topography or stiffness of the substrate can directly affect cell adhesion, proliferation, focal adhesion expression, and cytoskeletal dynamics, which in turn can enhance transfection efficiency using different non-viral carriers [119-121].

The topography of a cell-substrate can be designed to mimic the physical cues found in the ECM. Different structures, including grooves, pores, fibers, and pillars, can be fabricated using

lithography, nanoimprinting, and acid etching using a variety of synthetic substrates [122, 123]. For instance, the topographical properties of silicon substrates can be modified by introducing micropillars, nanopillars, or grates made of poly(methylmethacrylate) (PMMA). In a study by Teo *et al.*, silicon-PMMA substrates displaying micro and nanopillars have been tested on different cell lines, including mesenchymal stem cells, breast cancer cells, and simian fibroblasts. The change in morphology observed in all the different cell lines seeded on the substrates modified with micro and nanopillars was associated with a higher transfection of GFP-encoding DNA/Lipofectamine2000 complex when compared to the cells seeded on the flat substrates used as a control. It is likely that the changes in cytoskeletal rearrangement induced by the different topographies indirectly enhanced the process of endocytosis in the tested cells [124].

Based on a similar concept, another research group investigated the transfectability of naked plasmid DNA in hMSCs seeded on negatively charged polyurethane (PU) substrates containing microgrooves [125]. The transfection efficiency of hMSCs seeded on the modified substrates by using naked GFP plasmid DNA was similar to the cells transfected with standard transfection reagents. hMSCs seeded on the PU substrates containing the microgrooves also displayed an increase in the expression of integrins β1 and α5, as well as focal adhesion kinases (FAK). Overall, all of these factors may have contributed to the observed enhancement of endocytosis and intracellular trafficking of plasmid/DNA complexes.

Apart from substrate topography, another physical parameter widely investigated to modulate gene delivery is the stiffness of the cell-substrate. Different biomaterials can be engineered to create biomimetic substrates with values of stiffness ranging from 10^3 Pa to 10^9 Pa, which are characteristic of soft and hard tissues, respectively [113]. The elastic modulus of the cell-substrate is one of the main modulators of cell spreading, cell signaling, and stem cell differentiation [126-

128]. Additionally, cell membrane tension, actin fiber formation, and cell area can be significantly modified by the stiffness of the substrate. Interestingly, these changes have been shown to modulate the internalization of bio-conjugated nanoparticles and non-viral vectors, as well as transgene expression [129, 130]. In a study conducted by Jong *et al.*, the effect of substrate stiffness on transfection efficiency of murine MC3T3-E1 pre-osteoblasts using PEI-DNA was investigated. In this work, the stiffness of alginate-based hydrogels was varied from 20 kPa to 110 kPa and used as a model to study transfection efficiency. Cells seeded on the stiffer substrates showed higher proliferation, cell survival, and transfection [131]. A similar increasing trend for internalization and transfection of linear PEI-DNA was observed when NIH-3T3 fibroblast, myoblast, and bone marrow stromal cells were seeded on fibronectin-conjugated poly(ethylene glycol) diacrylate hydrogels with varying stiffness from 10 to 670 kPa. Additionally, the stiffness of these hydrogels affected the cell's projected area as well as the nuclear aspect ratio. These results suggest that actin stress fibers and microtubules rearrangement are responsible for the observed changes in cellular morphology and nuclear shape. These cytoskeletal components directly influenced the intracellular trafficking of polyplexes and as a result, the transfection efficiency [132].

1.5 Intracellular delivery by membrane disruption methods

Internalization of extracellular cargo has been investigated through alternative approaches that do not require the use of any carrier. These methods aim to increase the permeability of the cell membrane by creating transient pores, lesions, or defects of different shapes and sizes. Although these methods overcome the possible cytotoxic effects and safety concerns associated with the use of any nanomaterial or viral vector, several parameters need to be considered to guarantee efficient delivery without affecting the cell viability. One of the big challenges is that the method used to

create the pores should not be toxic and should not induce irreversible damage to the cell membrane. Similarly, several of the approaches are not efficient enough because of the limited number of cells that can be processed (low throughput), thus limiting their applicability in pre-clinical and clinical applications.

Overall, these methods can be subdivided into two major classes: direct penetration and permeabilization-based approaches (**Figure 1.3**).

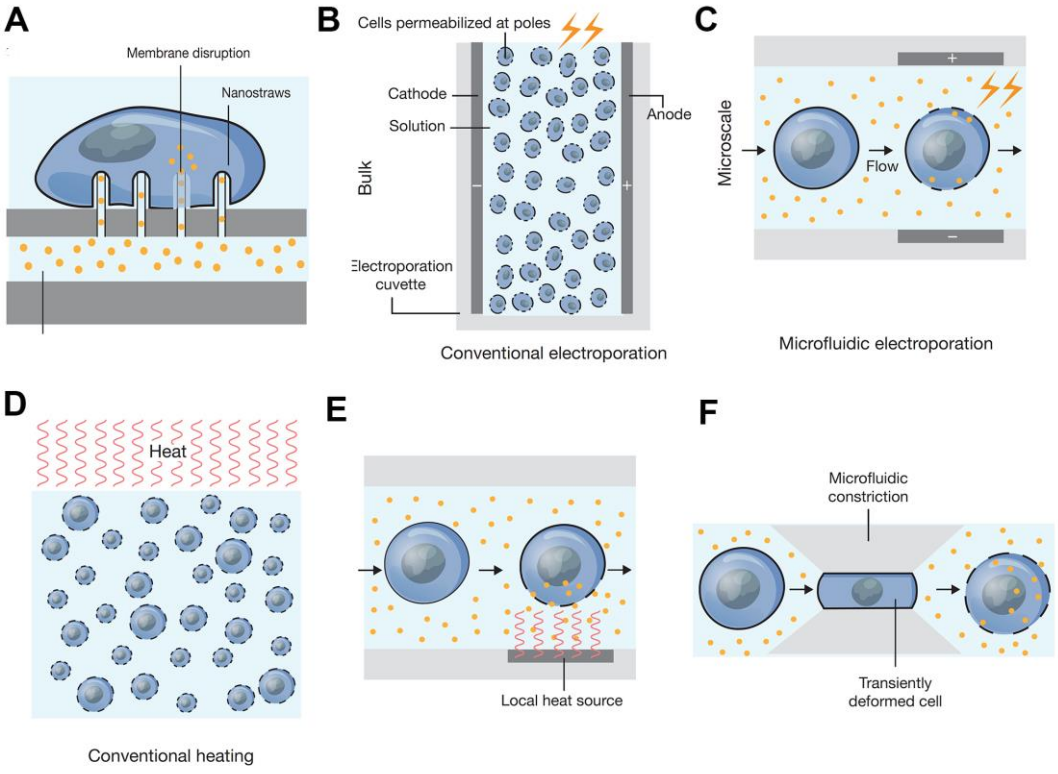

Figure 1.3 Strategies for the permeabilization of the cell membrane using physical and mechanical approaches. A) Nanostraws induce membrane disruption for the delivery of extracellular cargo. B) and C) Electroporation strategies for the delivery of external cargo. D) Conventional heating induces changes in the permeability of the cell membrane. E) Heat can be directed in localized regions of the cell membrane to reduce the risk of toxic effects. F) Cell squeezing through micro-constrictions induces the formation of transient pores in the cell membrane. Reprinted with permission from [176].

The first class consists of a group of strategies aimed to deliver cargo directly into the intracellular space by utilizing a vehicle or a conduit that pass through the cell membrane. In this category, it is possible to include microinjection, ballistic particles, and nanoneedles-based delivery. The

second category, such as permeabilization-based strategies, enables the delivery of extracellular cargo primarily by generating pores in the cell membrane. These pores can be created by different physical and mechanical methods that will be described more in detail in the following sections

1.5.1 Penetration methods: microinjection, nanoneedles, and biolistic-based delivery

Microinjection is the first method of intracellular delivery that was the first to be used in 1911 and perhaps the most direct method for delivering exogenous materials regardless of the cell type [133]. The materials are directly injected into the cells by using fine glass needles [134]. Different types of molecules, including DNA, RNA interference, proteins, peptides, and non-diffusible drugs, can be delivered into cells with nearly 100% efficiency [135-139]. Furthermore, precise control over the volume of the cargo delivered into the cytoplasm or the nucleus can be achieved by microinjection. Despite its accuracy and versatility, microinjection suffers from being a low throughput and time-consuming method of delivery [140, 141]. Additionally, utilizing microinjection in small cells such as blood cells (< 10 μm in diameter) can be challenging. It should also be noted that using microinjection in non-adherent cells can add more complexity to the overall process as there is the need for extra equipment to keep the cells in place prior to being microinjected [142].

Similar to microinjection, nanoneedles are nano-scaled features that can penetrate into cells and deliver exogenous cargos directly in the cytosol. The cargo can be delivered by using nanoneedles in three different ways. In the first method, the target material is attached on the nanoneedles and subsequently dissociated form them upon entering the cytosol. Different types of molecules, including siRNA, DNA, proteins, and peptides, have been successfully delivered in several cell lines such as neurons and immune cells [143-145]. Another possibility consists of directly

pumping the cargo into the cytoplasm via hollow nanoneedles or “nanostraw”. The advantage of using this method is the temporal control over the concentration and volume delivered [146]. Finally, in the third strategy, a grid of diamond nanoneedles is placed on top of adherent cells and subsequently spun down to create small holes in the plasma membrane, thus allowing the diffusion of the delivered materials. This approach has been successfully used to deliver different types of molecules into primary neurons while maintaining high cell viability [147]. Overall, nanoneedle injection is a straightforward and efficient approach, although its applicability is limited by the difficulty associated with the fabrication of the nanostructures and their utilization at large scales. Biolistics-based intracellular delivery, also known as “gene gun”, utilizes high-velocity microprojectiles to deliver DNA and other types of molecules into different cell types. The microprojectiles need to reach an optimum velocity to be effective. This requirement can be provided by a gas shock wave in the form of a high-voltage electronic discharge, chemical explosion, or helium shock [148, 149]. The particles (tungsten, gold, or silver) will then strike the cell membrane, entering the cytosol, and release the cargo molecule from the surface into the cytoplasm. The size of the particles conjugated with the delivery material should not exceed one-tenth of the size of the target cells. DNA, mRNA, siRNA, and proteins have been successfully delivered using this method in mammalian cells [150-152]. One of the limitations of this method is the inherent inconsistency of delivery. Specifically, the particles are bombarded on to the cultured cells from a distance that can vary from one experiment to another. Also, another major disadvantage of this method is the cytotoxicity that the particle can cause when impacting the cell membrane at high velocity.

1.5.2 Permeabilization methods by using energy sources

Permeabilization methods can generate transient pores in the cell membrane by using different types of energy source, including electrical, thermal, and ultrasounds. For instance, electroporation is a very useful method that relies on the use of rapid high-voltage electric pulses to generate an electric field higher than the capacitance of the cell membrane leading to the formation of reversible pores [139]. As a result, extracellular molecules enter the cytosol by passive diffusion or electrophoretic force. Electroporation has been around since the1980s and has been successful in the intracellular delivery of plasmid DNAs, mRNA, proteins, quantum dots, antibodies, and many other cargos [153-157]. However, the strong, intense electrical fields required to deliver large bioactive molecules such as proteins and DNA can cause significant damage or cell death [158, 159]. Different strategies have been recently implemented to reduce the adverse effect of high voltage in conventional electroporation. Specifically, microfluidic devices have been designed to provide a localized electrical filed to a single cell, thus reducing the required voltage by 100-fold. Another advantage of coupling electroporation with microfluidic chips is the possibility to design systems that can expose cells to high voltages while keeping them at a larger distance from the electrodes [160].

Aside from electrical pulses, membrane disruption and small holes can be created in the cell membrane by different types of thermal treatment. For instance, it is possible to cause lipid dissociation in the plasma membrane when the cells are exposed at supraphysiological temperatures higher than 42° C. This effect is mainly due to the high kinetic energy, which causes intense molecular fluctuations. Specifically, it has been proved that small molecules (< 1 kDa) can be internalized into 3T3 fibroblasts at temperatures above 55° C [161].

On the contrary, at temperatures below 0° C ice crystals start to form. Upon thawing, the ice crystals can cause cytosolic expansion, which triggers the formation of holes in the membrane. Finally, rapid heating between physiological temperatures (0° C- 42° C) can generate small transient holes in the membrane [162]. However, these bulk thermal induction methods can be harmful and hinder cell functionality. One way to avoid these detrimental effects is to confine the heat energy to a localized area by using thermal inkjet printers. Successful gene transfection in Chinese hamster ovary (CHO) cells was observed by using this technology [163]. Another strategy to circumvent the detrimental effect of bulk thermal induction to cells is to use absorbent nanoparticles, which can serve as nucleation sites for intense localized heating upon laser irradiation [164].

An alternative type of energy that can be used to create temporary holes in the cell membrane is the one provided by ultrasounds. This method is generally known as sonoporation. Cells are bound to vibrate at a constant frequency by continuous ultrasound waves creating gas bubbles form in the liquid, which boosts the permeability of the cell membrane [165]. The limitation associated with this method is the need for powerful ultrasound pulses to promote high internalization efficiency. This exposure to ultrasounds waves can cause extensive plasma membrane damage and cell death. The observed poor cell viability is due to harsh heterogenous cavitation that causes damage to some cells while others remain intact [166]. To avoid cell death, targeted cavitation is more favorable. In this technique, cavitation bubbles are precisely positioned at a certain distance from the cell, which can induce a shear force required for the plasma membrane rupture [167, 168]. A more sophisticated and extremely high throughput (100,000 cells per minute) design has been developed to create membrane pores. In this platform, the cells are allowed to adhere to a porous substrate lined with titanium absorbers. Rapid pulse laser scanning creates cavitation bubbles

underneath the cells at the titanium linings inducing plasma membrane pores. As a result, large cargoes such as bacteria (>1 µm) can enter the cytoplasm of different types of cells [169].

1.5.3 Permeabilization by mechanical forces: "cell squeezing"

Cell squeezing strategy has been recently proposed to generate small transient holes in the plasma membrane (**Figure 1.4**).

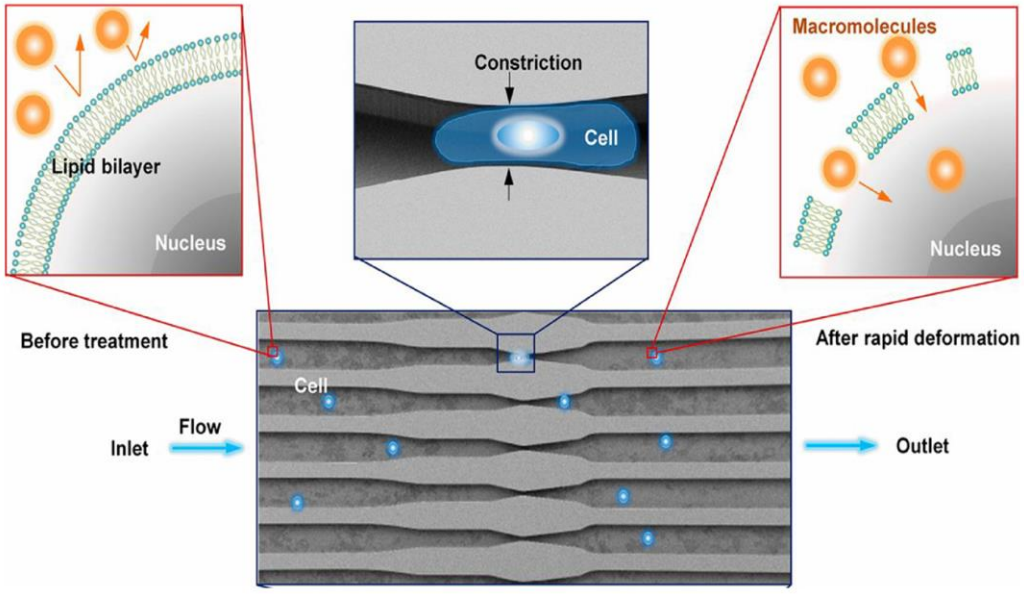

Figure 1.4 Example of the cell squeezing method to create transient pores for the delivery of extracellular cargo. Reprinted with permission of [177]. Copyright (2013) National Academy of Sciences

Precisely, induction of pores is accomplished by squeezing the cells through micron-sized microfluidic constrictions of around half to one-third of the cell's diameter [170-172]. This mechanical deformation of the plasma membrane allows the internalization of extracellular materials into the cytoplasm by passive diffusion without the need for a toxic carrier [173]. Microfluidic chips can be designed with different features and sizes to control cell squeezing. Precisely, the type of geometry has been shown to affect the internalization efficiency and cell

viability of extracellular cargo via the shear stress experienced by the cells [174]. Furthermore, this method does not induce toxicity or cell death as the plasma membrane recovers after it ruptures through squeezing [175]. Additionally, this technique offers the advantage of being rapid and high throughput without the requirement of a costly apparatus or external source of energy. The driving force needed for the cell's membrane disruption can be supplied by the flow of the cell suspension passing forcibly through the microfluidic device [176]. Internalization of numerous types of cargos in many cell types has been reported by cell squeezing. For instance, several studies have demonstrated the possibility to successfully delivery many types of cargos such as gold nanoparticles, quantum dots, carbon nanotubes, and antibodies into HeLa cells [177]. More importantly, the cell squeezing platform can be implemented to achieve high efficiency in gene delivery and gene editing applications, especially in hard-to-transfect cells. Han *et al.* showed successful applicability of cell squeezing for CRISPR (clustered regularly interspaced short palindromic repeats)–Cas9 (CRISPR-associated) genome editing, by implementing a series of microfluidic devices with different geometries [178]. Single guided RNA and Cas9 protein were delivered in HeLa and human luminal-like MCF7 cells for inducing the mutation of specific genes and knocking down their functionality. Additionally, GFP plasmid was delivered with high efficiency in basal-like SUM 159 breast cancer cells, human SU-DHL-1 anaplastic large cell lymphoma cells, and mouse AB2.2 embryonic stem cells, which are known to be hard-to-transfect cells. In another study conducted by Ding *et al.*, the microfluidic cell squeezing platform was combined with microelectrodes [179]. This unique device enhances the efficiency of delivery through two steps without compromising cell viability. In the first step, the cells are squeezed, and as a result, the membrane pores are generated, allowing the internalization of cargo molecules. In the second phase, the cells are passed through an electric field, which leads to disruption of the

nuclear envelope. Subsequently, plasmid DNA molecules can be rapidly translocated to the nucleus and hence increase the transfection efficiency. It has been shown that 80% expression of GFP plasmid took place within the first four hours of transfection, similar to microinjection. Overall, delivering different kinds of cargos by cell squeezing platform is rapid (millions of cells per seconds), safe (high cell viability), efficient, versatile, and applicable to numerous cell types. However, it should be noted that the correlation between cell size and delivery efficiency should be carefully considered when designing cell squeezing devices. For instance, if the squeezing gap is not optimized based on the diameter of the cells, large cells such as multinucleated cells may be lysed while smaller cells may not sufficiently deformed [176].

1.6 Aim of the thesis

The work that will be described in the next chapters of this thesis can be subdivided into two separate aims based on the strategy adopted for the intracellular delivery of the extracellular cargo. The first aim was to investigate the modulatory role of substrate stiffness in the transfection of stem cells by using conventional lipid-based carriers transporting plasmid DNA (lipoplexes).

Chapter 2. discusses the strategy proposed to achieve this goal. Specifically, human adipose-derived stem cells were used as a model cell line for this study and seeded on silicon-based hydrogels displaying different values of stiffness ranging from soft 0.5 kPa to stiff 32 kPa. The chapter describes how this change in this physical parameter could influence cell morphology, cytoskeletal rearrangement, and focal adhesion expression. Subsequently, the study focused on verifying whether these changes had any significant impact on the process of transfection by using Lipofectamine2000 complexed with plasmid DNA encoded for vascular endothelial growth factor. The chapter also discusses the type of endocytosis pathways activated during the internalization

of the lipoplexes and how a change in substrate stiffness can control the upregulation of clathrin and caveolin genes. The findings of this chapter are essential to advance the understanding of how the physical properties of the cell microenvironment can be modified to enhance the efficacy of lipid-based strategies for gene delivery.

Subsequently, the second part of the thesis was focused on the investigation of a free-carrier based approach. Specifically, the goal was to enable the delivery of small polar molecule that cannot pass through the membrane such as trehalose to promote efficient cryopreservation of stem cells without the use of dimethylsulfoxide (DMSO). Trehalose is a cryoprotecting agent (CPA) that could be used as a replacement of the more toxic molecule DMSO. However, the poor permeability of trehalose through cell membranes limits its applicability as a CPA for stem cell banking application.

Chapter 3 addresses the first part of this aim by describing the process of fabrication of a microfluidic chip used to squeeze the cells and create transient small pores in the cellular membrane to enable the delivery of extracellular cargo without the use of any carrier. The design of the micro-constrictions has been varied to promote maximum delivery efficiency of fluorescent extracellular cargo. Additionally, several parameters, including flow rate, the gap between the micro-constrictions, and molecular weight of the cargo delivered, have been optimized and tested by evaluating cell viability. The safety and efficacy of the microfluidic device have been assessed by studying apoptosis and evaluation of stemness gene expression. The chapter also describes the mechanism involved during the process of membrane sealing after the disruption of the membrane induced by the microfluidic device.

Chapter 4 presents the use of the optimized microfluidic system for the intracellular delivery of trehalose. The optimal concentration of trehalose both at the intracellular and extracellular levels

were optimized based on the cell viability assessed after cryopreservation. Additionally, several other biological parameters, including proliferation rate, cell morphology, apoptosis, and differentiation potential of hASCs loaded with trehalose, were compared to cells cryopreserved using DMSO. Overall, the strategy investigated in this study is an example of a carrier-free strategy that can be implemented to provide the delivery of trehalose and promote a safer alternative for cryopreservation with respect to DMSO.

Finally, **Chapter 5** contains the concluding statements of this thesis and a summary of the key findings for each aim. Moreover, a discussion will be provided on how the results of this thesis can be used to support future developments in the field of gene therapy and stem cell banking taking into account both carrier-based and carrier-free strategies for intracellular delivery.

CHAPTER 2. Deciphering the role of substrate stiffness on stem cell transfection using lipid-based nanocarriers to deliver angiogenic genes

Abstract

Substrate stiffness is an important parameter regulating stem cell morphology and cytoskeletal organization. It may also play a critical role in the internalization of lipid-based nanocarriers for gene delivery. Based on this hypothesis, the present study investigates the role of substrate stiffness on non-viral transfection of human adipose-derived stem cells (hASCs) with the aim to maximize hASCs expression of vascular endothelial growth factor (VEGF) and enhance their wound healing potential. hASCs display more actin stress fibers when cultured on stiffer silicone substrates that mimicked the elasticity of hard tissues such as bone. This change in cytoskeletal composition facilitates a greater internalization of plasmid/Lipofectamine lipoplexes. Additionally, the investigation of the main pathways involved in endocytosis is reported by studying the gene expression post-transfection. Caveolin-mediated genes are upregulated in the hASCs cultured on the stiffer silicone substrates, thus confirming the role of actin as a key mediator in the internalization of lipoplexes. Transfected hASCs seeded on more rigid substrates exhibit higher levels of VEGF expression when compared to hASCs cultured on softer hydrogels. Overall, these findings suggest that a higher plasmid internalization and corresponding VEGF expression can be obtained when hASCs are cultured on hydrogels resembling the elasticity of hard tissues.

Modaresi S., Pacelli S., Whitlow.J, Paul A. Deciphering the role of substrate stiffness on stem cell transfection using lipid-based nanocarriers to deliver angiogenic genes, Nanoscale 10(19)2018, 8947-8952.

2.1 Introduction

Gene delivery to stem cells is carried out using both viral and non-viral nanocarriers, which are designed to improve the internalization of plasmid DNA vectors encoding therapeutic genes [180, 181]. Viral carriers, such as adenoviruses, lentivirus, and retrovirus yield a high transfection efficiency because the transduction of viral DNA is facilitated by the viral envelopes surrounding their capsids. However, several safety concerns limit their applicability in gene therapy, including biosafety, immunogenicity, and possibility of mutagenesis [182]. On the contrary, non-viral gene nanocarriers such as cationic polymers, lipids, and peptide conjugates provide a safer alternative to viral carriers given their low toxicity, lack of pathogenicity, versatile surface chemistry, and controllable size [8, 183]. These set of unique advantages makes this type of nanocarriers a suitable candidate to ensure enhanced DNA delivery with limited cytotoxic effects. The selected carrier can also have a positive impact on transfection efficiency by promoting transmembrane diffusion of the genetic material, circumventing lysosomal degradation of the complex, and enhancing intracellular translocation to the nucleus [106]. For all these reasons, the selection of an appropriate nanocarrier directly influences the final outcome of gene-based therapies aimed to regulate transient growth factor expression in stem cells.

Aside from these carrier properties, internalization of plasmid-DNA lipoplexes is also dependent on the elasticity of the cellular microenvironment, which controls the cell membrane tension and the cytoskeletal remodeling [184]. Plasmid-DNA lipoplexes are internalized through several pathways including macropinocytosis, caveolin-mediated endocytosis [185], and clathrin-mediated endocytosis [13, 186], which in turn are regulated by the polymerization of actin stress fibers in the cytoskeleton [187]. Therefore, understanding the influence of substrate stiffness in modifying the intracellular organization of actin stress fibers is beneficial in optimizing

transfection efficiency in non-viral gene delivery. For instance, culturing pre-osteoblasts on stiff substrates, which mimic the elasticity of hard tissues, has been found to enhance non-viral transfection efficiency [188].

Based on this concept, we evaluated the role of substrate stiffness as a parameter in gene transfection of hASCs with the goal of maximizing the transient expression of VEFG-A. hASCs were chosen as a model stem cell line due to their high proliferative potential, ease of harvest, and inherent ability to produce angiogenic growth factors. hASCs were purchased from RoosterBio and harvested from human lipoaspirate of female donors (31-45 years old). Our hypothesis is that transfection efficiency and corresponding growth factor production of hASCs can be enhanced by varying the physical properties of the cell-substrate. Overall, our findings can be beneficial for the design of scaffolds with suitable stiffness for optimal transfection efficiency. Finally, this study will provide useful insights regarding the role of actin fiber stress as one of the main regulators of plasmid DNA internalization.

2.2 Materials and Method

2.2.1 Silicon gel substrates coating

CytoSoft® 6-well plates presenting different stiffness (0.5 and 32 kPa) were purchased from Advanced BioMatrix (Carlsbad, CA, USA). The well plates were made of silicon-based gels displaying on the surface anhydride functional groups that can be used to covalently bind ECM proteins necessary for promoting cellular adhesion. The surface of the gels was pre-coated with a sterile solution of Gelatin type A (1% w/v) from porcine skin (Sigma-Aldrich, USA) in PBS at pH 7.4. The coating step was carried out by adding 4 mL of gelatin solution in each well for 4 hours

at room temperature to ensure the homogeneous coating of the hydrophobic surfaces. The same procedure was applied to coat the CytoSoft® Imaging wells 24-well plates (Advanced BioMatrix, San Diego, CA) having different stiffness (0.5 and 32 kPa). This type of well plate was used for imaging cells at higher magnification (40X).

2.2.2 hASCs culture and fluorescence immunostaining

hASCs were purchased from RoosterBio (RoosterBio, USA). Passages 4–6 were used for all the studies. Cells were cultured in Minimum Essential Medium Alpha Modification (α-MEM) (Thermo-Fisher Scientific, USA) supplemented with 15% fetal bovine serum (FBS) (Thermo-Fisher Scientific, USA) and 1% penicillin/streptomycin (Thermo-Fisher Scientific, USA) at 37 °C and 5% CO_2. Cells were seeded (2×10^4 cells/well) on CytoSoft® Imaging wells with different stiffness (0.5 and 32 kPa) to study the influence of substrate stiffness on the focal adhesion expression of hASCs. After 24 hours, the media was replaced with α-MEM without FBS, and cells were cultured in these conditions for 48 hours. Cells were then fixed with 4% paraformaldehyde for 5 minutes at 37 ºC followed by permeabilization with 0.1 % Triton-X100 for 10 minutes at room temperature. Normal goat serum (5%) was applied for 45 minutes at room temperature to block the samples. Mouse anti-human Paxillin antibody (1:400 with 1% goat serum, Invitrogen, USA) was added to cells and incubated overnight at 4 °C. Next, goat anti-mouse AlexaFluor 594 (Invitrogen USA) (1:500 in 1% goat serum) was added to the cells for one hour at room temperature. Nuclei and F-actin were counterstained using Diamidino-2-phenylindole dilactate (DAPI, Invitrogen, USA) and phalloidin-AlexaFluor 488 (Invitrogen, USA), respectively. Immunofluorescence images were taken by EVOS cell imaging system (Thermo-Fisher Scientific, USA) and further analyzed in ImageJ for quantification of area occupied by each cell, number of

actin fibers, and the total area of adhesion sites. Specifically, the cell area was quantified using 7 to 10 cells per image for a total of 10 images per group (n=10). The number of actin stress fibers was counted based on a total of 7 images, each containing one cell captured at 40 X magnification (n=7). Paxillin area was measured using 7 different images per group (n=7) captured at 40X magnification. A single cell in each image was analyzed for paxillin area quantification.

2.2.3 Traction force microscopy

Cell traction was calculated using constrained Fourier transform traction microscopy (FTTM) [189]. 0.2 μm amino-modified fluorescence microbeads were conjugated to the substrates due to the presence of anhydride groups on the substrates' surface. hASCs (2×10^3/well) were seeded on substrates of varying stiffness and containing microbeads and allowed to grow for 24 hours. Fluorescence images of the microbeads were taken before and after cell detachment from the substrates by trypsinization. The corresponding displacement field was calculated using a customized Matlab code. The traction force was calculated based on the displacement field computed from 7 images for each group (n=7). A single cell in each image was analyzed for traction forces measurements.

2.2.4 Plasmid construct design

The pscAAV-GFP vector (John T. Gray, Addgene plasmid #32396) harboring the enhanced green fluorescent protein (EGFP) gene was digested with BamHI and NotI restriction enzymes (New England BioLabs, Ipswich, MA) to excise the EGFP gene. The pCMV6-XL5 mammalian expression vector (Origene Technologies, Rockville, MD) was digested with BamHI and NotI enzymes, and after purification, the linearized EGFP gene was ligated with the pCMV6-XL5

expression vector using T4 DNA Ligase (Promega). The resulting construct, pCMV-GFP, was transformed in chemically competent DH5α *Escherichia coli* (Invitrogen, Carlsbad, CA) to amplify the plasmid. Additionally, the expression vector for the human VEGF-165 gene, pCMV6-XL5-VEGF (Origene Technologies, Rockville, MD), was also amplified by the transformation of DH5α *E. coli*. Both plasmids were extracted and purified using QIAPrep Spin Midiprep kits (QIAGEN Inc., Germantown, MD).

2.2.5 Lipofectamine-plasmid DNA complex formation and characterization

Prior to transfection, both plasmid DNA and Lipofectamine2000 (Invitrogen, Carlsbad, CA) were diluted in 150 µL of incomplete α-MEM media. Specifically, the lipoplexes were prepared by mixing the two components in equal volumes (150 µL) containing a 1:3 ratio of plasmid DNA (4 µg) to Lipofectamine2000 (12 µL). The complexes were then incubated for 20 minutes at room temperature before addition to hASCs. The hydrodynamic diameter and the zeta potential of the Lipofectamine2000 and the lipoplexes were obtained using a ZetaPALS zeta potential analyzer (Brookhaven Instruments Corporation). Samples for DLS analysis were prepared by diluting Lipofectamine2000 and the lipoplexes in Opti-MEM (Thermo-Fisher Scientific, USA). On the contrary, zeta potential measurements were carried out by diluting the samples in KCl 1mM.

2.2.6 Transfection of hASCs

hASCs were seeded on the different silicone substrates (10^5 cells/well) and allowed to proliferate for 24 hours prior to transfection. hASCs were cultured in complete α-MEM (15% FBS and 1% penicillin/streptomycin) at 37 °C and 5% CO_2. The growth medium was replaced with fresh α-MEM (2 mL/well) without FBS, and the complexes of Lipofectamine2000 and plasmid DNA (300

μL/well) were added dropwise to the cells (80-90% confluency). After incubation for 1 and 4 hours at 37°C, the media containing the complexes was removed and replaced with complete α-MEM. Cells were cultured for 72 hours prior to changing the media, and further analysis was conducted to evaluate the quantity of VEGF secreted by the cells.

Similarly, GFP transfection of hASCs was carried out using Lipofectamine2000 according to the conditions reported above. Cells were cultured for 24 hours prior to fluorescence-activated cell sorting (FACS) analysis. Briefly, cells were trypsinized 24 hours post-transfection and suspended in PBS at the cell density of 1×10^5 cells/mL. The percentage of GFP positive hASCs and corresponding mean fluorescence intensity (MFI) values were determined using the Attune NxT flow cytometer (Thermo-Fischer Scientific, USA). Three different samples per group were analyzed, and the results were reported as mean ± deviation standard. Additionally, fluorescent and corresponding phase-contrast (10X) images were captured by EVOS cell imaging system (Thermo-Fischer Scientific, USA).

2.2.7 Assessment of plasmid internalization by qPCR analysis

hASCs seeded on soft and stiff substrates were transfected for 1 hour using the GFP plasmid. Cells were thoroughly washed several times with PBS to remove the excess of the plasmid. Cells were then trypsinized and counted to obtain a final cell suspension of 1×10^3/mL. Cells were centrifuged at 1000 rpm for 5 minutes, and the corresponding pellets were resuspended in 100 μL PBS and freeze-thawed to lyse the cell membrane at -80 °C [190]. One microliter of this lysate suspension containing the plasmid was mixed with 10 μL KiCqStart SYBR Green Master Mix, 2 μL of the forward and reverse primer for GFP gene and 5 μL of RNAse-free water. All of the reactions were performed using a Mastercycler Realplex (Eppendorf, Germany). The quantity of plasmid

internalized by the cells in each group was quantified using a calibration curve obtained in the range of 0.9 ng to 30 ng of GFP plasmid. Each dilution of the GFP-plasmid was generated using a suspension of the non-transfected hASCs lysate (1×10^3/mL). Additionally, GFP-plasmid dilutions were also obtained in RNAse-free water to detect undesired contamination. Samples were measured in triplicate for each dilution (n=3).

2.2.8 Evaluation of plasmid internalization using fluorescent-labeled plasmid-Lipofectamine lipoplexes

The plasmid was labeled with red fluorescent Rhodamine using the Label IT® Tracker™ intracellular nucleic acid localization Kit CX-Rhodamine (Mirus, WI, USA) to visualize the plasmid internalization. The process of labeling was achieved following the established protocol provided by the kit. The labeled plasmid was complexed with Lipofectamine2000 following the procedure reported above. hASCs were transfected for one hour, followed by thorough washing with PBS to remove the non-internalized plasmid. Fluorescent and corresponding phase-contrast (40X) images were captured by EVOS cell imaging system (Thermo-Fischer Scientific, USA). Cell boundaries were defined based on phase-contrast images. The fluorescence intensity was quantified based on the integrated density values of each cell using ImageJ. Results were reported as mean ± standard deviation (n = 5) and normalized to the number of cells.

2.2.9 qPCR investigation of caveolin and clathrin genes

Expression of caveolin and clathrin-mediated genes by hASCs was evaluated using qPCR after 1 and 4 hours post-transfection on the soft (0.5 kPa) and stiff substrates (32 kPa). mRNA was extracted from the cells using an RNeasy Mini Kit (Qiagen, Germany) and quantified using a

NanoDrop spectrophotometer (Thermo Scientific, USA). Next, mRNA samples were converted to cDNA using the High-Capacity cDNA Conversion Kit (Applied Biosystems, USA). Lastly, gene expression was measured using a cocktail of predesigned primers and the KiCqStart SYBR Green Master Mix (Sigma Aldrich, USA). All of the reactions were performed using a Mastercycler RealPlex (Eppendorf, Germany). The fold expression levels were calculated using the relative ΔΔCt method. *GAPDH* was considered as the housekeeping gene, and the results were normalized based on the gene expression of hASCs cultured on the softer substrates.

2.2.10 VEGF quantification by ELISA

hASCs (10^5 cells/well) were seeded on 6-well plate silicon hydrogels coated with 1% w/v of gelatin type A and allowed to grow in α-MEM (2 mL) supplemented with 15% FBS and 1% penicillin/streptomycin (Thermo-Fisher Scientific, USA) at 37 °C and 5% CO_2. Cells at 70-80% confluency were transfected with VEGF-165 plasmid using Lipofectamine2000 reagent in incomplete α-MEM. Supernatants were collected 72 hours after transfection. Quantification of VEGF expression was carried out using an enzyme-linked immunosorbent assay (ELISA, R&D Systems, Minneapolis, MN) according to the manufacturer's protocol. The amount of VEGF released was quantified by ELISA using a standard calibration curve ranging from 32 pg/mL to 1 ng/mL. Results were normalized based on the concentration of VEGF obtained from the media recovered after 72 hours in the soft substrates (n=3).

2.2.11 HUVEC migration assay

Human umbilical vein endothelial cells (HUVECs) (Lonza, Walkersville, MD) between passages 6-9 were cultured in 24 well plates (2×10^4 cells/well) in endothelial growth medium (400 µL)

(EGM-2 BulletKit, Lonza, Walkersville, MD) without the addition of VEGF and rhFGF-B. After reaching confluency, scratches were made in the cell monolayer using a cell scraper. Cells were washed thoroughly with PBS to remove all the floating cells. Media containing VEGF was collected from stiff and soft substrate groups after 72 hours of transfection (100 µL). Then, HUVECs were allowed to migrate through the scratch for 12 and 24 hours. Cells were stained with calcein, and corresponding fluorescent images were taken in the same positions along with the scratch at 12 and 24 hours. HUVECs that did not receive any growth factors were considered as control groups. The percentage of area covered by HUVECs during the migration was calculated using ImageJ software. The original scratch area was calculated based on preliminary images taken immediately after the scratch was formed (n=3).

2.2.12 Statistical analysis

Statistical analysis for area calculation covered by HUVECs in the scratch assay was performed using one-way analysis of variance (ANOVA) followed by Tukey's multiple comparison test to determine any significant differences between groups at each time point. For all other analyses, a t-test (non-parametric) was used to compare two groups. All analyses were carried out with GraphPad Prism. A p-value of less than 0.05 indicates statistical significance.

2.3 Results and discussion

2.3.1 Effect of substrate stiffness on the cell morphology

As the first step of our investigation, we studied the effect of gelatin-coated silicon hydrogel stiffness on the morphology and cytoskeletal arrangement of hASCs. Soft (0.5 kPa) and stiff (32 kPa) substrates were chosen to resemble the stiffness of adipose and bone tissues, respectively [191]. hASCs displayed a diverse morphology on the different substrates, as indicated by immunofluorescent staining (**Figure 2.1A** and **Figure S2.1**). Cells seeded on the stiffer hydrogels showed an elongated morphology characterized by a larger surface cell area (4173 μm^2) with respect to the hASCs on the softer hydrogels (2195 μm^2) (**Figure 2.1B**). Additionally, paxillin staining was carried out to investigate the differences in cell focal adhesion expression [192]. A greater focal adhesion area was observed for the hASCs seeded on the stiff hydrogels, and this result is congruent with previous reports that investigated paxillin expression in other cells lines [193] (**Figure 2.1C**). Aside from a change in the focal adhesion area, a higher number of actin stress fibers was quantified in the hASCs on the 32 kPa hydrogels (**Figure 2.1D**). Similar results were also found in a study comparing the percentage of actin stress fibers in human fibroblasts seeded on poly(dimethylsiloxane) and polyacrylamide hydrogels presenting stiffness values ranging from 5 kPa to 2 MPa. Fibroblasts seeded on the stiffer matrix presented a more aligned distribution of F-actin and a higher cell area [193].

Additionally, the average local stress magnitude exerted by the cells on the substrates was calculated based on constrained Fourier transform traction (FTTM). Results confirmed that hASCs seeded on stiffer hydrogels displayed a higher traction force with an increase in the mean value from 0.5 MPa to 5.7 MPa (**Figures 2.1E-F**). This difference can be attributed to the increase in

tension within the networks of actin fibers in the cell's cytoskeleton, and furthermore, the cells on stiffer substrates exhibited reduced cytoskeletal mobility.

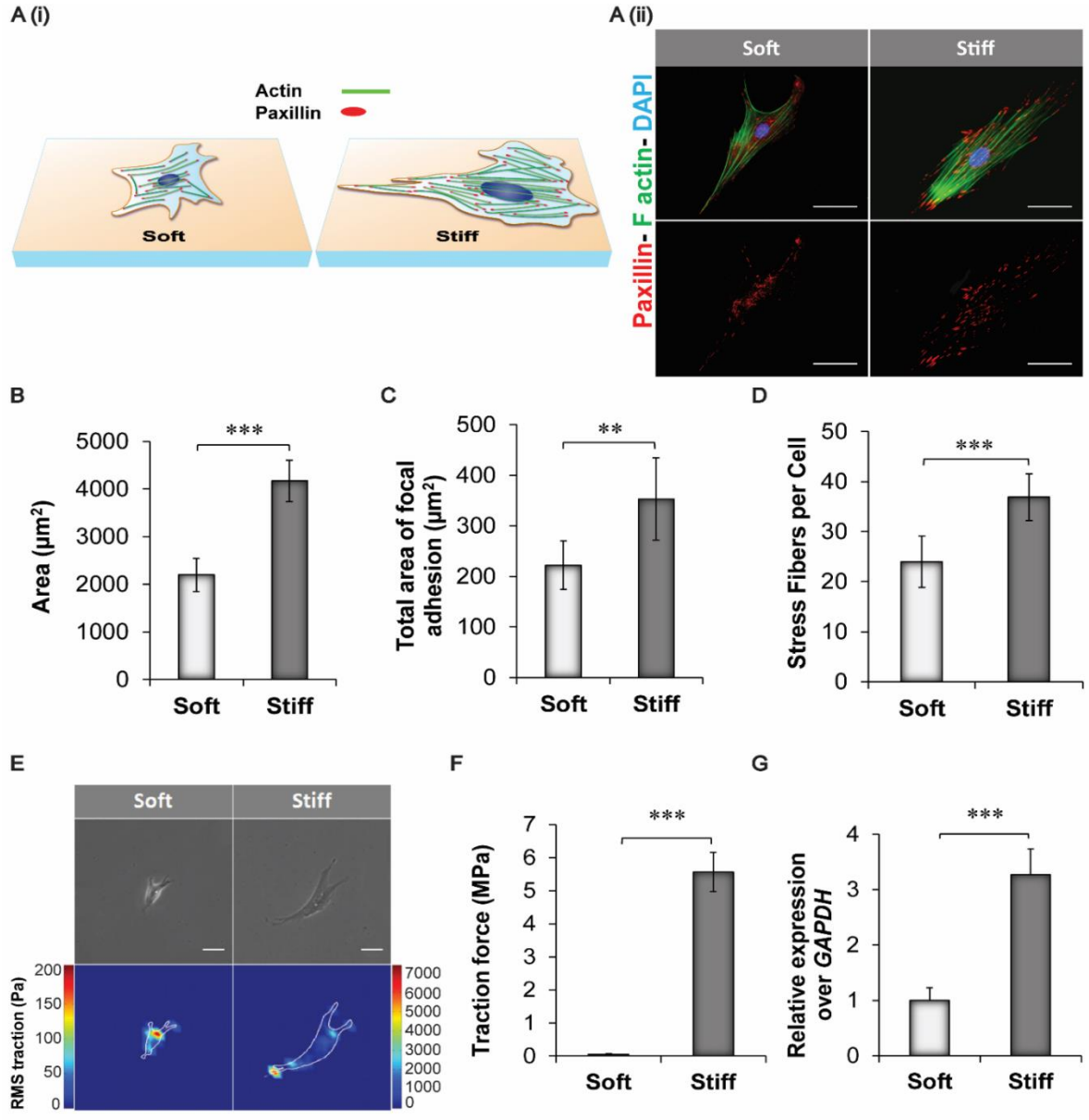

Figure 2.1 Influence of substrate stiffness on hASC morphology and cytoskeletal remodelling. A) (i) Schematic representing the main changes in cytoskeletal composition and focal adhesion distribution observed by culturing hASCs on soft and stiff hydrogels. Cells cultured on softer substrates displayed reduced cell surface area, lower total area of focal adhesions, and reduced formation of actin filaments. (ii) Immunofluorescence staining of hASCs seeded on soft (0.5 kPa) and stiff (32 kPa) silicon hydrogels pre-coated with a solution of gelatin 1% w/v. Cells were stained with Alexa Fluor 488 Phalloidin to visualize actin stress fibers (green) and with Diamidino-2-phenylindole dilactate (DAPI) to stain the nuclei (blue). In addition, paxillin staining (red) was carried out to identify the area of focal adhesion. Scale bar = 50 µm. B) Quantification of cell area

of hASCs cultured on the two different substrates. Results are reported as mean ± standard deviation (n=10). C) Quantification of the total area of focal adhesions expressed by hASCs on the different substrates. Results are calculated based on the red fluorescence intensity obtained from the immunofluorescent staining for paxillin expression (n=7). D) Actin stress fibre quantification obtained by counting the number of actin stress fiber on each cell at 40X magnification. Results are reported as mean ± standard deviation (n=9). E) Phase contrast pictures and traction map images of hASCs cultured on soft and stiff silicone hydrogels. Scale bar = 80 μm. F) Root-mean-square (RMS) traction values of hASCs indicated an increase in cell traction on the stiffer substrate (n=7). G) *RhoA* gene expression in hASCs seeded on the different substrates after 24 hours. Results were normalized based on the gene expression of cells cultured on the softer substrates (0.5 kPa) n=3. Results are reported as mean ± standard deviation * = $p < 0.05$, ** = $p < 0.01$ and *** = $p < 0.001$.

This change in mobility is also evident by the increase in measured traction forces [189, 194]. These findings were further confirmed by qPCR analysis. Specifically, we evaluated the expression of *RhoA* gene, which regulates the assembly of both contractile actomyosin filaments and focal adhesion complexes. *RhoA* was found to be upregulated in the 32 kPa group with a 2.1-fold increase compared to the softer hydrogel group (**Figure 2.1G**) [195].

2.3.2 Effect of substrate stiffness on the intracellular internalization of Lipofectamine/plasmid complexes

After studying the effects of substrate stiffness on cell activity and cytoskeletal remodeling, we proceeded to evaluate the effects of substrate stiffness on the efficiency of gene delivery to hASCs. Following our previous observations, we hypothesized that an increase in the number of actin stress fibers would promote the internalization of the Lipofectamine-DNA complexes (lipoplexes) and therefore increase the transfection efficiency (**Figure 2.2A**). The Lipofectamine used in this study has a mean diameter of 346.96 ± 34.42 nm and a positive zeta potential value of 15.65 ± 0.89 as measured by dynamic light scattering (DLS) analysis. Rhodamine-tagged plasmids were electrostatically complexed with Lipofectamine, and DLS analysis confirmed the formation of the

complex (**Figure 2.2B**). For instance, the lipoplexes displayed an increase in the mean diameter value as well as a change in the zeta potential measurement from positive to negative values. Similar results were found in other reports investigating the formation of a complex between plasmid DNA and cationic liposomes [196]. The lipoplexes were used to transfect hASCs seeded on the soft and stiff silicon hydrogels. The process of internalization was evaluated one hour post-transfection. Subsequently, cells were imaged to visualize the quantity of plasmid internalized (**Figure 2.2C**). Quantification of the fluorescence intensity of the rhodamine-tagged plasmid revealed a higher presence of plasmid DNA in the hASCs cultured on the 32 kPa hydrogels. A three-fold increase in the fluorescent intensity was detected in the more rigid hydrogels with respect to the softer substrates (**Figure 2.2D**). This trend was further confirmed by qPCR analysis to determine the quantity of plasmid that was internalized into the cells (**Figure 2.2E**) [190]. The amount of plasmid internalized was measured based on a calibration curve obtained by qPCR analysis of different concentrations of GFP plasmid (0.9 ng to 30 ng) in the cell lysates (Figure S2.2). As proof of concept, we also transfected hASCs with a green fluorescent protein (GFP) plasmid using Lipofectamine. hASCs seeded on the stiff substrates displayed a higher GFP expression as confirmed by FACS analysis and fluorescent imaging of GFP positive fluorescent cells (**Figure S2.3**). Our findings suggest that the differences in cell morphology and cytoskeletal remodeling play a fundamental role in influencing the cell's ability to uptake the lipoplexes. These results are in agreement with other reports studying the effects of matrix elasticity as the main mediator of cellular endocytosis in other cell lines. For instance, fibroblasts, myoblasts, and bone marrow stromal cells displayed higher internalization of fluorescently labeled DNA when seeded on the stiffer fibronectin-conjugated poly(ethylene glycol) diacrylate hydrogels (670 kPa) with respect to cells seeded on softer substrates [197].

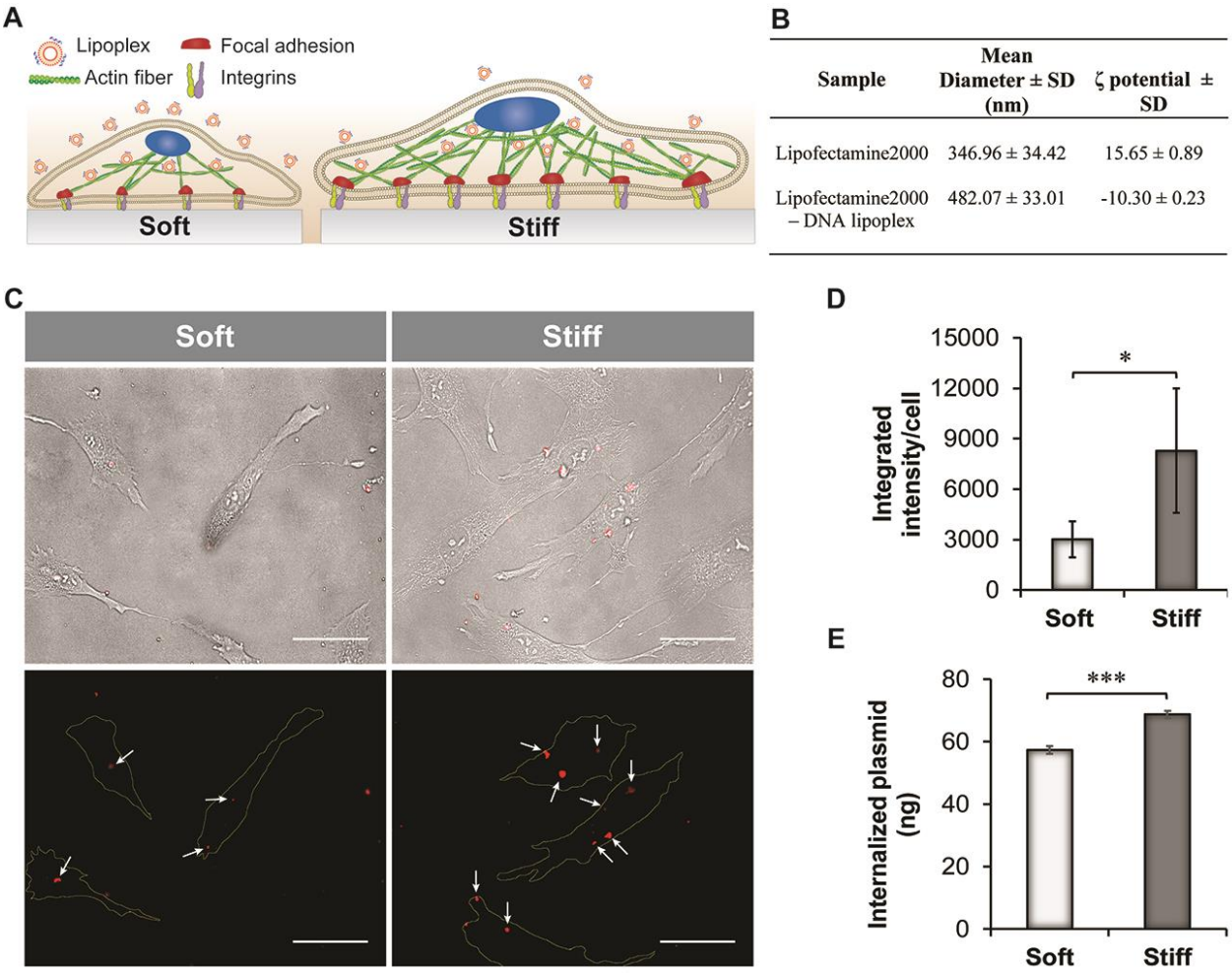

Sample	Mean Diameter ± SD (nm)	ζ potential ± SD
Lipofectamine2000	346.96 ± 34.42	15.65 ± 0.89
Lipofectamine2000 – DNA lipoplex	482.07 ± 33.01	-10.30 ± 0.23

Figure 2.2 Effect of substrate stiffness on lipoplexes internalization. A) Schematic indicating the internalization efficiency of lipoplexes on hASCs adhering to substrates with different stiffness. Cells seeded on 32 kPa substrate internalized a higher quantity of plasmid DNA. B) Mean diameter and ζ-potential results obtained by DLS analysis of Lipofectamine2000 and lipoplexes. C) Bright field images of hASCs seeded on soft and stiff substrates show the presence of internalized red-fluorescent lipoplexes. Scale bar = 50 µm. Corresponding fluorescent images displaying the red fluorescent complexes (white arrows). Cell boundaries are shown with a yellow line in the fluorescent images. Scale bar = 50 µm. D) Quantification of the fluorescence intensity of the rhodamine-tagged plasmid performed using image analysis (n=5). E) Quantification of plasmid internalization in hASCs seeded on soft and stiff substrates by qPCR analysis. Results are reported as mean ± standard deviation (n=4). * = $p < 0.05$, ** = $p < 0.01$ and *** = $p < 0.001$.

2.3.3 qPCR analysis of caveolin and clathrin genes

We also investigated the expression of the genes involved in endocytosis to define the role of actin stress fibers in regulating the internalization of the lipoplexes. We studied the gene expression of several key proteins directly involved in both caveolae and clathrin-mediated endocytosis pathways since both uptake mechanisms are commonly activated in the presence of Lipofectamine2000 complexes [198]. The genes and primers used as well as the functions of each gene have been reported in the supplementary info (**Table S2.1**, **Table S2.2**, Supporting Information). The gene expression profile of hASCs was evaluated 1 hour and 4 hours post-transfection with lipoplexes. These two different times points were selected based on previous studies investigating the trafficking processes of the lipoplexes within the cytosol. Lipoplexes commonly bind with the cell membrane followed by association with actin fibers within the first hour upon transfection. Subsequently, lipoplexes can migrate to the perinuclear region through

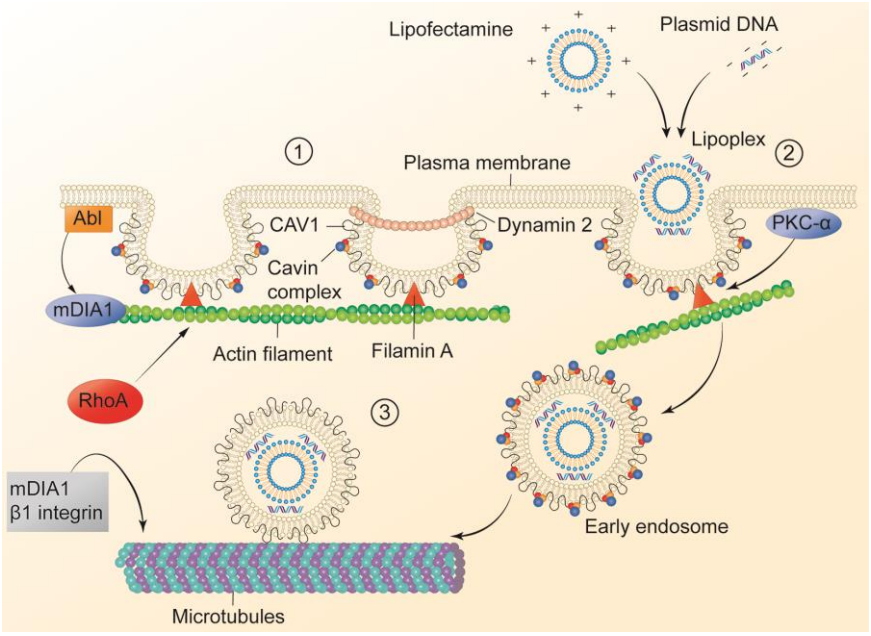

Figure. 2.3 Schematic of the process of endocytosis through caveolae-mediated pathway. This process is divided into three steps: (1) Dynamic of caveolae at the plasma membrane, (2) Caveolae internalization by actin fibers stress and (3) endocytotic trafficking by microtubules

active transport using microtubules within the next four hours, as shown in other reports (**Figure 2.3**) [199].

According to the qPCR results, caveolin-mediated genes were upregulated in the cells cultured on the 32 kPa substrate (**Figure 2.4A**), which confirmed the role of substrate stiffness as an indirect regulator of endocytosis. Specifically, Filamin A (*FLNA*) and Abl tyrosine kinases-1 (*ABL1*) genes were more expressed in hASCs cultured on the stiffer silicon hydrogels. Both genes are essential regulators of caveolae formation and migration. Filamin A is a protein that participates in the later migration of caveolae membrane and regulates the interaction between caveolin 1 (*CAV1*) and actin stress fibers. A depletion of the *FLNA* gene is commonly associated with an alteration in the caveolae dynamic and a reduction in the caveolae formation. Additionally, Abl tyrosine kinase-1 controls the polymerization of actin stress fibers and regulates actin interaction with *CAV1*. *CAV1* and *CAVIN1* genes were instead only upregulated after 4 hours, indicating a later expression of these proteins essential for caveolae formation. The higher upregulation of all the selected genes is justified by the increased presence of actin fibers in hASCs cultured on the stiffer hydrogels. Finally, β1 Integrin *ITGB1* was upregulated after 1 hour of transfection in the 32 kPa group, which is indicative of stabilization of microtubules that are involved in the cellular trafficking of caveolae and recycling of *CAV1* to the plasma membrane [18, 185]. Overall, the upregulation of all the analyzed genes can be explained by the greater presence of well-aligned actin fibers in the hASCs seeded on the stiffer substrates.

On the contrary, no significant differences were found among clathrin-mediated genes in the two tested groups (**Figure 2.4B**). A possible explanation is that actin only plays a primary role in the caveolin-mediated pathway, while its contribution to clathrin-mediated endocytosis is reported to

be secondary. For instance, actin is not necessary to promote endocytosis of transferrin, which is a common ligand used to investigate clathrin-mediated endocytosis.

Another explanation for the predominance of a caveolin-mediated pathway is that the size of the lipoplexes used in this study was larger than 200 nm (482.07 ± 33.01 nm) as evaluated by DLS analysis. Clathrin-mediated endocytosis becomes the predominant mechanism of internalization only with nanomaterials characterized by a diameter of less than 200 nm [200].

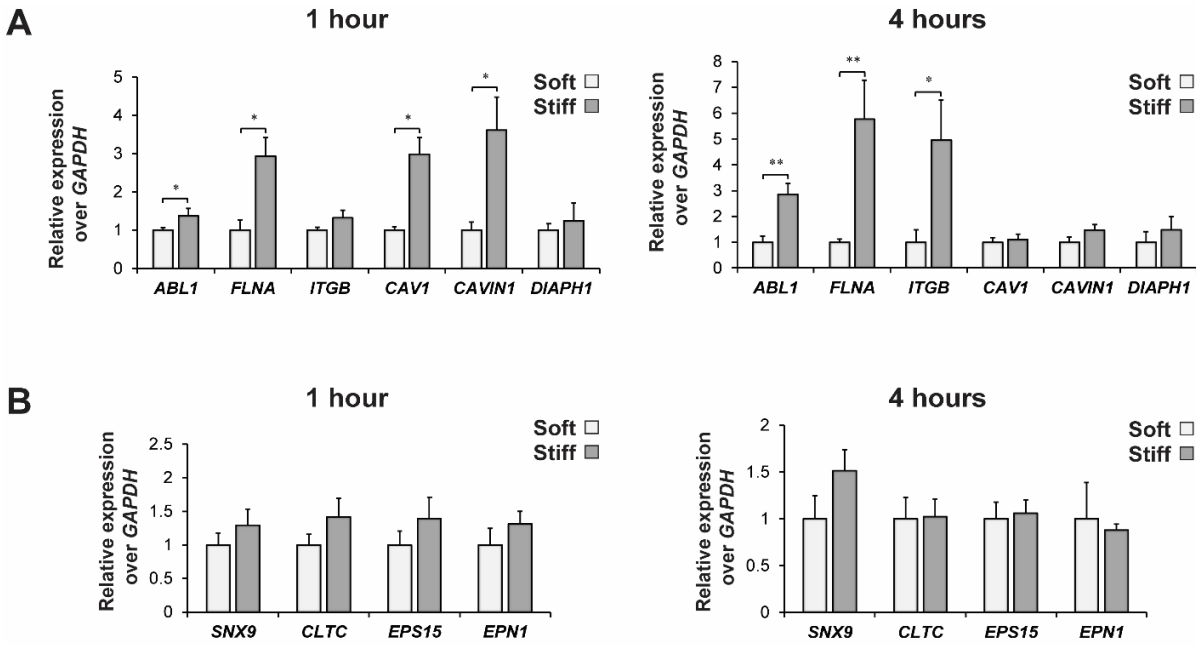

Figure 2.4 qPCR analysis of caveolin and clathrin genes regulating the process of endocytosis of lipoplexes. A) Fold increase expression of the main genes involved in caveolin endocytosis pathways after 1 and 4 hours of lipoplexes internalization. B) Fold increase expression of the main genes regulating clathrin endocytosis pathways after 1 and 4 hours of lipoplexes internalization. Results are normalized based on the gene expression of hASCs cultured on the soft substrate (0.5 kPa) (n=3). *= $p < 0.05$, ** = $p < 0.01$.

2.3.4 Evaluation of VEGF secretion and activity

Finally, we evaluated how the changes in plasmid internalization affected the cell's ability to transiently express angiogenic growth factor. hASCs seeded on the different substrates were

transfected with plasmid DNA encoding for the human VEGF-A gene.

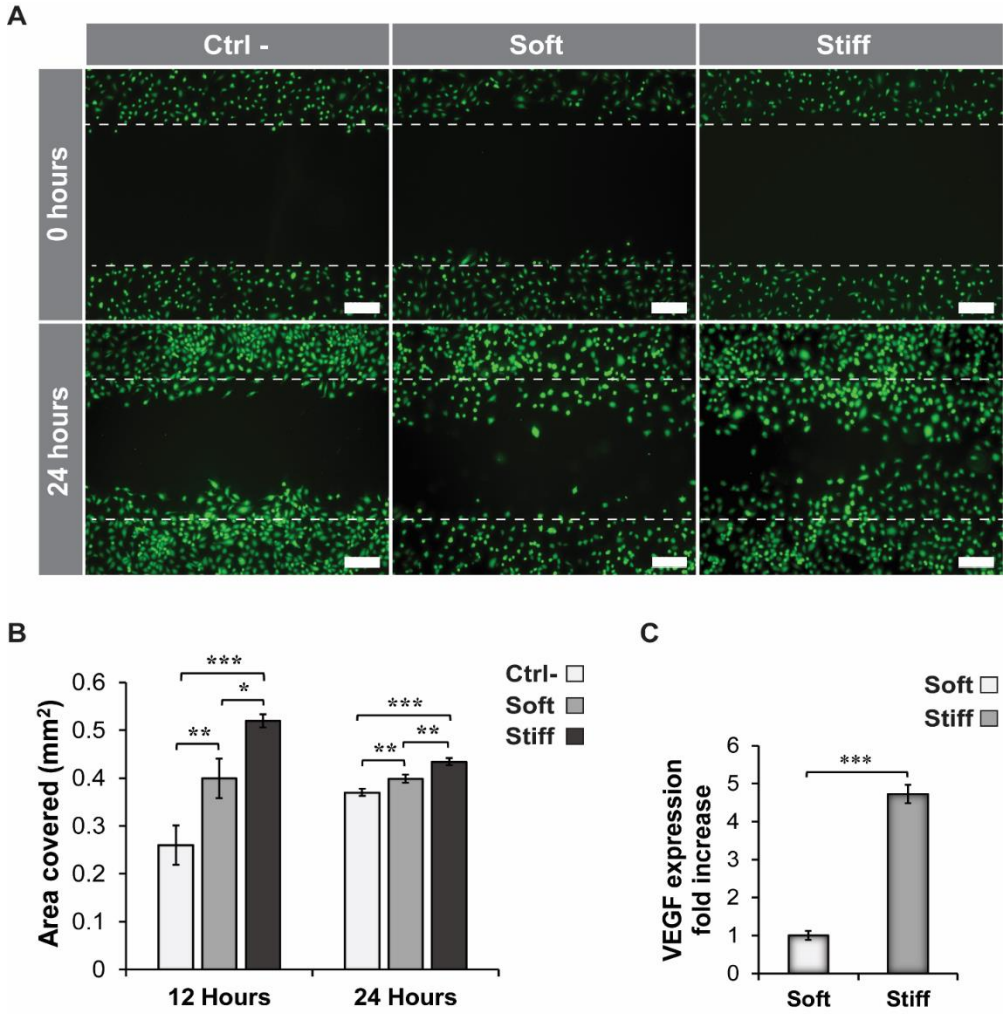

Figure 2.5 Modulation of VEGF expression of hASCs transfected on silicon hydrogels with different stiffness. A) Fluorescence images of HUVECs stained with calcein. Scratches were made at time zero on HUVEC monolayer. Cells were allowed to migrate into the void area for 24 hours. The conditioned media in the soft and stiff group was supplemented with VEGF secreted by hASCs after 72 hours post-transfection. No VEGF and recombinant human fibroblast growth factor-B (rhFGF-B) were present in the media of the control group (Ctrl-). Scale bar = 200 µm. B) Quantification of the surface area covered by HUVECs after proliferation through the original scratches at 12 and 24 hours. The area covered was calculated based on the original area of the scratches at time zero. C) Quantification of VEGF expression by ELISA after 72 hours post-transfection. Results are normalized based on the VEGF expression of hASCs cultured on the soft substrate (0.5 kPa).*= $p < 0.05$, ** = $p < 0.01$, *** = $p < 0.001$.

While hASCs possess a natural ability to produce angiogenic growth factors, this inherent capability can be augmented by using gene delivery and controlling the physical properties of the substrate on which hASCs are seeded [201].

Higher gene transfection efficiency observed in hASCs cultured on the stiffer substrates resulted in a greater production of VEGF, which was evaluated by human umbilical vein endothelial cells (HUVEC) migration assay and ELISA quantification [202]. HUVEC migration was monitored over time, and a larger migration area was evident after 24 hours in the group exposed to VEGF produced by hASCs cultured on the 32 kPa hydrogels (**Figure 2.5A**-B). Finally, a four-fold increase in VEGF concentration was found in the media of the 32 kPa sample compared to the 0.5 kPa group after 72 hours (**Figure 2.5C**).

2.4 Conclusions

This study highlights the importance of substrate stiffness as an essential regulator of cellular cytoskeletal remodeling and internalization of exogenous genes in hASCs. hASCs displayed a higher cell area, increased focal adhesion expression, and a greater amount of actin stress fibers when seeded on stiffer substrates (32 kPa). These changes in cellular morphology and cytoskeletal organization directly controlled the process of lipoplexes delivery. Specifically, the role of actin stress fibers in the process of endocytosis of lipoplexes has been confirmed, defining its direct contribution in plasmid internalization. Genes involved in the regulation of caveolae-mediated endocytosis were upregulated in hASCs seeded on stiffer substrates 4 hours post-transfection.

These interesting findings have been directly implemented to augment the angiogenic potential of hASCs. hASCs normally secrete VEGF as one of the regulators of their proliferation and differentiation into adipogenic, chondrogenic, and osteogenic lineages [203]. The secretion of this growth factor can be controlled by nanocarrier-based gene delivery to obtain a selective angiogenic protein expression [204]. In this study, we have successfully demonstrated how the efficiency of a conventional transfection approach based on Lipofectamine2000 can be augmented simply by altering the stiffness of the substrate. Precisely, upon transfection with a plasmid encoding for VEGF, we observed a higher VEGF secretion for hASCs seeded on the stiffer substrates. Overall, these findings demonstrate how it is possible to control specific cellular functions and augment gene intracellular delivery by using lipid-based carriers.

CHAPTER 3. Intracellular delivery of exogenous macromolecules into human mesenchymal stem cells by double deformation of the plasma membrane

Abstract

Physical techniques for intracellular delivery of exogenous materials offer an attractive strategy to enhance the therapeutic efficiency of stem cells. However, these methods are currently limited by poor delivery efficiency as well as cytotoxic effects. Here, a high throughput microfluidic device is designed for efficient (~85%) cytosolic delivery of exogenous macromolecules with minimal cell death (less than 10%). The designed microfluidic device enables the generation of transient pores as the cells pass through the micron-sized constrictions (6-10 μm), leading to the passive diffusion of extracellular cargos into the cell cytosol. Specifically, the microfluidic system is designed to induce a double deformation on the cell membrane at the squeezing zones to maximize intracellular delivery. Additionally, the flow rate, ionic concentration, and the molecular weight of the cargo are optimized for maximum efficiency. The optimized device enables cytosolic diffusion of small (3 kDa) and large molecules (70 kDa) without inducing any apoptotic effect. Overall, this double cell deformation platform offers new opportunities to rapidly and efficiently deliver extracellular cargo into stem cells without affecting their viability and functionality.

Modaresi S., Pacelli S., Subham S., Dathathreya K., Paul A., Intracellular delivery of exogenous macromolecules into human mesenchymal stem cells by double deformation of the plasma membrane, Advanced Therapeutics, 2019.

3.1. Introduction

Intracellular delivery of exogenous materials can be useful for many research applications ranging from gene therapy, cancer treatment, and cellular tracking for diagnostic purposes [205-210]. However, the method of delivery should be efficient and selective without compromising cell viability or cell functionality. Various approaches have been investigated to promote the intracellular delivery of macromolecules, including carrier-based strategies as discussed in the previous chapters [176].

Alternative solutions are the ones that provide the permeabilization of the cell membrane to enable the passive diffusion of extracellular cargo. For example, electroporation and sonoporation take advantage of the disruption of the plasma membrane using different sources of energy to directly deliver target molecules into the cytoplasm. In sonoporation techniques, the cells vibrate at a constant frequency by continuous ultrasound waves. As a result, gas bubbles are formed in the liquid, leading to an increase in cell membrane permeability [165, 169]. The limitation associated with this technique is the need for strong ultrasound pulses to promote high internalization efficiency, which causes extensive plasma membrane damage and cell death (50% viability) [134, 211]. Additionally, electroporation is another method that generates rapid high-voltage electric pulses to form an electric field responsible for the formation of temporary pores [139]. However, the intense electrical fields can cause significant damage to the delivered cargo as well as denaturation of intracellular proteins [159, 212, 213].

Creating small transient pores in the cell membrane by simple mechanical deformation can also offer a new paradigm for rapid and effective delivery of exogenous macromolecules of interest [214]. As reported by other groups, this can be achieved by passing the cells through micron-sized constrictions [215, 216]. The deformations generate transient pores on the cell surface, leading to

passive diffusion of extracellular cargos into the cytosol [172, 173, 217]. Depending on the dimensions of the target cell, precise control on cell deformation can be achieved by squeezing them through different types of geometries with constrictions that are approximately half of the cell diameter [171, 218]. This technique offers the advantage of being rapid and efficient without the need for a costly apparatus or an external source of energy. In fact, the driving force required for the disruption of the cell membrane can be supplied primarily by the flow of the cell suspension passing through the channels of the microfluidic chips.

In this work, we report an efficient and high throughput strategy to deliver extracellular cargos into human mesenchymal stem cells by a double deformation of the cell membrane (i.e., 2-step deformation). Particularly, we have fabricated and tested two different microfluidic designs to generate the pore formation and induce passive diffusion of extracellular cargos into human adipose-derived stem cells (hASCs). This cell source was selected for the study because of their ease of harvest [130], and great potential in regenerative medicine, as shown in promising pre-clinical and clinical trials [219-222]. The applicability of this new technique on other cell types, such as NIH 3T3 fibroblasts, were also tested. Several parameters, such as the chip geometry, flow rate, gap size, as well as the ionic concentration in the delivery medium were optimized to enhance internalization efficiency. Different molecular weights of the model macromolecule dextran fluorescein isothiocyanate (Dex-FITC) were tested to determine the suitable size range of cargo that could be delivered using the fabricated microfluidic chips. High cell viability (higher than 90%), limited cell apoptosis, and preservation of stemness were achieved using the optimized microfluidic device. Furthermore, the study investigates the expression of several genes involved in the process of cytoskeletal remodeling and membrane resealing post-deformation using the microfluidic chip. Overall, here we present a potentially transformative cellular engineering tool

to drastically enhance intracellular delivery of exogenous macromolecules without compromising cell viability and their functionality.

3.2. Materials and Methods

3.2.1. Fabrication of the silicon master molds

As the first step, a silicon wafer was treated with hexamethyldisilazane (HMDS) for 30 minutes at 150ºC before the coating with a thin film of the SU-8 2015 negative photoresist (Microchem, Newton, MA). After treatment, the wafer was allowed to cool at room temperature. A photoresist was applied on the pre-treated wafer using a spin coater rotating at 3000 rpm for 30 seconds to obtain a layer with a thickness of 15 µm. The wafer was subsequently heated at 65°C for 2 minutes and at 95°C for an additional 2 minutes to evaporate the solvent from the SU-8 layer (soft baking) prior to UV crosslinking (Photronics, INC). Two distinct chrome-coated photomasks have been generated by using AutoCAD (Autodesk), and the pattern was transferred to the silicon wafer using contact type mask aligner (ABM, Inc.). UV light at 365 nm was used to crosslink the photoresist and the time of exposure (5-10 seconds) was varied based on the energy level of the UV lamp, which was checked before each UV treatment. Subsequently, the UV-treated wafers were baked at 95°C for 10 minutes to ensure the completion of the crosslinking process. The non-crosslinked photoresist was removed by washing the wafer in the SU8-developer solvent. Finally, the developed wafer was cured at 150°C for 2 hours (hard bake) to anneal any surface cracks that are evident after development. The successful fabrication of the micro-constrictions with the correct geometry and size was confirmed by visual inspection using a bright field microscope. Master molds on the wafer containing micro-constrictions displaying a gap distance larger or smaller than 1 µm with respect to the optimal value were discarded. Additionally, the thickness of

the master molds was monitored with a profilometer to ensure the obtainment of channels with a height of around 15±1 µm. Overall, two separate geometry designs have been fabricated with distinct scatter and squeezing areas. The micro-constrictions gaps were varied from 6 to 10 µm to ensure efficient cell squeezing.

3.2.2 Fabrication and characterization of the PDMS microfluidic chips

The SU8-2015 master molds prepared, as described in section 2.1 were used to fabricate the microfluidic chips made of polydimethylsiloxane (PDMS). Before the addition of the PDMS pre-polymer solution, the surface of the silicon SU8-2015 molds was treated with trimethylchlorosilane (TMCS) for 30 minutes in a vacuum chamber. This step was necessary to ensure the easy removal of the PDMS from the wafer after the curing process. The PDMS prepolymer solution and the curing agent (Sylgard 184 silicone elastomer kit, Dow Corning) were mixed in a 10:1 ratio. The mixture was de-gassed and poured onto the silicon master molds and cured at 75°C for 3-4 hours. After careful removal of the cured PDMS from the wafer, holes of 1 mm in diameter were punched in the PDMS to create the corresponding inlets and outlets of the final microfluidic chips. Finally, an oxygen plasma treatment for 40 seconds was used to bond the PDMS mold to the glass slides and seal the microfluidic channels. The bonded devices were kept at 90°C for 3 hours to ensure permanent bonding. Tygon tubes (1/16 OD × 0.02" ID) were inserted in the inlet and outlet holes of the PDMS chips using isopropanol to secure the insertion of the tubes. The PDMS chips were placed on a holder with double-sided conductive carbon tape sputter-coated with gold (35 mm) to visualize the channels and confirm the correct size of the different micro-constrictions. The microfluidic chips were imaged at an acceleration voltage ranging from 1 to 10 kV with an in-lens detector using SEM.

3.2.3 COMSOL analysis of the flow velocity in the microfluidic chips

COMSOL simulation was performed to ensure that the flow velocity was uniform in every channel of both microfluidic devices. The input velocity for the simulations was calculated based on the flow rate and the corresponding device geometry used during each experiment. Simulations were run in laminar flow conditions considering water as the fluid. Series of simulations were performed with a different number of elements to check for convergence.

3.2.4 Evaluation of calcium and PBS concentration on the delivery efficiency of Dex-FITC

hASCs (passages 2-5) were collected from the flasks by trypsinization. The cell suspension in α-MEM was subdivided into small aliquots containing 200,000 cells each. hASCs were centrifuged at a speed of 1.5 g for 5 minutes. The media was discarded, and the pellet was resuspended in 0.5 mL PBS 1X containing three different amounts of $CaCl_2$ (0, 1 and 2mM) and dextran fluorescein-isothiocyanate (Dex-FITC) 3 kDa (Sigma Aldrich) at the constant concentration of 0.25 mg/mL. The cell suspension was then injected into the microfluidic chip at the constant flow rate of 150 µL/min using a microfluidic pump (Harvard apparatus). Cells were collected at the outlet and allowed to recover for 5 minutes post-treatment. Subsequently, the cell suspension was centrifuged at 1.5 g for 5 minutes, and the supernatant was carefully removed. The cell pellets were resuspended in 350 µL of PBS solutions containing the corresponding concentrations of $CaCl_2$ used to deliver Dex-FITC before the treatment. 150 µL of a trypan blue 0.4% w/v solution was added to the cell suspension to reach a final concentration of 0.1% w/v and quench the extracellular fluorescence of Dex-FITC. The delivery efficiency of Dex-FITC based on the concentration of $CaCl_2$ added to PBS was analyzed by Attune NxT flow cytometer (Thermo-Fischer Scientific, USA), and the percentage of fluorescent cells for each group was quantified (n=3). Corresponding

fluorescent images of the cell suspensions post-treatment for the different groups were taken using a fluorescent microscope (Zeiss). A similar procedure was followed to evaluate the optimal concentration of PBS (KCl, KH_2PO_4, NaCl, Na_2HPO_4-$7H_2O$, no calcium, no magnesium) necessary to maximize the delivery efficiency of Dex-FITC. The only difference was that hASCs were resuspended in PBS solutions at different concentrations ranging from 1X to 0.5X before being deformed through the microfluidic device. All the solutions of PBS tested contained the same concentration of Dex-FITC (0.25 mg/mL).

3.2.5 Evaluation of the delivery efficiency of Dex-FITC at different molecular weights (3 and 70 kDa)

Prior to each experiment, the channels of the microfluidic devices were coated with 3% bovine serum albumin (BSA) for 15 minutes to increase the hydrophilicity of the surface of the PDMS microchannels. Each device was flushed with phosphate buffered saline (PBS) to wash any residue of BSA. Human adipose-derived stem cells (hASCs) from female donors between the age of 31 and 45 years old were purchased from Rooster Bio. Passages 2-5 were used for all the experiments. Prior to the experiments, cells were cultured in traditional 2D conditions (3.3×10^3 cells/cm^2) using hASCs High-performance media (Rooster Bio media) at 37°C and 5% CO_2 containing 2% of FBS. Additional studies were performed using NIH 3T3 fibroblasts, which were cultured in DMEM (Gibco) at 37°C and 5% CO_2 containing 10% of FBS.

Both cell lines were suspended in PBS 1X (0.4×10^6 cells/mL) with no calcium and containing dextran fluorescein-isothiocyanate (Dex-FITC) (Sigma Aldrich) at the concentration of 0.25 mg/mL. Two different molecular weights of Dex-FITC (3kDa and 70 kDa) were tested to evaluate the efficiency of delivery. The cell suspension was infused through the microfluidic device by a

PHD ULTRA™ Syringe Pump (Harvard Apparatus, Holliston, MA) at a controlled flow rate. Two different flow rates (150 and 300 µL/min) were tested in all the internalization studies. Cells were collected at the outlet and kept for 5 minutes at room temperature. hASCs were then centrifuged at the speed of 1.5 g for 5 minutes, and the Dex-FITC solution was discarded. The pellet was resuspended in 0.35 mL of PBS 1X containing propidium iodide (PI) (Life Technologies) for 15 minutes at room temperature. Finally, 150 µL of a trypan blue 0.4% w/v solution was added to the cell suspension to reach a final concentration of 0.1% w/v and quench the extracellular fluorescence of Dex-FITC. The efficiency of the delivery of Dex-FITC was evaluated by monitoring the percentage of positive fluorescent cells. The results were reported as the mean ± deviation standard (n=3).

3.2.6 Plasmid DNA delivery

The microfluidic devices designed in this study were also tested for the delivery of large plasmid DNA encoded for the green fluorescent protein (GFP). The DNA plasmid used for this study had about 4,000 bp and a corresponding molecular weight of 2,600 kDa. A few changes were made to guarantee the successful internalization of the plasmid compared to the delivery process described in section 3.2.5. hASCs were introduced in the microfluidic chip at the cell density of 2.6×10^6/mL in OptiMEM medium containing 100-300 µg/mL [179]. After deformation and internalization of the plasmid, the cell suspension was allowed to recover for 15 minutes at room temperature. Cells were seeded in 12 well plates and allowed to grow for 24 hours. Fluorescent images were taken to visualize the successful transfection with GFP with EVOS Auto Fl microscope. Additionally, cells were trypsinized and analyzed using flow cytometry to quantify the mean fluorescent intensity (MFI) of hASCs expressing GFP. The results were expressed as mean ± deviation standard (n=3).

3.2.7 Assessment of apoptosis and qPCR analysis

hASCs were stained for the presence of Annexin A5, which is used to detect apoptotic cells, which express phosphatidylserine on their cell membrane. Before the experiment, hASCs were passed through the microfluidic device at different flow rates. Cells were collected and seeded in a 24 well-plate for 24 hours. As a control group, hASCs were not squeezed through the microfluidic device and cultured in Rooster Bio media containing 10% of FBS for 24 hours.

hASCs were then collected by trypsinization and washed twice with cold PBS. The Annexin A5 binding buffer was used to resuspend hASCs in a final cell density of 1×10^6 cells/ mL. 10 µL of Annexin A5-FITC was added to the resuspended hASCs. Cells were then incubated in the dark for 30 minutes. Additionally, 1 µL of propidium iodide was added to the cells to stain necrotic cells. The apoptosis ratio of hASCs was immediately measured using the Attune NxT flow cytometer (Thermo-Fischer Scientific, USA). Aside from Annexin A5 staining, qPCR analysis of key apoptotic genes was carried out. Gene expression of *BAX*, *BAD*, *BAK*, *BBC3* was monitored right after the deformation through the microfluidic chips and after 24 hours. hASCs that did not undergo a step of deformation were used as a control group. mRNA was extracted from the cells using RNeasy Mini Kit (Qiagen, Germany) and quantified using a NanoDrop spectrophotometer (Thermo Scientific, USA). Next, mRNA samples were converted to cDNA using the High-Capacity cDNA Conversion Kit (Applied Biosystems, USA). Finally, the gene expression was obtained by using pre-designed primers and the KiCqStart SYBR Green Master Mix (Sigma Aldrich, USA). All reactions were performed using a Mastercycler RealPlex (Eppendorf, Germany). The fold expression levels were calculated using the relative ΔΔCt method (n=4). *GAPDH* was used as the housekeeping gene, and results were normalized based on the gene expression of the control group [223].

Following the same procedure, qPCR analysis was performed to evaluate possible changes in the expression of stemness-related genes including *Nanog, SOX2, KLF4* at 0 and 24 hours post-deformation using the microfluidic device. Similarly, we have investigated changes in the expression of cytoskeletal genes such as *ACTA1, MYH2*, *LAMA1,* and *KRT18* involved in the process of cytoskeletal remodeling after membrane resealing.

3.2.8 Investigation of cytoskeletal remodeling process after membrane rupture

For this test, two different groups were investigated. The test group consisted of hASCs exposed to Cytochalasin D at a concentration of 0.5 µM for two hours [224, 225]. The drug was solubilized in dimethyl sulphoxide. The control group consisted of hASCs cultured in normal conditions without any drug treatment. Cells from both groups were trypsinized and passed through the double deformation device at the flow rate of 300 µL/min and a gap of 8 µm between the constrictions. The suspension medium was supplemented with Dex-FITC 3 kDa at the constant concentration of 0.25 mg/mL for both groups. Subsequently, the cells were treated following the procedure reported in section 2.5, and fluorescent hASCs were detected using flow cytometry. Cells were exposed to trypan blue at the concentration of 0.1% w/v to quench the external fluorescence of Dex-FITC. The percentage of fluorescent cells were expressed as the mean ± deviation standard (n=3).

3.2.9 Statistical analysis

Statistical analysis was performed using an unpaired t-test and one-way ANOVA (followed by Tukey's multiple comparison test) to determine whether a significant difference exists between specific groups. All statistical analyses were carried out with GraphPad Prism Software 6. A p-

value less than 0.05 indicates statistical significance, which was displayed as *p < 0.05, **p < 0.01, ***p < 0.001.

3.3 Results and discussion

3.3.1 Fabrication and characterization of the microfluidic device

The formation of small transient pores in the cell membrane can be achieved by creating micron-sized constrictions with a size of half the diameter of the cell [179, 226]. Additionally, the arrangement of the micron-sized channels within the microfluidic device plays a fundamental role in modulating the extent of deformation the cells are subjected to during the squeezing phase [227]. Finally, cells need to be homogeneously distributed in the microfluidic channels to avoid the possible risk of clogging, thus enhancing the efficiency of internalization of extracellular cargos. Based on these concepts, we have developed a novel microfluidic design which includes different alternated sub-units defined as dispersion and squeezing zones (**Figure 3.1A**). Each microfluidic chip has 7 dispersion zones and 12 squeezing zones. The dispersion zone contains pillars made of polydimethylsiloxane (PDMS) with a diameter of 20 µm and a height of 15 µm, which are separated from one another with a 30 µm gap to ensure the proper dispersion of the cell suspension within the different channels of the squeezing zones. The inclusion of a dispersion zone prior to the squeezing channels was found to be efficient in preventing the formation of cell agglomerates, as demonstrated in another study [228]. The squeezing zone is fabricated with parallel channels to ensure a steady flow rate throughout the microfluidic device. This strategy guarantees the preservation of the flow in all the other channels if one of them is clogged by the cell suspension. We confirmed the presence of a steady flow by simulating the velocity of the flow in each channel using COMSOL (**Figure S3.1**). The squeezing zones were designed following two different

patterns. The first one was created by orienting the constrictions to form tunnels of 20 μm in length (25 in each squeezing zone), while the second design was obtained by changing the geometry and displacing the pillars to avoid the formation of micro-tunnels (50 in each squeezing zone). This orientation enabled the formation of squeezing constrictions rather than micro-tunnels. Scanning electron microscopy (SEM) images of the two different types of squeezing zones were taken to verify the correct disposition and dimensions of the channels (**Figure 3.1B-C**). The different geometry designs were able to deform the cell in two distinct modalities defined as "single" and "double" deformations within each squeezing path (20 μm) of the device (**Figure 3.1D**). The single deformation through single channels has already been investigated in other studies [226, 229]. In this case, cells are stretched along the direction of the flow leading to the formation of transient pores for exogenous cargo internalization. However, in the novel double deformation design, as investigated here, it is possible to change the membrane orientation and increase the number of deformations the cell can experience in each squeezing path. Our hypothesis is that the cells, while undergoing a double deformation, will internalize a larger amount of extracellular material compared to the single squeezing strategy. Nevertheless, this is not the only parameter that needs to be considered to maximize intracellular delivery.

For instance, the ion concentration is another factor that has been shown to affect the internalization efficiency of exogenous material and to control the process of membrane resealing after rupture [174, 230]. Specifically, there are two distinct plasma membrane repair mechanisms. If the pore size generated by squeezing is a few nanometers, cells spontaneously will repair their membrane after the injury by following a thermodynamic rearrangement of the phospholipid bilayer [231-233]. On the contrary, resealing of membrane ruptures larger than 200 nm in size requires the influx of calcium ions (Ca^{2+}) [234, 235]. Mechanical disruption of the cell membrane

by using microfluidic devices has been reported to promote the formation of pores with a size greater than 200 nm in other studies [175, 179]. Therefore, it was important to evaluate whether the delivery efficiency of extracellular cargo Dex-FITC could be affected by the amount of Ca^{2+} as well as other ions present in the delivery medium.

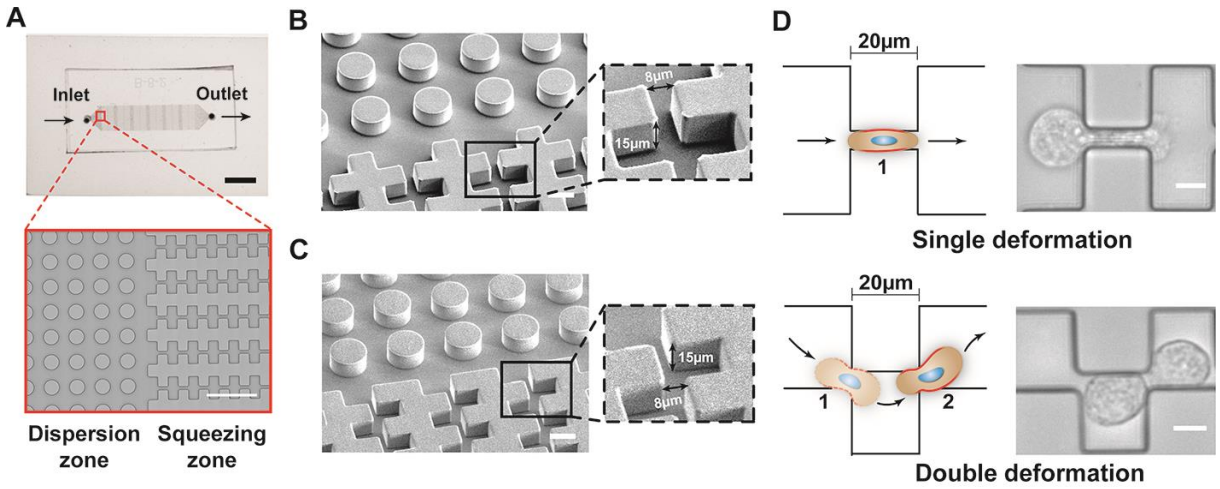

Figure 3.1 Design of microfluidic devices to induce cell deformation. A) Picture showing the overall microfluidic device structure composed of 7 dispersion zones and 12 squeezing zones (Scale bar = 5 mm). The inset shows a corresponding higher magnification image of the microfluidic device (Scale bar = 100 µm). B) and C) Corresponding SEM images of the two designs (Scale bars = 20 µm). On the right, insets of both patterns displaying the dimensions of the channels and the gap size. D) Schematic represeinting the process of cell squeezing with two different deformation modalities (single and double), and corresponding bright field images of hASCs squeezed through the single and the double deformation designs (Scale bar = 10 µm). Single deformation is a 1-step deformation process, whereas double deformation contains 2-step deformation of plasma membrane.

3.3.2 Effect of calcium and phosphate buffer concentration on the internalization efficiency

Upon the cell membrane injury, the influx of Ca^{2+} enables the fusion of intracellular vesicles responsible for the formation of a membrane patch necessary to reseal the bilayer (**Figure 3.2A**) [236]. Based on this mechanism, we tested different Ca^{2+} amounts (0, 1 and 2 mM) in the medium phosphate buffered saline (PBS 1X) to determine the concentration necessary for optimal Dex-

FITC 3 kDa delivery in hASCs (**Figure 3.2B**). These concentrations were selected considering the physiological range of Ca^{2+} in the extracellular fluids [237, 238]. We observed the highest delivery efficiency in the group without any calcium, and a corresponding decrease in the percentage of fluorescent cells as the amount of calcium was increased up to 2 mM (physiological Ca^{2+} concentration) (**Figure 3.2C**). These results suggest that the influx of Ca^{2+} after membrane rupture may be directly linked to the time required for the complete resealing of the membrane [239]. On the contrary, in the absence of Ca^{2+}, the membrane pores remain open for a longer time, and therefore, there is a higher chance for internalization of extracellular cargos. These results are in accordance with other reports investigating the role of calcium in the delivery of Dex-FITC in HeLa cells similarly deformed using a different type of microfluidic device [175]. Aside from Ca^{2+} concentration, cellular membrane deformability can be altered by changing the osmolarity of the buffer used for the treatment [240]. To prove this concept, we studied the delivery of the same cargo into hASCs by varying the concentration of PBS from 1 X to 0.25 X. No significant difference was observed in the delivery efficiency of Dex-FITC 3 kDa when the concentration of PBS was varied from 1 X to 0.5 X. However, at 0.25 X PBS the delivery efficiency was much higher leading to a 90% of efficiency (**Figure 3.2D**). This result may be due to the greater deformation of the membrane in less concentrated salt solutions resulting in the generation of more membrane pores. However, a corresponding increase in cell death was observed by flow cytometry analysis as the concentration of PBS was decreased (**Figure 3.2E**). These findings are consistent with another report investigating the role of PBS in intracellular delivery of fluorescent cargos using cancer cells [174]. Overall, the absence of calcium and a concentration of PBS equal to 1X were the optimal conditions to maximize the delivery efficiency of the model Dex-FITC, and these set of parameters were used for the rest of the study.

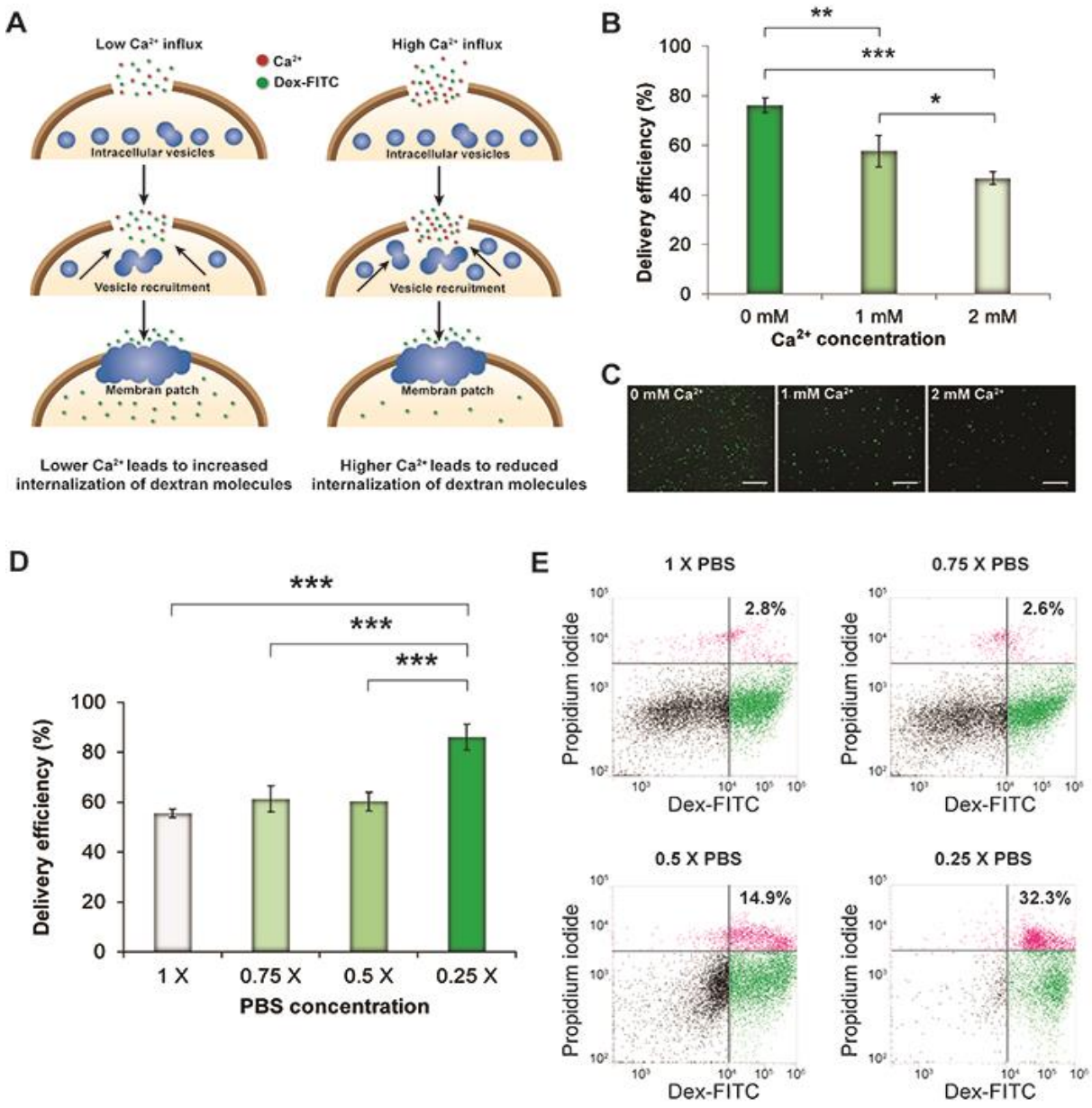

Figure 3.2 Effect of varied ionic concentrations of calcium and PBS on intracellular delivery of Dex-FITC in hASCs. A) Schematic showing the process of membrane resealing in the presence of calcium. The influx of calcium is responsible for the fusion of intracellular vesicles. These vesicles form a membrane patch to reseal the membrane rupture. B) Delivery efficiency of Dex-FITC 3kDa in hASCs using PBS 1X with different concentrations of Ca^{2+}. C) Corresponding fluorescent images of hASCs loaded with Dex-FITC in the different group tested post-treatment (Scale bar = 200 µm). D) Delivery efficiency of Dex-FITC 3kDa in hASCs using different concentrations of PBS to evaluate the effect of osmolarity on intracellular diffusion. E) Dot plots graphs displaying the population of green fluorescent hASCs that have internalized Dex-FITC, and red fluorescent hASCs stained with propidium iodide (dead cells). The percentage of dead cells is reported for all the different group tested. Results are reported as mean ± deviation standard (n =3). * = $p < 0.05$, ** = $p < 0.01$, and *** = $p < 0.001$.

3.3.3 Optimization of the microfluidic parameters for efficient intracellular delivery

As the second step of this work, we have investigated the effect of gap size, flow rate, design type, and molecular weight of the cargo as additional features influencing intracellular delivery. Each microfluidic device was able to successfully treat a cell density of 400,000 cells/mL. A set of gaps between the micron-sized constrictions for both designs was developed ranging from 6 to 10 µm which corresponded to half of the diameter of hASCs (~ 17.5 µm). Two different flow rates (150 µL/min and 300 µL/min) were tested to verify the impact of the flow velocity on the internalization efficiency. Flow rates larger than 300 µL/min were not tested because the designed microfluidic chips could not withstand them. Two distinct molecular weights of Dex-FITC (3 kDa and 70 kDa) were tested to verify whether the designed microfluidic devices were suitable for the internalization of small molecules such as siRNA, miRNA, and oligonucleotides, as well as large biomolecules including proteins and enzymes [226]. Finally, as the last parameter, we compared the efficiency of the two modalities of squeezing as discussed previously.

Dex-FITC was selected due to its impermeability through the cell membrane, and only a small percentage of cells were able to internalize Dex-FITC 3 kDa and 70 kDa via endocytosis (**Figure S3.2**). The cell suspension containing Dex-FITC was squeezed through the device and allowed to recover post-treatment for 5-10 minutes at room temperature. This time has been found to be necessary for the resealing of the cell membrane, as demonstrated in another similar study [226]. A significant increase in the delivery of Dex-FITC 3 kDa was observed when hASCs were squeezed through the narrower gaps in both designs (**Figure 3.3A**-**B**). However, once a double deformation was applied, a higher internalization was observed. Specifically, a delivery efficiency larger than 80% was achieved in this design when using a gap of 8 µm and a flow rate set to 300 µL/min. In contrast, a decrease to 60% was detected when using the same parameters in the single

deformation design (**Figure 3.3C**). Similar trends were observed in the delivery efficiency between the two designs while keeping the other parameters constant (**Table S3.1**). These data confirm the validity of our hypothesis. It is likely that the cells may experience greater localized stress due to the change in membrane orientation when passing through the double deformation design compared to the single deformation group. This difference may be responsible for a larger number of transient holes in the cell membrane leading to higher diffusion in the cytosol of the external molecules as detected by flow cytometry analysis. In other studies, by modifying the deformation angles of the constrictions, it was possible to change the orientation of the cell membrane during the squeezing phase [174]. This variation led to a larger deformation and higher diffusion of exogeneous material into the cytosol similar to our findings.

The efficiency of internalization in all the tested groups decreased when Dex-FITC 70 kDa was delivered. This result indicates that the size of the cargo is an important parameter that can affect the delivery efficiency irrespective of the design of the microfluidic device used. Furthermore, a significant decrease in the percentage of fluorescent cells was observed with an increase in gap size, confirming the data obtained with Dex-FITC 3 kDa. However, with a larger molecule, it is more evident the effect of the flow rate on the percentage of delivery for both designs tested (**Figure 3.3D-E**). Finally, the double deformation design exhibited a larger internalization of Dex-FITC 70 kDa compared to the single deformation group as observed previously. Precisely, an increase in positive fluorescent cells from 38% to 53% was detected using flow cytometry when comparing the two designs with the same gap of 6 µm and the same flow rate of 300 µl/min (**Figure 3.3F**).

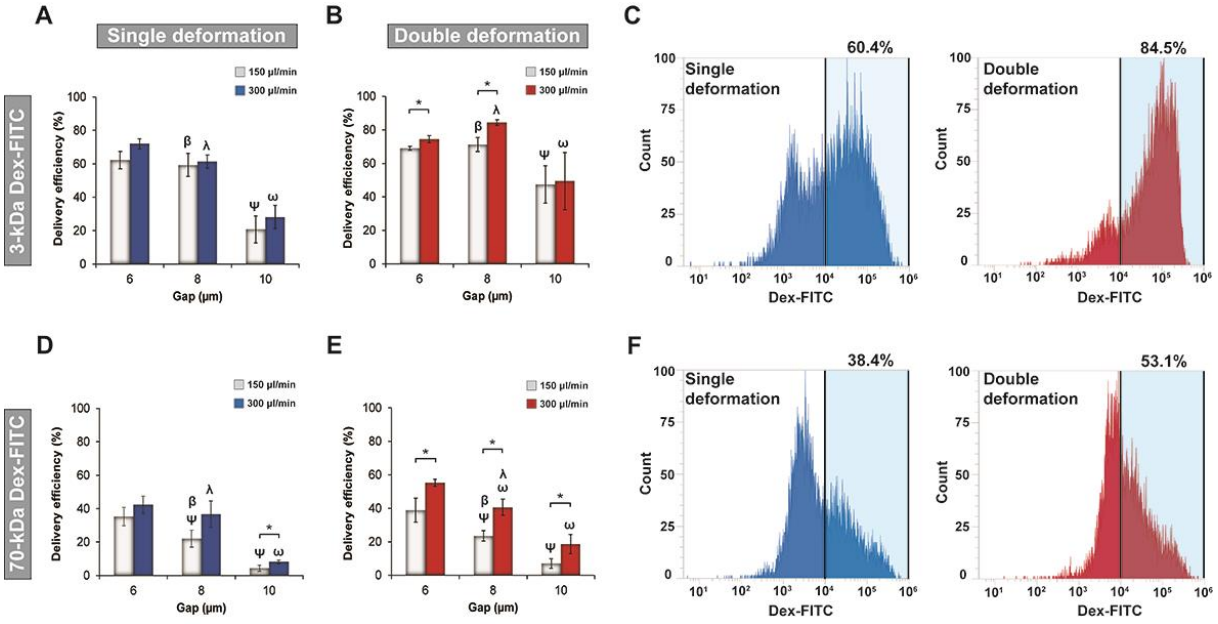

Figure 3.3 Effect of gap size, flow rates and geometry (single and double deformation) on the internalization of Dex-FITC with different molecular weight in hASCs. A) and B) Delivery efficiency of Dex-FITC (3 kDa) in hASCs using single and double deformation, respectively. Three different gaps (6, 8 and 10 µm) and two different flow rates (150 µL/min and 300 µL/min) were tested for each design C) Representative histogram plots displaying a higher percentage of green fluorescent cells in the group undergoing double deformation. hASCs were squeezed using the same gap (8 µm) and flow rate (300 µL/min) for both designs. D) and E) Delivery efficiency of Dex-FITC (70 kDa) using single and double deformation, respectively. A decrease in the percentage of positive fluorescent hASCs were found in all the gaps tested compared to the results reported for Dex-FITC 3 kDa. F) Representative histogram plots obtained by flow cytometry showing a higher percentage of delivery of Dex-FITC 70 kDa in the double deformation group compared to the single deformation design. hASCs were squeezed using the same gap (6 µm) and flow rate (300 µL/min) for both designs. Results are reported as mean ± deviation standard (n =3). ψ and ω are used to indicate significant change in delivery compared to gap 6 for the other two gaps at the flow rate of 150 µL/min and 300 µL/min, respectively ($p<0.05$). β and λ are used to indicate significant change in delivery compared to gap 8 for gap 10 at the flow rate of 150 µL/min and 300 µL/min, respectively ($p<0.05$). * indicates significance between two different flows for the same gap ($p<0.05$).

A similar trend in the delivery efficiency was observed for the other gaps and flow rates for the double deformation design (**Table S3.2**). We also performed internalization studies using NIH 3T3 fibroblasts, and a significant decrease in the percentage of Dex-FITC was observed when

using a higher molecular weight. (**Figure S3.3**). Collectively, these data confirmed our hypothesis that cells can experience a more impactful squeezing in the double deformation design, and the process of internalization was more efficient when smaller gaps and higher flow rates were used. We also explored the possibility to deliver biomolecules larger than Dex-FITC 70 kDa. Specifically, GFP plasmid was delivered successfully using the double deformation design, although the efficiency of transfection was low (less than 10%). The mean fluorescent intensity (MFI) of transfected hASCs was similar in both groups at the different flow rates tested (150 and 300 µL/min) (**Figure S3.4**). Poor transfection efficiency may be due to several factors. One of the primary reasons is the possible plasmid degradation occurring in lysosomes compartments, which prevents its successful translocation to the nucleus. Additionally, another possible explanation is that the plasmid used in this study had a large molecular weight (~2,600 kDa) and was not linearized as reported in a different study [228].

3.3.4 Evaluation of cell viability and apoptosis

The next step of our investigation was to verify the impact of cell deformation on cell viability. Specifically, it was essential to assess whether a double deformation would have any detrimental effect compared to the less efficient single deformation design. Cell viability was studied 30 minutes post-treatment by propidium iodide staining. In both designs, there was an increase in cell viability as the gap size increased (**Figure 3.4A-B**). This trend was expected based on the extent of deformation induced by the constriction gap size. Specifically, the highest cell viability value was associated with a 10 µm gap, which is slightly higher than half of the hASCs' diameter. No significant change was observed as the flow rate increased from low (150 µL/min) to high (300 µL/min) except for the double deformation design using a gap of 8 µm. Flow cytometry analysis

displayed comparable results in the percentage of positively stained dead cells with propidium iodide when comparing the two different designs at the same gap (10 μm) and flow rate (300 μL/min) (**Figure 3.4C**). Similar results in the percentage of cell viability were found for both designs when comparing all the other parameters (**Table S3.3**). We also observed a similar trend in the cell viability for fibroblasts tested with the two different microfluidic devices (**Figure S3.5**). Overall, considering the efficiency of delivery as well as the cell viability trends, so far described, the double deformation design with a gap of 8 μm represented the best option to promote efficient delivery without causing a significant change in cell viability. Therefore, to investigate possible changes in apoptosis and gene expression of cytoskeletal markers, further characterization was performed by using this optimized device. We analyzed the effect of the flow rate on the apoptosis of hASCs after 24 hours post-treatment using Annexin A5 staining. Annexin A5 is used to detect apoptotic cells that express phosphatidylserine on their surfaces. The results of the different groups tested were compared to a control group consisting of hASCs cultured in normal conditions without being passed through the microfluidic device. Flow cytometry analysis showed an increase in the percentage of apoptotic cells as the flow rate was increased. In detail, an increase from 8% to 13% of apoptotic cells was observed, although not statistically significant (**Figure 3.4D**). Similarly, we investigated the gene expression of pro-apoptotic markers such as *BAD*, *BAX*, *BAK1*, and *BBC3* immediately after squeezing and at 24 hours post-treatment (**Figure 3.4E-F**) [223]. Compared to the control groups, no significant change in the expression profile was observed at both time points. Moreover, to demonstrate the lack of changes in stem cell genotype, we performed qPCR analysis on the expression of common stemness cell genes including *Nanog*, *Sox2*, *Klf4* after 24 hours post-treatment [241]. No significant change in the profile expression compared to the control group was observed after 24 hours post-treatment (**Figure S3.6**). Overall,

these combined results demonstrate the safety of the optimized designed microfluidic device, which did not alter cell functionality after the deformation of the cell membrane.

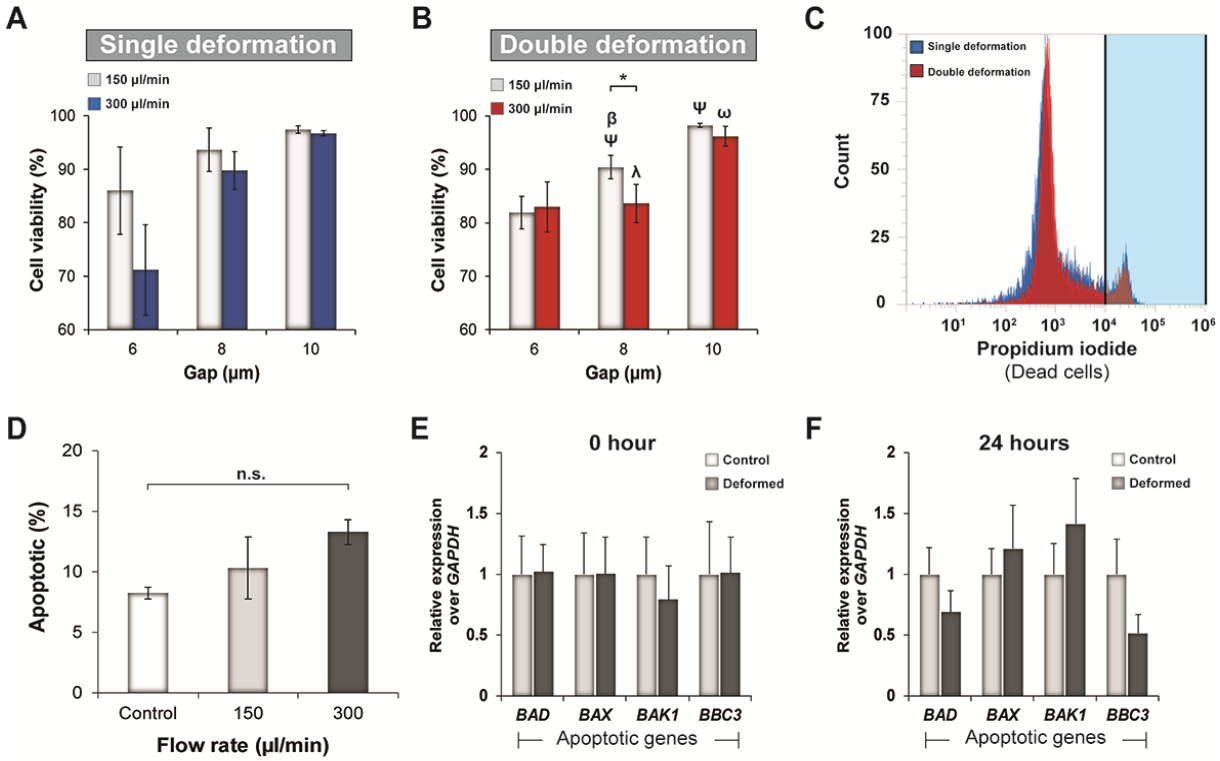

Figure 3.4 Effect of gap size, flow rates and geometry design on viability and apoptosis of hASCs passing through the microfluidic device. A) and B) Percentage of cell viability obtained after passing the cells through the single and the double deformation design, respectively. Similar to the delivery efficiency tests, three different gaps (6,8 and 10 µm), and two different flow rates (150 µL/min and 300 µL/min) were tested for each design. Results are reported as mean ± deviation standard (n =3). ψ and ω are used to indicate significant increase in cell viability compared to gap 6 for the other two gaps at flow rate of 150 µL/min and 300 µL/min, respectively ($p<0.05$). β and λ are used to indicate significant increase in cell viability compared to gap 8 for gap 10 at the flow rate of 150 µL/min and 300 µL/min, respectively ($p<0.05$). * indicates significance between two different flows for the same gap ($p<0.05$). C) Overlap between histogram plots obtained by flow cytometry displaying a similar population of dead hASCs stained with propidium iodide for both designs. D) Percentage of apoptotic hASCs 24 hours post-treatment after passing through the double deformation design at different flow rates. The percentage of apoptotic cells was determined by staining hASCs with Annexin V staining followed by flow cytometry analysis. E) and F) qPCR analysis of key genes involved in the process of apoptosis such as *BAD*, *BAX*, *BAK1* and *BBC3* after 0 and 24 hours post-treatment, respectively. hASCs cultured in a well plate without undergoing a process of deformation were used as control group. No significant change was observed among the two groups for both time points. Results are reported as mean ± deviation standard (n=3). n.s. indicates non-significant.

3.3.5 Evaluation of the key parameters involved in cell membrane resealing

Finally, it was essential to understand the role of cytoskeletal rearrangement and cell stiffness in the process of membrane repair and cargo internalization in hASCs. Particularly, upon damage of the cell membrane calcium enters the cytosol and initiates a cascade of events leading to the resealing of the membrane. These include a step of depolymerization of actin fibers followed by intracellular vesicle fusion to form a patch necessary to reseal the membrane. Finally, remodeling of cytoskeletal components takes place to replace the membrane patch and to form the cortical cytoskeleton [234]. Based on these well-known events, it was important to study the regulation of several markers involved in the expression of cytoskeletal proteins immediately after membrane rupture. We observed a significant upregulation of actin (*ACTA1*) 3.79 ± 0.7, myosin II (*MYH2*) 2.24 ± 0.46, for hASCs undergoing a process of squeezing. These changes compared to the control group were not present after 6 hours, indicating an active process of cytoskeletal remodeling occurring only shortly after the rupture (**Figure 3.5A-B**).

To further confirm the role of actin as the main regulator involved in membrane resealing, we induced the depolymerization of actin filaments in the cytoskeletal network prior to the process of squeezing. The overall hypothesis is that the stiffness of the cell may be an additional factor responsible for the membrane deformability. Precisely, a disruption in the actin cytoskeletal network could be responsible for the formation of a larger number of pores during squeezing, leading to a higher internalization of extracellular cargo (**Figure 3.5C**). To test this hypothesis, we exposed the cells to the drug Cytochalasin D (Cyto D) for two hours, which inhibits the polymerization of actin in hASCs, This mycotoxin is known to penetrate cells and link to actin leading to its disruption. After internalization, Cyto D has also been reported to promote a reduction in hASCs stiffness from 3 kPa to 1.5 kPa [242]. hASCs treated with CytoD displayed a

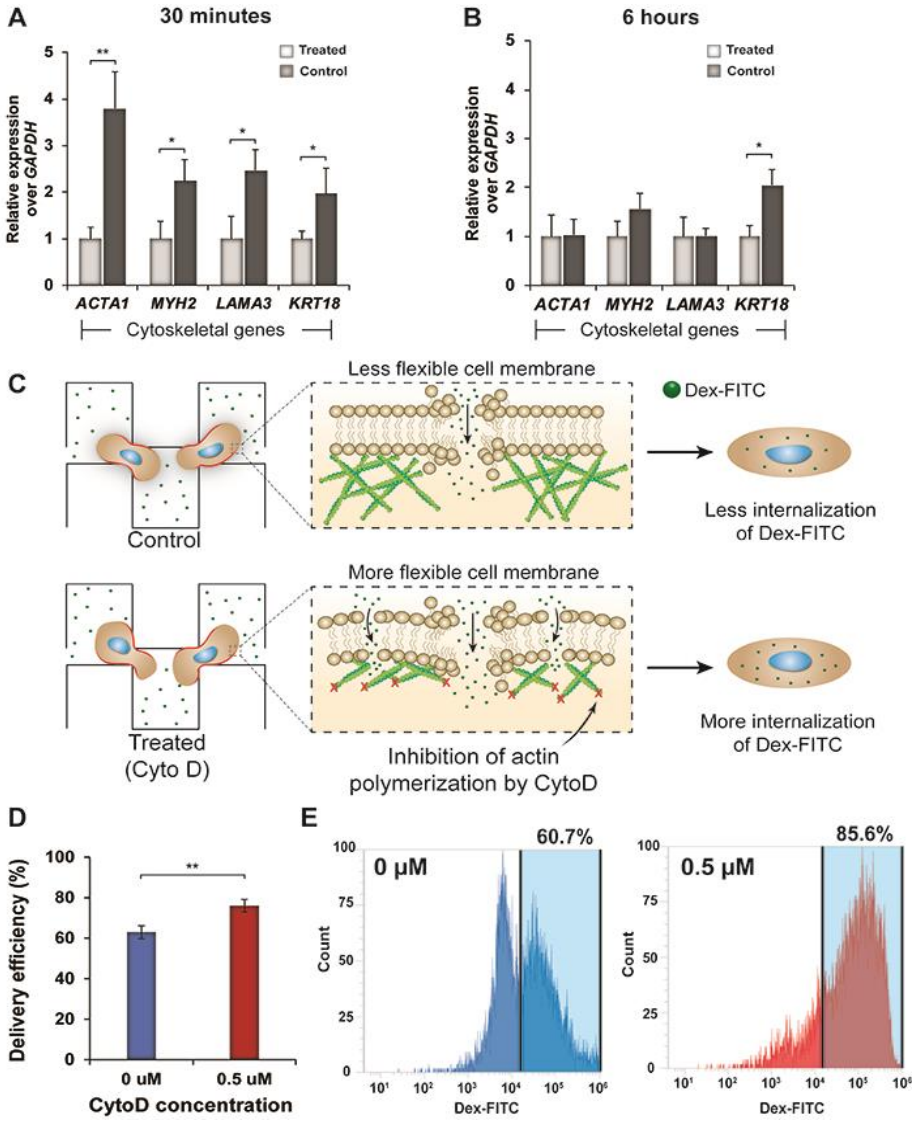

Figure 3.5 Assessment of key parameters involved in the process of membrane resealing. A) and B) qPCR analysis of the expression of different cytoskeletal genes in hASCs after 30 minutes and 6 hours post-treatment, respectively. A significant upregulation in the genes was observed after 30 minutes indicating an active process of cytoskeletal remodeling. As a control group, hASCs were cultured without undergoing a step of deformation. C) Schematic indicating the process of cell squeezing with and without the presence of Cytochalasin D (Cyto D), which inhibits actin polymerization and disrupts network organization. The hypothesis is that the inhibition of actin polymerization will reduce the stiffness of hASCs leading to a higher deformability of the membrane and enhanced molecule internalization ability. D) Delivery efficiency of Dex-FITC 3kDa in hASCs treated with 0.5 µM Cyto D for 2 hours compared to untreated cells. A higher internalization of Dex-FITC was detected in the treated cells. Results are reported as mean ± deviation standard (n=3). ** indicates significance between the two different groups tested ($p < 0.01$). E) Corresponding histogram plots displaying positive Dex-FITC cells treated with 0 µM and 1 µM of CytoD.

higher internalization of Dex-FITC after squeezing through the optimized microfluidic device. Precisely, an increase in positive fluorescent cells from 60% up to 85% was observed by flow cytometry (**Figure 3.5D-E**). These findings confirmed our hypothesis highlighting the importance of cell stiffness and actin network formation as additional parameters to be considered for efficient internalization of extracellular cargo.

3.4 Conclusions

In this work, we have successfully developed and optimized a novel microfluidic device to maximize the delivery efficiency of external model fluorescent molecules into hASCs. This method is fast and can be used to treat large numbers of cells (0.5×10^6) in a short amount of time (< 5 minutes). The process of delivery of Dex-FITC into hASCs was directly influenced by the concentration of calcium ions in the medium. Increasing the concentration of calcium led to a decrease in delivery efficiency, suggesting the presence of a calcium-dependent mechanism. Such an effect indicates the formation of pores of around 200 nm, as demonstrated by other studies [175]. The osmolarity of the solution did not influence the internalization efficiency of Dex-FITC, and an increase was detected only for the lower concentration (0.25X). However, at such a low amount of PBS, a significant decrease in cell viability was observed.

Aside from the medium composition, the design of the chip had a profound impact on delivery efficiency. A double deformation of the cell membrane in each squeezing path of 20 μm enabled a higher internalization of Dex-FITC compared to the single deformation modality. The internalization efficiency decreased as the size of the cargo increased, although the optimized device could be used to deliver different types of molecules, including plasmid DNA. Overall, based on the results, the designed microfluidic chip is ideal for delivering small bioactive

molecules with a size below or equal to 3 kDa that can be useful to enhance the therapeutic potential of hASCs in future studies. High cell viability was observed irrespective of the squeezing modality proving that the double deformation design can be effectively used without inducing cell death. 8 µm gap size between the micro-constrictions was found to be the best compromise in terms of high delivery efficiency and minimal cell death. More importantly, the process of squeezing did not induce any apoptosis and did not significantly upregulate key pro-apoptotic genes. Similarly, the stemness of hASCs was preserved 24 hours post-treatment suggesting a complete restoration of their functionality. However, additional investigations should be carried out in the future to verify whether hASCs can maintain their osteogenic or adipogenic differentiation potential.

Finally, we have analyzed the role of actin stress fibers and stem cell stiffness as additional parameters influencing the internalization of extracellular cargo. Our results indicate that hASCs undergo a process of cytoskeletal remodeling after the formation of transient pores in the cell membrane. However, this process is only occurring within the first-hour post-treatment. In fact, the cells were able to restore the expression of these markers to their basal level after 6 hours. Finally, inhibiting actin polymerization in hASCs by using Cyto D was responsible for the formation of a more flexible cell membrane. The change in cell stiffness led to a higher internalization of Dex-FITC. These findings further confirm the role of actin as a key component involved in the process of cell membrane resealing, which needs to be accurately considered for further studies aimed to maximize the delivery efficiency of extracellular cargo. For instance, a thorough characterization based on the stem cell stiffness could be useful to predict which cell type would be the most suitable when using this developed novel microfluidic device.

CHAPTER 4. Direct intracellular delivery of trehalose into human adipose-derived stem cells for efficient cryopreservation

Abstract

Available strategies to preserve stem cells rely on cryopreservation, and one of the most commonly used cryoprotectant agent (CPA) is dimethyl sulfoxide (DMSO). This CPA has been shown to preserve stem cells during a freezing/thawing process, although its high toxicity at 37 °C can hinder the regenerative potential of stem cells upon transplantation *in vivo*. A valid alternative to DMSO is trehalose, a natural disaccharide that does not pose any risk of cytotoxicity to stem cells during freezing/thawing. However, trehalose needs to be delivered intracellularly to be effective as a CPA in comparison to the cell-permeable DMSO. This issue is caused by the limited permeability of this sugar in the cell membrane that hampers its use for cryopreservation purposes. In this work, we proposed the intracellular delivery of trehalose through the creation of transient pores by using the designed microfluidic chip discussed in Chapter 3. The goal of this work is to promote the intracellular delivery of trehalose into human adipose-derived stem cells (hASCs) to promote efficient cryopreservation. To verify the effectiveness of our strategy, the amount of trehalose delivered intracellularly was quantified and optimized based on the observed cell viability post-cryopreservation. hASCs were also frozen in freezing media containing DMSO and used as a standard control group. Several parameters including cell viability, apoptosis, retention of stemness, angiogenic growth factor secretion, and differentiation capability through osteogenic and adipogenic lineages, were compared with cells frozen in DMSO.

Modaresi S., Pacelli S., Chakravarti R.A., Paul A., Direct intracellular delivery of trehalose into human adipose-derived stem cells for efficient cryopreservation. 2019 (To be submitted)

4.1 Introduction

Stem cells are a valuable resource for tissue engineering, regenerative medicine, and stem cell-based therapies [243-248]. Precisely, the global stem cells market size is expected to reach 11,380 billion dollars by 2021 [249]. Currently, stem cells are being tested as a valid treatment in a variety of diseases such as leukemia, myocardial infarction, diabetes, autoimmune, and blood disorders [243, 250-252]. Hence, due to their immense value in regenerative medicine, it is important to provide a safe method of cell storage post-harvesting which can preserve their stemness and prevent any sort of metabolic damage. In addition, stem cell banking reduces the costs associated with culturing cells at 37°C and limit the possibility of genetic alteration due to continuous long-term culture *in vitro* [253-256].

Stem cells can be cryopreserved by using different CPA [257-260]. The most common CPA is DMSO, a small amphiphilic molecule, which rapidly penetrates the cell membrane and protects cells from irreversible damage during a freezing/thawing process [261, 262]. Despite its efficiency, DMSO has been shown to be toxic to cells at 37 °C (body temperature) and requires rigorous washing steps for the complete removal from the cells. This drawback limits the availability of freshly thawed cells cryopreserved with DMSO for clinical use [263-265]. Additionally, during each washing step, about 10% of cells can be lost, making this procedure highly inefficient [241]. Finally, DMSO has also been found to induce differentiation in more than 25 human stem cells lines [266], and incomplete removal of DMSO has been shown to cause intravascular hemolysis, increased serum transaminase levels, cardiac and pulmonary arrest, acute renal failure, and seizures [267-269]. As a safer alternative, disaccharides, such as trehalose, can be considered as natural CPAs for cryopreservation [262, 270-273]. They offer the advantage of being non-toxic

and do not need to be removed after thawing. However, one of the drawbacks associated with this type of CPA is the limited permeability across cell membranes [274, 275].

Over the past few decades, various approaches have been developed to overcome this issue and promote the delivery of trehalose into eukaryotic mammalian cells. The most direct method for the controlled delivery of trehalose is microinjection [276-278]. Although useful, this process is extremely labor-intensive and cannot be used for all types of cells [139, 271]. Another strategy is to introduce trehalose through transporter 1 (TRET 1), which facilitates the selective transport of trehalose across the cell membrane [279]. Additionally, endogenous expression of trehalose in cells can be achieved by adenoviral transduction [280]. These methods are associated with several concerns, including possible cytotoxic effects and the risk of undesired genetic modification [130, 281]. For these reasons, viral transduction is not considered a safe option with limited applicability in a clinical setting.

Other research groups have investigated alternative strategies for the delivery of trehalose. These consist of the synthesis of delivery vehicles such as nanoparticles [241, 272], polymers [282-284], cell-penetrating peptides [285], and liposomes [258, 286]. Several limitations are associated with these types of carriers, including possible cytotoxic effects, poor stability, as well as poor loading efficiency. The listed drawbacks restrict the possible use of these approaches for large-scale stem cell banking.

Additional routes for the delivery of trehalose are based on permeabilization methods that require thermal, ultrasound, and electrical (electroporation) forms of energies [167, 287-289]. These methods, although effective in enhancing the internalization of trehalose, require thorough optimization as they can induce irreversible damage to cells.

An alternative solution is to explore techniques aimed to generate transient membrane pores by mechanical deformation of the cell membrane. These temporary defects allow the internalization of trehalose with high efficiency and limited cytotoxic effects. For example, microfluidic devices can be fabricated with micron-sized microfluidic constrictions of around half to one-third of the cell's diameter to generate localized stress on the cell membrane [170-172]. By following this approach, the goal of the work discussed in Chapter 4 is to quantify the intracellular delivery of trehalose using the optimized microfluidic described in Chapter 3 with the aim to promote efficient cryopreservation of human adipose-derived stem cells (hASCs). Specifically, hASCs loaded with trehalose will be cryopreserved in freezing media supplemented with extracellular trehalose and several parameters including cell viability, apoptosis, stemness, angiogenic growth factor secretion, and differentiation capability will be tested post-cryopreservation. hASCs frozen in freezing media containing DMSO will be used as a control group for all the studies proposed in this work. Overall, the findings of this research will be necessary to validate the efficacy of this approach for the intracellular delivery of trehalose to promote efficient cryopreservation.

4.2 Materials and Method

4.2.1 Materials

D-(+)-Trehalose dihydrate from Saccharomyces cerevisiae, phosphate buffer saline 1X (PBS), potassium phosphate monobasic (KH_2PO_4), potassium phosphate dibasic (K_2HPO_4), Magnesium -chloride ($MgCl_2$), dimethyl sulfoxide (DMSO), ascorbic acid-2 phosphate, β-glycerophosphate, dexamethasone, and hematoxylin were purchased from Sigma Aldrich. α-Minimum Essential Medium (α-MEM), Dulbecco's Modified Eagle Medium (DMEM), fetal bovine serum (FBS) propidium iodide (PI), 10% goat serum, Mouse anti-human Paxillin antibody, goat anti-mouse AlexaFluor 594 antibody, diamidino-2-phenylindole dilactate (DAPI), phalloidin-AlexaFluor488, Matrigel Matrix, Gentamicin were purchase from Thermo Fisher Scientific. Trehalose fluorescein isothiocyanate (Trehalose-FITC) Mw 731.7 Da was purchased from Kerafast.

4.2.2 Delivery of trehalose into hASCs using microfluidic chips

The same procedures reported in sections 3.1 and 3.2 of Chapter 3 were used to fabricate the silicon master molds necessary to manufacture the polydimethylsiloxane (PDMS) microfluidic chips. Specifically, microfluidic devices displaying a double deformation design with gaps of 8 μm in the deformation zones were selected for this investigation based on the optimization studies carried out in Chapter 3.

hASCs (passages 2-5) were used for all the studies. Cells were cultured in T-75 flasks and collected by trypsinization when reaching 70-80% of confluency. After the neutralization and removal of trypsin, the cell pellet was resuspended in α-MEM and subdivided into aliquots containing 0.5 $\times 10^6$ cells. hASCs were centrifuged at a speed of 1.5×10^3 g for 5 minutes. The media was

discarded, and the pellet was resuspended in 0.5 mL of low-conductive phosphate buffer (10 mM K_2HPO_4, 10 mM KH_2PO_4 and 1 mM $MgCl_2$) containing different concentrations of trehalose (100, 200, 250, and 300 mM). Cell diameter was measured with an automated cell counter to evaluate the effect of the osmotic pressure of the delivery medium. Three measurements were carried out for each cell suspension. The microfluidic chip was washed and pre-treated with the different trehalose solutions before the infusion of the cells. The cell suspension was then injected into the microfluidic chip at the constant flow rate of 150 µL/min using a microfluidic pump (Harvard Apparatus, MA, USA). hASCs were collected at the outlet and allowed to recover for 5 minutes post-treatment at room temperature. Subsequently, the cell suspension was centrifuged at 1.5×10^3 g for 5 minutes, and the supernatant containing trehalose was carefully removed and stored for further quantification as reported in the following section. Cells were then resuspended in 0.5 mL of PBS 1X containing propidium iodide for 15 minutes at room temperature. The cell suspension was analyzed by flow cytometry to evaluate the percentage of cell death.

4.2.3 Quantification and visualization of intracellular trehalose

The amount of trehalose internalized by the cells was evaluated indirectly by measuring the concentration of trehalose before and after hASCs were squeezed in the microfluidic device. Precisely, trehalose was quantified by using a Megazyme trehalose assay (Megazyme International Ireland, Wicklow, Ireland) according to the instructions provided in the manufacturer's protocol. Trehalose is first enzymatically converted into glucose by hydrolysis. Glucose is then phosphorylated into glucose-6-phosphate (G6P) by a hexokinase. Finally, G6P is converted into gluconate-6-phosphate by the enzyme glucose-6-phosphate dehydrogenase (G6P-DH) with the formation of reduced nicotinamide-adenine dinucleotide phosphate (NADPH) which can be

detected by UV spectroscopy at 340 nm using a well plate reader. The results were calculated as the mean ± deviation standard (n=3).

Finally, to visualize the presence of intracellular trehalose, the same experiment was carried out by delivering trehalose-FITC. Briefly, hASCs were suspended in a solution of trehalose-FITC at the concentration of 0.125 mg/mL in PBS 1X. Cells were infused in the microfluidic chip and collected at the outlet. After squeezing, hASCs were left for 5 minutes at room temperature in the presence of trehalose-FITC to allow the resealing of the membrane. hASCs were then centrifuged at the speed of 1.5×10^3 g for 5 minutes, and the trehalose-FITC solution was discarded. The pellet was resuspended in 0.35 mL of PBS 1X containing propidium iodide for 15 minutes at room temperature. Finally, 150 µL of a trypan blue 0.4% w/v solution was added to the cell suspension to quench the extracellular fluorescence of trehalose-FITC. The efficiency of the delivery of trehalose-FITC was evaluated by monitoring the percentage of fluorescent cells. The results were reported as the mean ± deviation standard (n=3). Similarly, hASCs loaded with trehalose-FITC were imaged using a fluorescent microscope (Evos Fl Auto, Life Sciences, USA), and corresponding bright-field images were taken to visualize the population of fluorescent cells.

4.2.4 Cryopreservation of hASCs using trehalose

hASCs 0.5×10^6 were loaded with trehalose (300 mM) by following the procedure reported in section 4.2.2. Cells were collected at the outlet of the microfluidic chip and allowed to reseal their membrane for 5 minutes at room temperature. Then, hASCs were centrifuged at 1.5×10^3 g for 5 minutes, and the supernatant discarded. The pellet was resuspended in freezing media containing trehalose as the cryoprotectant agent to obtain a cell suspension of 1×10^6 cells/mL. The freezing media was made of DMEM, 10% FBS and trehalose included at different concentrations ranging

from 50mM to 600 mM. Cells were frozen at -80 °C for 24 hours using a 'Mr. Frosty' freezing container filled with isopropanol to allow the temperature to decrease constantly at the rate of 1 °C/min. Subsequently, hASCs were stored in the liquid nitrogen for 24 hours. Additionally, hASCs were passed through the microfluid device without loading any trehalose intracellularly and frozen in the same freezing media containing trehalose. Finally, as a control group, hASCs cultured in flasks were collected by trypsinization and frozen at the cell density of 1×10^6/mL using DMEM, supplemented with 10% FBS and 10% DMSO. The cells were frozen following the same steps consisting of a slow freezing phase (1°C/min) at -80 °C for 24 hours, followed by a freezing step in liquid nitrogen.

4.2.5 Assessment of cell viability, morphology, proliferation rate, and apoptosis post-cryopreservation

The following studies were carried out using hASCs frozen in DMSO (control group) and hASCs loaded with trehalose (300 mM) and frozen the freezing media supplemented with trehalose (400 mM). The cryovials were removed from the liquid nitrogen tank and placed in a 37 °C beads bath for five minutes. The freezing media was diluted with an equal volume of fresh culture medium added to the cell suspension before centrifugation. The cells were resuspended in a PBS solution pH 7.4 supplemented with 1μL of a PI solution (100 μg/mL) for 15 minutes to assess cell viability. The percentage of dead cells post-thawing was quantified with flow cytometry analysis by measuring the amount of red fluorescent cells. Three different samples were assessed for each tested group.

hASCs obtained from the two different groups were thawed and seeded at the cell density of 1×10^4 cells/well in a 24 well-plate with flat and clear bottom. Cells were allowed to proliferate for 24

hours before staining to visualize their morphology. Cells were fixed with 4% paraformaldehyde for 5 minutes at 37 °C and permeabilized with 0.1% Triton-X100 for 10 minutes at room temperature. Samples were blocked with 5% normal goat serum at room temperature for 45 minutes. Mouse anti-human Paxillin antibody (1:400 with 1% goat serum) was added to hASCs and left overnight at 4 °C. Goat anti-mouse AlexaFluor 594 (1:500 in 1% goat serum) was then added and left for one hour at room temperature. DAPI and phalloidin-AlexaFluor488 were used to counterstain nuclei and F-actin, respectively. Fluorescent images were taken for each sample with a fluorescent microscope (Evos Fl Auto) at 40 X. Images were processed using ImageJ software, which enabled the quantitation of the total area of adhesion sites.

Furthermore, the proliferation rate of hASCs was monitored for 24 and 48 hours post-thawing using an MTS assay (Promega, USA). hASCs were seeded in 24 well plates at the cell density of 25×10^3 cells/well. Cells were incubated with an MTS reagent (20 µL for every 100 µL of media) following the manufacturer's instructions. The absorbance of the media supplemented with the reagent was monitored at 490 nm after 1 hour and 30 minutes of incubation at 37°C in the dark. Proliferation rate was calculated considering an average of 3 different samples for each group and normalizing the results to the number of cells quantified 24 hours post-thawing. A calibration curve ranging from 5×10^3 to 1×10^5 cells/well was created to accurately correlate the absorbance values with the number of cells.

Finally, the population of apoptotic cells was determined by Annexin A5 staining and subsequently assessed by flow cytometry. Briefly, cells were thawed and seed in 12 well plates at the cell density of 1×10^5 cells/well. Cells were allowed to proliferate for 24 hours prior to the experiment. Briefly, hASCs were collected by trypsinization and resuspended in PBS at the cell density of 1×10^6 cells/mL. Cells were stained with Annexin A5 following the instructions provided in the

manufacturer's protocol and analyzed by flow cytometry. The results were reported as the mean ± standard deviation of three samples for each group.

4.2.6 Analysis of stemness and pro-apoptotic genes post-cryopreservation

The expression of key stemness markers was monitored by qPCR analysis to investigate whether the stemness of hASCs was preserved after being stored in freezing media supplemented with trehalose. Similarly, the expression of pro-apoptotic markers was investigated post-cryopreservation. Briefly, cells were seeded in a 12-well plate for 48 hours after thawing. Three groups were tested including hASCs frozen in DMSO, hASCs loaded with trehalose and frozen in media containing the disaccharide. mRNA was extracted from the cells using an RNeasy Mini Kit (Qiagen) and quantified using a NanoDrop spectrophotometer. Next, the mRNA samples were converted to cDNA using the High-Capacity cDNA Conversion Kit. Finally, gene expression was measured using a mixture of predesigned primers and the KiCqStart SYBR Green Master Mix. The expression of the following stemness markers was assessed, including *Klf4*, *Nanog*, and *Sox2*. Similarly, the following pro-apoptotic genes such as *BAD, BAX, BAK1, BBC3* were analyzed. All the reactions were performed using a Mastercycler RealPlex. The fold expression levels will be calculated using the relative ΔΔCt method (n=4). *GAPDH* was considered as the housekeeping gene, and results were normalized based on the gene expression of hASCs cryopreserved in freezing media supplemented DMSO.

4.2.7 Quantification and assessment of angiogenic growth factor activity by hASCs *in vitro* post-cryopreservation

hASCs from the different groups were thawed and cultured in Rooster Bio medium containing 2% FBS at 37 °C and 5% CO_2 for 24 hours and 48 hours. Cells were seeded in 24 well plates at the cell density of 5×10^4 cells/well. The conditioned media was collected, and the concentration of vascular endothelial growth factor (VEGF) was quantified using an ELISA kit (R&D Systems) (n=3) by following the manufacturer's protocol. A calibration plot in the range from 33 pg/mL to 1ng/mL was used to correlate the absorbance at 450 nm with the concentration of VEGF.

Additionally, the conditioned media obtained from the different groups was tested for its efficacy in promoting the formation of tubular-like structures *in vitro*. Human umbilical vein endothelial cells (HUVECs) were seeded on a growth factor depleted Matrigel based on the manufacturer's protocol. Briefly, 289 µL of growth factor depleted Matrigel Matrix (10 mg/mL), previously thawed overnight on ice, was added to a 24 well culture plate. The plate was then incubated at 37°C for 60 minutes to allow the gel to form. HUVECs (1.2×10^5) were seeded on each gel. The media composition was varied according to the different groups. A negative control consisted of endothelial cell growth medium-2 bullet kit (EGM-2, Lonza) without VEGF and basic fibroblast growth factor (bFGF). As positive control cells were cultured on the Matrigel with Lonza Media EG2-bullet kit supplemented with all the angiogenic growth factors. As test groups, HUVECs were cultured in EGM-2 without angiogenic growth factor but supplemented with the condition containing VEGF at the concentration of 0.1 ng/mL. After 18 hours, bright field images of the endothelial networks were taken for each group and the total number of nodes, meshes, and segments, as well as the total segment length and the number of isolated segments were determined

using the Angiogenesis Analyzer for ImageJ. Results were obtained from the analysis of at least 15 images for each group.

4.2.8 Evaluation of the differentiation ability of hASCs post-cryopreservation

These studies were carried out to compare the differentiation potential post-cryopreservation *in vitro* of hASCs frozen in media containing DMSO or trehalose. After thawing, hASCs were seeded at the cell density of 2.5×10^4 cells/well in DMEM supplemented with 10% fetal bovine serum (FBS) and 1% penicillin and streptomycin. When the cells reached 80% of confluency, the media was replaced with complete adipogenesis differentiation medium (1X StemPro® Adipocyte Differentiation Basal Medium, 1X StemPro® Adipocyte Supplement, and Gentamicin (10 mg/mL) reagent. The media was changed every other day for a total number of 10 days. As a negative control group, hASCs were cultured in DMEM 10% FBS and 1% penicillin-streptomycin for the entire duration of the study. On the last day of differentiation, the media was removed, and cells were washed with PBS. Cells were fixed with 4% paraformaldehyde for 5 minutes and washed with PBS. Subsequently, cells were treated with isopropanol 60% for 5 minutes. The presence of intracellular lipid droplets, which is indicative of adipogenic differentiation, was assessed by Oil Red O (Sigma Aldrich) staining. The Oil red Stock Solution was obtained by dissolving 60 mg of Oil Red O in 20 ml of 100% isopropanol. The suspension was mixed and allowed to sit for 20 min. Then, the Oil Red O stock solution was diluted in distilled water by mixing 3 parts of this solution with 2 parts of water. After 10 minutes, the suspension was filtered with a 0.22 μm syringe filter and used within 15 minutes. 400 μL of Oil Red O solution was added to each well for 20 minutes. Cells were imaged using a microscope with a color camera to visualize the stained lipid droplets.

Additionally, gene expressions of several markers involved in early adipogenesis phase were monitored by qPCR analysis following the same procedure reported in section 4.2.6. These genes include peroxisome proliferator-activated receptor gamma-2 (*PPARγ-2*), lipoprotein lipase (*LPL*), adipocyte protein 2 (*aP2*), and *GAPDH* as the housekeeping gene.

Osteogenic differentiation was also investigated. After thawing, hASCs were initially cultured as reported above, and the media was replaced with an osteogenic medium consisting of α-MEM, 10% FBS, 1% penicillin-streptomycin, 50 μM ascorbic acid-2 phosphate, 10 mM β-glycerophosphate, and 10 nM dexamethasone. The media was changed every other day for 14 days. Alkaline phosphatase (ALP) enzymatic activity was measured at day 7 following a fluorometric assay (Abcam, USA). To measure the ALP activity, cells were centrifuged at 1,500 rpm for 5 minutes, and the supernatant was removed. Cells were homogenized in ALP buffer following the steps described in the protocol provided by the kit. Fluorescence was measured using a microplate reader at the excitation of 360 nm and an emission wavelength of 440 nm (n=3).

At day 14, the media was removed, and the cells were washed with PBS. The cells were fixed with 4% paraformaldehyde for 5 minutes. After fixation, hASCs were washed twice with distilled water and were stained for intracellular calcium deposits with 2% Alizarin Red S solution for 2-3 minutes. After washing the excess of staining the cells were imaged with a microscope equipped with a color camera.

4.2.9 Statistical analysis

Statistical analysis was carried out by performing a two-way analysis of variance (ANOVA) followed by Tukey's multiple comparison test, which was used to determine the presence of significant difference among the groups. A t-test was used to compare experiments between two

experimental groups. All statistical analyses were carried out with Graph-pad Prism Software 7. A p value less than 0.05 indicates statistical significance, which was displayed as *$p < 0.05$, **$p < 0.01$, ***$p < 0.001$.

4.3 Results and discussion

4.3.1 Intracellular delivery of trehalose using the microfluidic device

To be effective as a cryoprotectant reagent, trehalose needs to be present both intracellularly and extracellularly as demonstrated in other studies [274, 290]. Trehalose contributes to the formation of a stable glassy state by establishing hydrogen bonds with the polar head functional groups of phospholipids and transmembrane proteins present in the plasma membrane [291]. This phenomenon can prevent damage to the cells during the freezing step and avoid adverse conformational changes in proteins. Based on this premisis, the first part of this study was focused on the optimization of the concentration of trehalose both extracellularly and intracellularly with the final objective to find an alternative to DMSO for stem cell banking.

Trehalose is a disaccharide of glucose, and due to its hydrophilicity, it cannot diffuse through the cell membrane. To overcome this issue, we have investigated a novel and safe delivery method that should promote efficient internalization without eliciting any detrimental effect on cell functionality. Toward this goal, hASCs were forced to pass through micro-constrictions in a microfluidic chip that could generate transient pores in the cell membrane, as shown in the schematic (**Figure 4.1A**). These temporary defects in the cell membrane enable the passive diffusion of trehalose present in the delivery medium. Specifically, a squeezing gap of 8 μm, a flow rate of 150 μL/min, and a double deformation design were selected as the constant parameters of the microfluidic device in this study. These values were selected based on the best delivery

results obtained in Chapter 3. Additionally, we further proved in this work that the optimized microfluidic chip did not cause any significant cytotoxic or apoptotic effect. To prove this point, we investigated the cell proliferation rate and apoptosis of hASCs after being squeezed in the microfluidic device (passed), and the results were compared to cells without any treatment (not passed). A small increase in the cell apoptosis values from 7.4±1.4 % to 11.2 ± 1.4 % was observed as the cells were squeezed in the microfluidic device (**Figure S4.1A**). However, cells displayed a similar proliferation rate after 48 hours of culture for both groups suggesting that the process of squeezing did not hinder the cells proliferation potential of hASCs (**Figure S4.1B**).

The amount of extracellular trehalose in the freezing media (DMEM containing 10% FBS) was optimized based on hASCs' cell viability. Specifically, the concentration of trehalose was varied from 50 to 600 mM to determine the optimal amount of extracellular trehalose needed for effective cryopreservation. According to the results, the highest cellular viability was detected when trehalose was present in the freezing medium at a concentration of 400 mM (**Figure 4.1B**). Concentration higher than 400 mM were not selected as a decline in cell viability was observed probably due to the increase in osmotic pressure. This osmotic effect was verified indirectly by measuring the variation in cell diameter of hASCs once resuspended in the freezing media containing trehalose prior to freezing. A decrease from 16.9 ± 0.2 μm to 14.02 ± 0.3 μm was measured as the cells were exposed to freezing media supplemented with 50 mM and 600 mM trehalose, respectively (**Figure S4.2A**).

As the second step, we delivered trehalose intracellularly by varying its concentration from 100 mM to 300 mM using a low conductive phosphate buffer (~50 mOsm/kg) [289]. The amount of trehalose delivered intracellularly was quantified indirectly by measuring the decrease in its concentration before and after squeezing the cells through the microfluidic device. As expected,

the amount of disaccharide delivered intracellularly was strictly dependent on the initial concentration used. The highest amount of trehalose delivered to the cells was 42.8 ± 5.76 mM, which was achieved by delivering trehalose at an initial concentration of 300 mM (**Figure 4.1C**). Aside from the concentration of trehalose, the cell diameter is another important parameter that can impact the process of squeezing and the corresponding internalization of the external cargo. The best delivery results are commonly achieved when cells are squeezed within a gap with a size equal to half of the value of their diameter [218]. The optimized microfluidic device used in this study possessed micro-constrictions with a gap size of 8±1 μm. This means that cells should display a diameter of 16 ± 1 μm to guarantee the maximum efficiency of delivery. The cell diameter was initially measured to assess any change induced by the different osmotic pressure of the trehalose solutions. Specifically, hypotonic (100 mM, ~150 mOsm/Kg and 200 mM ~250 mOsm/kg), isotonic (250 mM ~290-300 mOsm/kg) and hypertonic (300 mM, ~350 mOsm/Kg) solutions were tested in this study. A constant decrease in cell diameter was observed from 21.7 ± 0.5 μm to 15.1 ± 0.2 μm as the concentration of trehalose was increased, suggesting a change in osmotic pressure (**Figure S4.2B**). The low efficiency of internalization detected when using a solution of 100 mM of trehalose could be attributed to the largest cell diameter of hASCs in this delivery medium, which was equal to 21.7 ± 0.5 μm. This value is much higher than the optimal range of 16 ± 1 μm required to obtain a maximum delivery efficiency. On the contrary, the cell diameter was in the optimal range required for effective deformation using the designed microfluidic device for concentrations of trehalose equal to 250 and 300 mM.

4.3.2. Assessment of cell viability of hASCs loaded with trehalose

Subsequently, cells loaded with trehalose were frozen in the freezing medium containing a constant concentration of extracellular trehalose of 400 mM, which was chosen based on the previous optimization. Cell viability was assessed by flow cytometry analysis immediately after thawing in the media. Interestingly, the cell viability of hASCs after cryopreservation was significantly improved once trehalose was delivered intracellularly. Specifically, only 55.2% of hASCs were still alive after cryopreservation when no trehalose was internalized in the cytosol. As the concentration of trehalose delivered was increased from 100 mM to 300 mM, a significant enhancement was detected up to 83% of cell viability (**Figure 4.1D**). Similar results were obtained for the 250 and 300 mM groups, although the amount of trehalose internalized intracellularly was 32.97 ± 3.05 mM and 42.8 ± 5.76 mM, respectively (**Figure 4.1C**). hASCs cryopreserved using DMSO displayed the better results in terms of cell viability with a value of 92.5% although not statistically significant compared to 300 mM trehalose group (**Figure 4.1D**). Several studies have demonstrated that the required intracellular concentration of trehalose for effective cryopreservation of mammalian cells ranges from 100 to 200 mM [259, 292]. However, our results demonstrate that an intracellular concentration of 42.8 ± 5.76 mM was sufficient to provide effective cryoprotection of hASCs with similar results to the DMSO group. This difference observed in this study may be due to the type of cells investigated as well as the different method used for the delivery of trehalose.

Finally, we demonstrated the intracellular presence of the disaccharide by delivering trehalose-FITC into hASCs using the same strategy. hASCs became fluorescent upon delivery of trehalose-FITC. Corresponding bright-field and fluorescent images were taken to visualize the cells that successfully retained the external fluorescent cargo (**Figure 4.1E**).

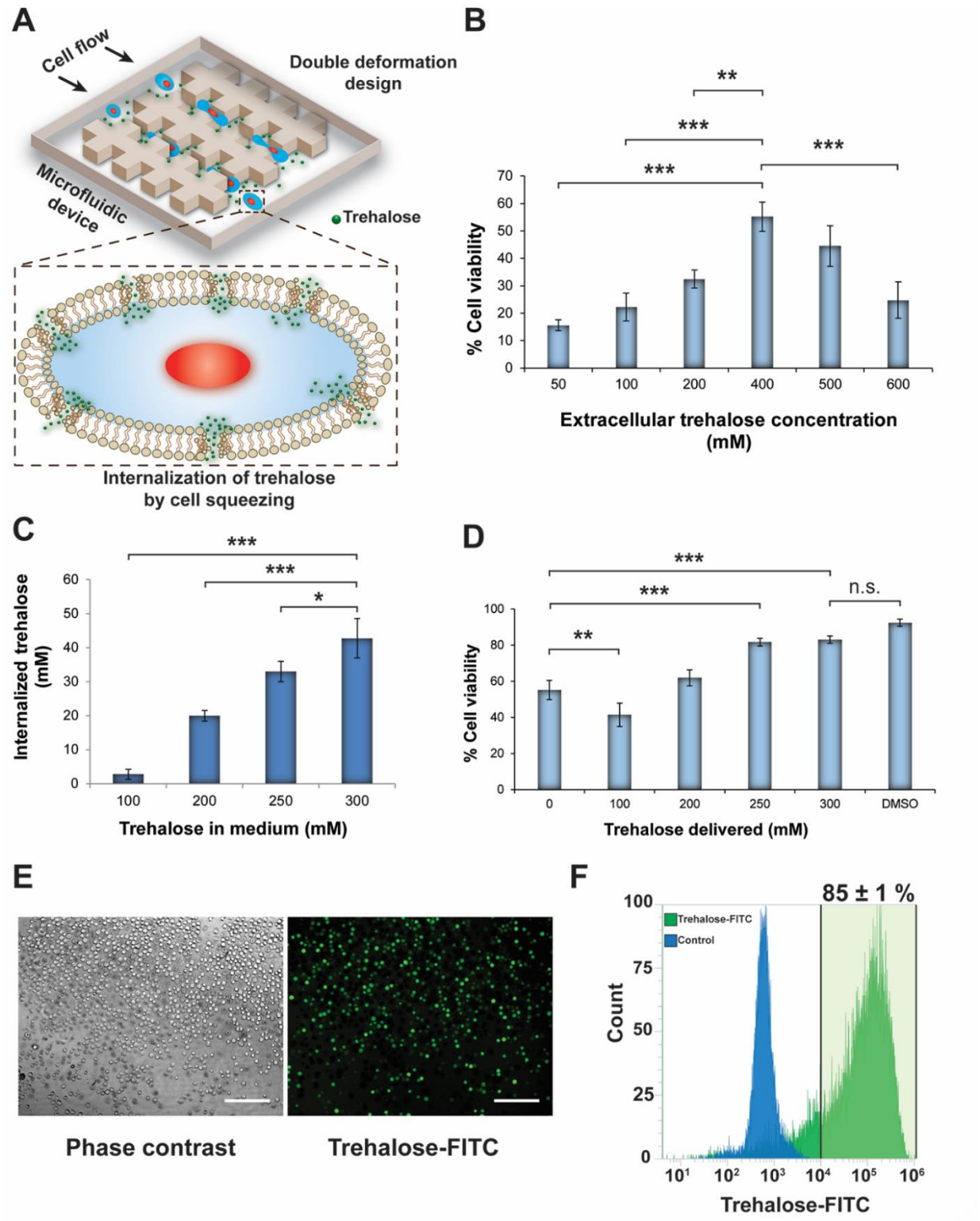

Figure 4.1 Internalization of trehalose and quantification of intracellular delivery. A) Schematic is representing the process of cell squeezing necessary for the formation of transient pores in the cell membrane. These pores enable the passive diffusion of extracellular trehalose into the cells. B) Cell viability of hASCs assessed by flow cytometry to identify the optimal concentration of extracellular trehalose in the freezing medium, C) Quantification of intracellular delivery of

trehalose in hASCs (n=3). D) Cell viability of hASCs assessed by flow cytometry after cryopreservation. The amount of extracellular trehalose used in all the groups was 400 mM except for DMSO. E) Bright-field and corresponding fluorescent images of hASCs after delivery of trehalose-FTIC. Scale bars = 200 μm. F) Flow cytometry histograms comparing hASCs loaded with trehalose-FITC and without any treatment. The gate indicates the population of fluorescent cells that have internalized the disaccharide. Results are reported as mean ± standard deviation (n=3). * = $p < 0.05$ ** = $p < 0.01$, *** $p < 0.001$, and n.s. indicates non-significant values.

Precisely, 85.1% of the cell population was fluorescent after being squeezed through the microfluidic device in the presence of trehalose-FITC (**Figure 4.1F**). Overall, these results indicate that our proposed strategy is efficient in promoting the delivery of trehalose. An extracellular concentration of 400 mM and intracellular of 42.8 ± 5.76 mM of trehalose were sufficient to preserve the viability of hASCs after cryopreservation with similar results to DMSO. This set of parameters were used for the rest of the studies discussed in the following sections.

4.3.3 Evaluation of morphology, proliferation rate, apoptosis, and stemness post-cryopreservation using trehalose

Aside from cell viability, it was important to evaluate other cellular parameters after cryopreservation with trehalose. hASCs' morphology was investigated after thawing the cells by immunofluorescence staining to visualize actin stress fibers and the expression of focal adhesion points. Specifically, we stained for the presence of paxillin, which is one of the main proteins present in the focal adhesion complexes of mammalian cells [293]. Cells cryopreserved in trehalose (400 mM extracellular, and 48.2 mM intracellularly) did not show any visible change in morphology compared to the cells cryopreserved in the freezing media containing 10% of DMSO (**Figure 4.2A**). Quantification of the total area of focal adhesions and cell area showed comparable results for both tested groups (**Figure 4.2B-C**). Similarly, the proliferation rate of the cells post-cryopreservation was monitored by MTS assays at 24 and 48 hours. Cells were able to proliferate

after 48 hours with an increase in their cell number of 2.3 ± 0.1 and 2.86 ± 0.6 times for the DMSO and trehalose group, respectively (**Figure 4.2D**). Furthermore, apoptotic cells were evaluated after 48 hours post-thawing by flow cytometry analysis. Specifically, cells were stained with Annexin A5, which is a protein that binds to phosphatidylserine. This phospholipid is normally present in the cytosol side of the plasma membrane in healthy cells. On the contrary, cells undergoing a process of apoptosis start to expose this phospholipid on the extracellular side of their membrane that can be detected by staining with Annexin A5 and quantified by flow cytometry. A similar percentage of apoptotic cells was found in both groups with a value of 5.4 ± 0.3% and 6.2 ± 0.6 % for trehalose and DMSO group, respectively (**Figure 4.2E**).

FACs results were further confirmed by evaluating the expression of pro-apoptotic genes after 24 hours post-thawing. Precisely, we investigated the expression of several markers such as *BAD*, *BAX*, *BAK1,* and *BBC3*, and the results were normalized based on the gene expression of hASCs frozen in DMSO. No significant difference was found in the expression of these markers for both groups investigated (**Figure 4.2F**). Finally, we evaluated the expression of key markers that regulate stem cells' stemness, including *Sox2*, *Nanog,* and *Klf4* after 24 hours post-thawing. Also, for this investigation, no significant difference in the expression of these genes was detected (**Figure 4.2G**). Taken all together, this set of data demonstrate how hASCs cryopreserved with trehalose delivered intracellularly displayed a similar cellular behavior after thawing to the ones cryopreserved in DMSO. However, it should be noticed that further investigation is required to verify whether similar results can be obtained for longer times of storage (one month) since the majority of these data were collected after only 24 hours post-cryopreservation in liquid nitrogen.

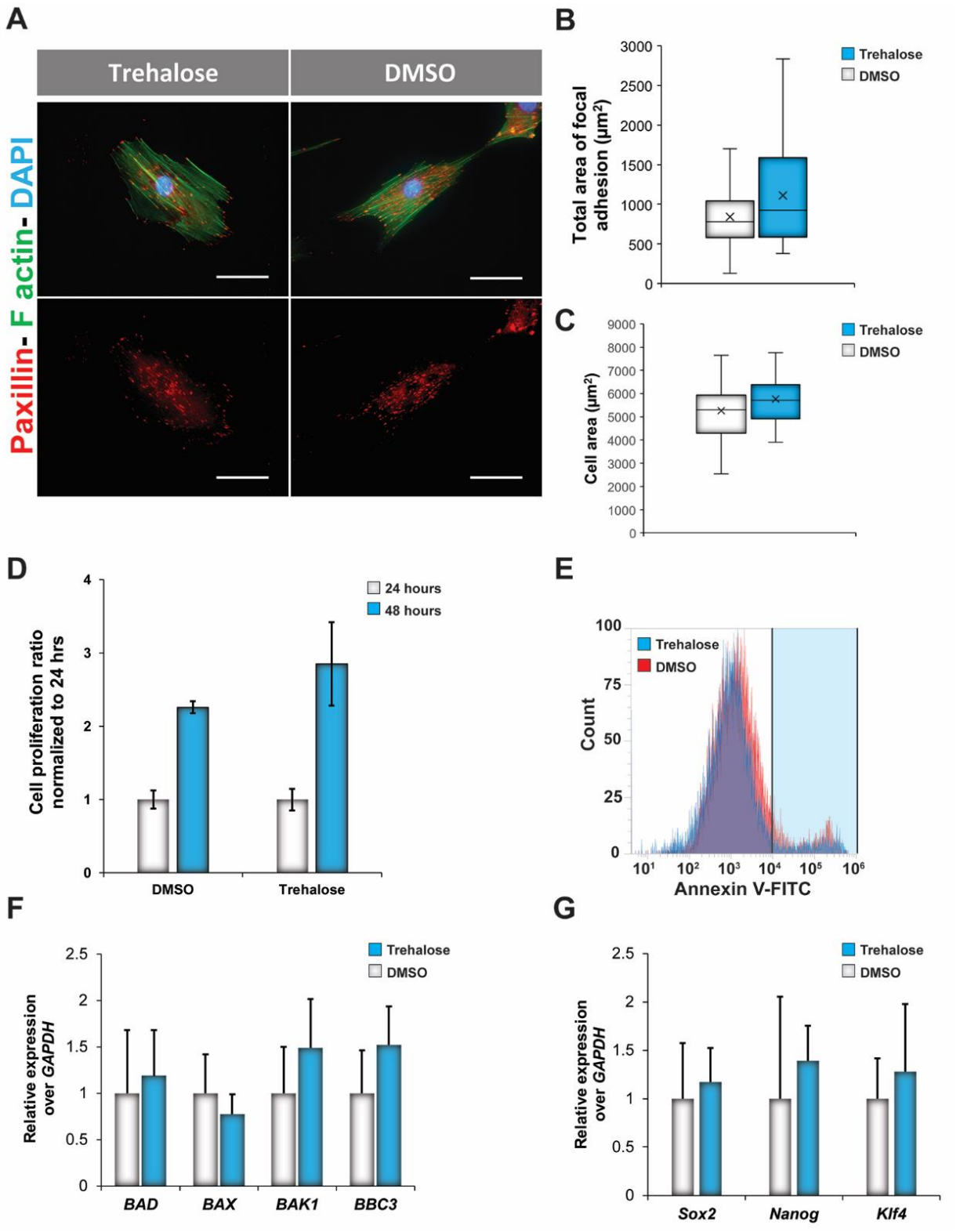

Figure 4.2 Evaluation of stem cell morphology, proliferation rate, apoptosis, and stemness after cryopreservation using trehalose vs. DMSO. A) Immunofluorescence staining of hASCs cryopreserved with freezing media supplemented with trehalose (400 mM) and DMSO (10% v/v).

hASCs were loaded with trehalose intracellularly before cryopreservation by delivering 300 mM trehalose. Cells were stained with Alexa Fluor 488 Phalloidin to visualize actin stress fibers (green) and with Diamidino-2-phenylindole dilactate (DAPI) to stain the nuclei (blue). In addition, paxillin staining (red) was carried out to identify the area of focal adhesions. Scale bar = 50 µm. B) Quantification of the total area of focal adhesions expressed by hASCs cryopreserved with the two different types of freezing media. Results are calculated based on the red fluorescence intensity obtained from the immunofluorescent staining for paxillin expression (n=20). C) Quantification of cell area of hASCs for the two groups tested. Results are reported as mean ± standard deviation (n=17). D) MTS analysis of the cell proliferation rate of the two different groups calculated at 48 hours post-thawing (n=3). Results were normalized based on the cell number obtained at 24 hours. E) The overlap between representative histogram plots obtained by flow cytometry displaying a similar population of apoptotic cells for both hASCs cryopreserved in freezing media containing DMSO and trehalose. The area in light blue defines the gate used to quantify the apoptotic cells stained with Annexin A5 (n=3). F) qPCR analysis of key genes involved in the process of apoptosis such as *BAD*, *BAX*, *BAK1*, and *BBC3* 24 hours post-cryopreservation for DMSO and trehalose. G) Relative expression of stemness genes (*Sox2*, *Nanog*, *Klf4*) over *GAPDH* (housekeeping gene) in hASCs after 24 hours post-cryopreservation. qPCR results are reported as mean ± standard deviation (n=3). * = $p < 0.05$ ** = $p < 0.01$, and *** $p < 0.001$ (n=3).

4.3.4 Evaluation of angiogenic growth factor secretion and pro-angiogenic potential post-cryopreservation using trehalose

One of the well-known features of hASCs is their ability to produce a milieu of angiogenic growth factors that are essential to regulate angiogenesis both *in vitro* and *in vivo* [294, 295]. Therefore, we verify whether hASCs' angiogenic potential was still retained after cryopreservation by quantifying the amount of VEGF secreted after cryopreservation. The results were expressed as a fold increase at 48 hours and normalized to the amount of growth factor retrieved after 24 hours. According to the results, a higher increase in VEGF secretion was detected in the DMSO group at 48 hours in comparison to hASCs frozen with trehalose (**Figure 4.3A**). As a control study, we also investigated whether the mechanical stress produced by the process of cell squeezing was able to influence VEGF secretion with respect to untreated hASCs. The fold increase of VEGF found in both groups tested at 48 hours was similar, indicating that the process of squeezing used to deliver trehalose did not alter the angiogenic potential of hASCs (**Figure S4.3**).

The angiogenic potential of the different secretome produced by hASCs was further investigated for their ability to modulate the reorganization of human umbilical vein endothelial cells (HUVECs) into tubular structures. Particularly, HUVECs were seeded on Matrigel hydrogels, and their network structure was monitored over the course of 18 hours. The medium used to culture HUVECs was supplemented with the secretome derived from the different groups of hASCs (trehalose vs. DMSO) cultured for 24 hours post-thawing. Bright-field images were taken to assess the morphology of HUVECs and verify the formation of a healthy ranched network. A positive and negative control were included in the study consisting of HUVECs cultured in Lonza medium with and without angiogenic growth factors, respectively. The morphology of the HUVECs' network did not display significant differences among the groups except for the negative control where a poor connection and lack of interconnected segments was clearly evident after 18 hours (**Figure 4.3B**).

A more detailed analysis was carried out by ImageJ to quantify several parameters such as the number of nodes, number of meshes, number of segments, the total segment length and the number of isolated segments (**Figures 4.3C-G**). Each one of these parameters is essential to define the connectivity of the network and the presence of tubular structures (meshes), which are indicative of a healthy vasculature network. On the contrary, the number of isolated segments should be as low as possible as it suggests the lack of connection among the branches of the network. As expected, the negative control displayed the lower values among all groups for all the parameters quantified except for the total number of isolated segments. No significant difference was detected between the trehalose and the DMSO groups except for the total segment length, which was found to be significantly higher in the DMSO group. Overall, these set of results suggest indirectly that

the angiogenic secretome derived from hASCs cryopreserved with trehalose has a similar angiogenic potential with respect to hASCs cryopreserved in DMSO.

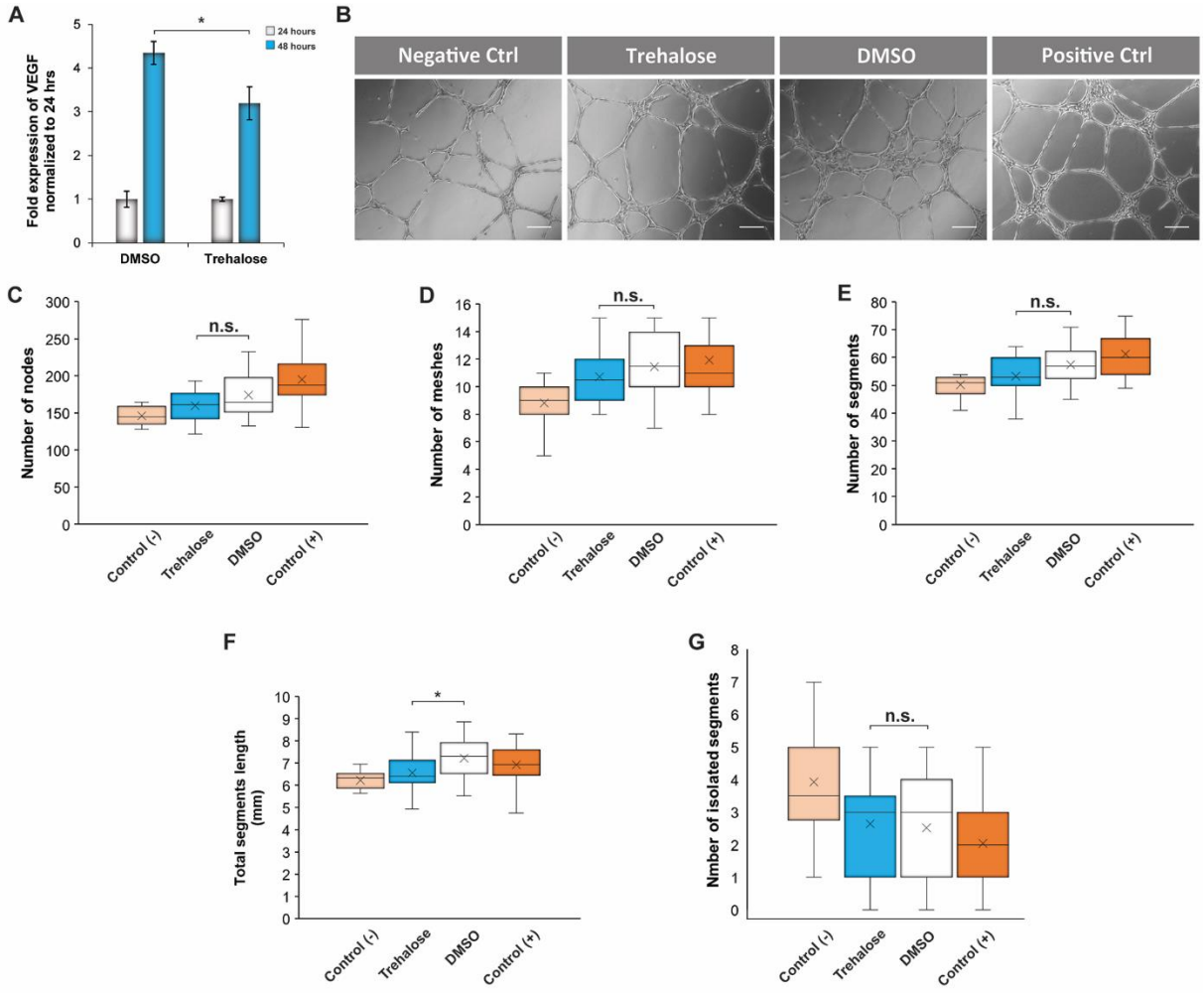

Figure 4.3 Assessment of the angiogenic potential of hASCs cryopreserved using trehalose vs. DMSO. A) Fold expression of VEGF secretion after 48 hours normalized to the amount of growth factor produced after 24 hours of culture. Results are reported as mean ± standard deviation (n=3). B) Bright-field images of HUVECs cultured on Matrigel and treated with different types of secretome derived from hASCs cryopreserved in freezing media supplemented with trehalose or DMSO. The negative control group was represented by endothelial cells cultured without any angiogenic growth factor. Scale bars = 400 µm. Image J quantification of several parameters regarding the network structure including C) number of nodes D) number of meshes E) number of segments F) total segments length in the network, and G) number of isolated segments. The results are reported as mean ± deviation standard (n=20). * = $p<0.05$, ** = $p<0.01$ *** = $p<0.001$.

4.3.5 Evaluation of osteogenic and adipogenic differentiation potential of hASCs post-cryopreservation using trehalose

The final step of this investigation aimed to verify the differentiation potential of hASCs into osteogenic and adipogenic lineages *in vitro* post-cryopreservation with trehalose. The evaluation of osteogenic differentiation was monitored by assessing the presence of the enzyme alkaline phosphatase (ALP), which is generally considered as an early osteogenic marker of differentiation. The ALP activity measured after 7 days of osteogenic differentiation was found to be similar between the DMSO and the trehalose group (**Figure 4.4A**). Similarly, hASCs started to deposit a significant amount of intracellular calcium that was detected by alizarin red staining after 14 days post-differentiation. No difference in the amount of intracellular calcium deposits was visible in the stained images of the cells cryopreserved with DMSO and trehalose after 14 days (**Figure 4.4B**).

hASCs were also successfully differentiated towards adipogenic lineage after 10 days of culture in adipogenic medium. qPCR analysis of main adipogenic gene markers such as *LPL*, *aP2*, and *PPARγ-2*, which are commonly upregulated in adipocytes, were quantified and compared between the two groups tested. Although *aP2* was found more expressed in hASCs cryopreserved in trehalose, the results were not statistically significant for any of the markers tested (**Figure 4.4C**). Similarly, hASCs adipogenic differentiation was evaluated by staining with Oil red O to visualize the presence of intracellular lipid-filled droplets. Overall, the DMSO and the trehalose groups displayed a similar level of staining after 10 days of adipogenic differentiation (**Figure 4.4D**). Finally, we also verified whether the process of squeezing used to deliver trehalose has any effect on the differentiation potential of hASCs prior to freezing. The same studies have been carried out comparing the osteogenic and adipogenic differentiation of hASCs passed through the microfluidic

device and untreated cells. No significant change was observed in ALP quantification on day 7 and alizarin red staining at 14 days between the two group tested (**Figure S4.4A-B**). Similarly, the process of squeezing did not alter the ability of the cells to differentiate towards the adipogenic lineage and similar level of staining and expression of *LPL*, *aP2*, and *PPAR-γ2* was found for both groups analyzed (**Figure S4.4C-D**).

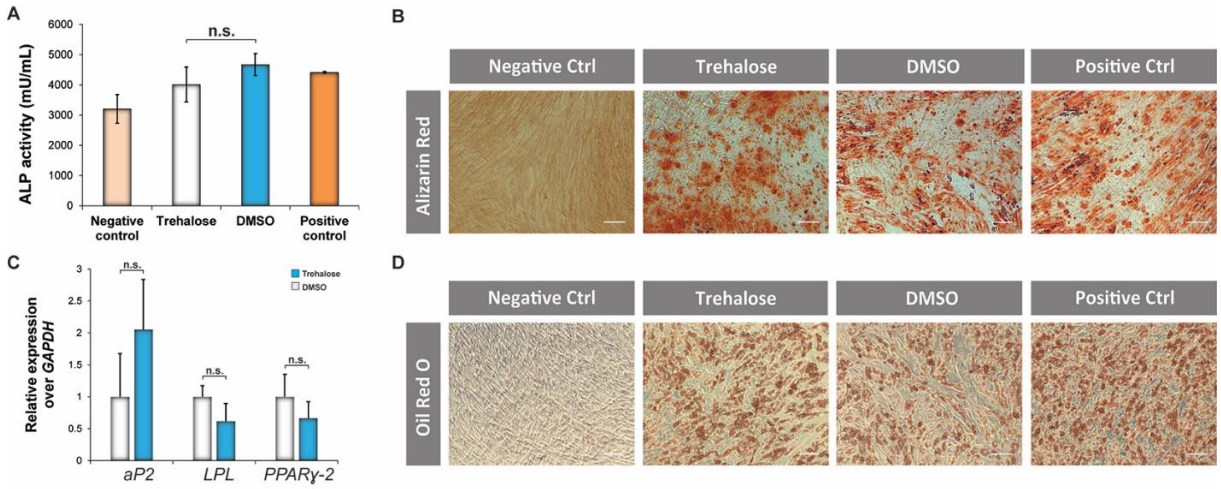

Figure 4.4 Assessment of osteogenic and adipogenic differentiation of hASCs cryopreserved with trehalose vs. DMSO. A) Alkaline phosphatase quantification of hASCs for the different groups after 7 days of osteogenic differentiation. B) Alizarin red staining to detect the presence of intracellular deposits of calcium in the different groups after 14 days of osteogenic differentiation. Scale bars = 200µm C) qPCR analysis of *PPARγ-2*, *aP2*, *LPL* genes, which are commonly upregulated during the process of adipogenic differentiation of stem cells after 10 days. *GAPDH* was used as the housekeeping gene. Results are reported as mean ± deviation standard (n=3). * = $p<0.05$, ** = $p<0.01$ *** = $p<0.001$. D) Oil Red O staining of hASCs differentiated in the adipogenic medium after 10 days to visualize the presence of intracellular lipid-filled droplets.

The results reported in this investigation are confirmed by other reports were trehalose was delivered intracellularly through alternative delivery methods. For instance, Dovgan *et al.* promoted the internalization of trehalose by electroporation in hASCs and found that the stem cells

were able to successfully differentiate similarly into osteogenic and adipogenic lineages [289]. Similarly, in another study by Rao *et al.*, trehalose was delivered using chitosan nanoparticles into hASCs. After cryopreservation, hASCs displayed similar differentiation potential towards adipogenic, osteogenic, and chondrogenic lineages with respect to cells without any step of cryopreservation [241]. Overall, these recent studies, combined with the findings reported in this work, strongly support the use of trehalose as a safe alternative to DMSO for the cryopreservation of hASCs.

4.4 Conclusions

The findings reported in Chapter 4 highlights the possibility of delivering trehalose intracellularly using the optimized microfluidic device. This strategy is efficient and does not require any toxic carrier for the delivery of trehalose. The amount of disaccharide required to obtain the highest cell viability post-cryopreservation has been optimized both intracellularly and extracellularly. Precisely, an extracellular concentration of 400 mM and an intracellular amount of 42.8 ± 5.76 mM were required to achieve the best results in terms of cell viability.

Cells cryopreserved in trehalose displayed a similar proliferation rate, negligible apoptosis, and retention of stemness markers with similar results for the cells cryopreserved in DMSO. Additionally, the angiogenic potential of hASCs cryopreserved using trehalose was comparable to the cells frozen with DMSO as demonstrated by *in vitro* angiogenic assays. Finally, the osteogenic and adipogenic differentiation potential of hASCs *in vitro* was preserved after cryopreservation irrespective of the CPA used.

In conclusion, further validation of these promising *in vitro* results should be provided by testing the *in vivo* efficacy of hASCs cryopreserved with trehalose. An example in this direction could be

the assessment of the angiogenic potential *in vivo* of hASCs when co-administered with endothelial cells to promote wound healing. Similarly, a complete transcriptome analysis of hASCs cryopreserved in trehalose and DMSO could be necessary to exclude any variation occurring during the freezing step in the gene expression of key markers, which are important regulators of the cellular metabolic functionality.

CHAPTER 5. Conclusions and future directions

The work discussed in the previous chapters provides direct examples of how intracellular delivery is a powerful tool that can be optimized and controlled to obtain specific cellular responses based on the type of cargo delivered into the cytosol.

Firstly, in **Chapter 2**, we have investigated a carrier-based strategy to deliver plasmid DNA into stem cells taking into consideration the stiffness of the substrates as a modulator of transfection efficiency. We have demonstrated how the cell microenvironment plays a crucial role in defining the efficiency of transfection when using Lipofectamine2000, which is a widely used lipid-based carrier for gene delivery. Interestingly, stiffer substrates can augment both the internalization of lipoplexes and the transfection efficiency of hASCs. Our findings suggest a direct correlation between the observed changes in cytoskeletal rearrangement and the internalization of the lipoplexes. Additionally, we observed how caveolae-mediated genes are upregulated in the hASCs cultured on the stiffer silicone substrates, thus confirming the role of actin as a key mediator in the internalization of plasmid lipoplexes. Finally, the results indicate how transfected hASCs seeded on more rigid substrates exhibited higher levels of VEGF expression when compared to hASCs cultured on softer hydrogels.

Based on these promising results, ideally, the same strategy proposed in this study could be applied to other types of stem cells to enhance transfection efficiency by using Lipofectamine. Gathering evidence from different sources of stem cells could be useful to further validate the impact of our findings and extend the applicability of our strategy for gene delivery applications.

Aside from the stiffness, other physical factors defining the properties of the cell-substrate can be varied at the same time to augment transfection efficiency. One interesting approach would be to modulate both the stiffness and the topography and verify whether this dual effect may be

beneficial in improving the internalization of the lipoplexes used in this study. Finally, to further expand the understanding of how stiffness influence cell transfection in hASCs it would be also important to carry out the same experiment in a 3D model with a range of hydrogels displaying the same value of stiffness (0.5 kPa to 32 kPa). Cells encapsulated in a 3D microenvironment commonly display a different ability to uptake extracellular cargo and numerous parameters such as porosity, degradability aside from the substrate stiffness may play a decisive role in defining the yield of transfection.

Another important aim addressed in this dissertation was the design of a microfluidic device to promote the intracellular delivery of trehalose. The design of the microfluidic chip described in **Chapter 3** was optimized to promote maximum intracellular delivery of external cargo and minimal cytotoxic effects. The efficiency of the microfluidic chips strictly depended on the gap size of the micro-constrictions, the molecular weight of the cargo delivered, and the design of the geometry used to fabricate the chip. Specifically, a gap size of 8 μm was found to be the optimal distance that promoted the maximum efficiency of internalization with minimal toxicity. Similarly, the double deformation design proved to be more effective than the single deformation strategy in enhancing the delivery of extracellular cargo. hASCs displayed minimal apoptosis and retained their stemness.

The optimal microfluidic chip design was used to deliver trehalose intracellularly as discussed and studied in **Chapter 4**. hASCs loaded with trehalose could be successfully cryopreserved in freezing media containing 400 mM trehalose. Upon thawing similar cell viability, proliferation rate, morphology, percentage of apoptotic cells, and differentiation potential was found for both hASCs loaded with trehalose and hASCs cryopreserved in DMSO. These results indicate that trehalose was effective in preserving the hASCs' functionality *in vitro* post cryopreservation.

Among different strategies for intracellular delivery of trehalose, our proposed method offers a carrier-free platform to deliver extracellular components without causing any cytotoxic effect. For instance, designed delivery platforms based on pH-responsive polymers and cell-penetrating peptides can be used to efficiently load high amounts of intracellular trehalose. However, the risk of cell toxicity remains a big challenge for the clinical translation of these strategies [285, 296]. Small transient pores are generated in the cell membrane by squeezing the cells through micron-sized constrictions of desired geometry [170, 226, 297]. This process allows the internalization of extracellular materials into the cytoplasm without the need for a toxic carrier [227, 228].

Similarly, trehalose could be delivered by mechanical disruption of the cell membrane using external energy sources, including ultrasound, electrical, and thermal stress [167, 287-289]. Unfortunately, some of these methods (such as electroporation) can cause membrane instability and protein denaturation, and hence, thorough optimization is needed [298, 299]. On the contrary, the mechanical disruption of the cell membrane described in this thesis is a reversible process that enables efficient internalization of extracellular components with minimal decrease in cell viability. Finally, the proposed carrier-free strategy could be potentially translated into clinical settings. Stem cells isolated from healthy subjects can be ideally treated with the designed microfluidic chip to deliver trehalose to millions of cells in a short amount of time (minutes). Following this step, stem cells can be cryopreserved for long-term storage without the use of any DMSO. However, post-thawed cells should be thoroughly washed to remove all trehalose both extracellularly and intracellularly. Additionally, the genetic profile of stem cells cryopreserved using trehalose should be monitored after several passages post-cryopreservation.

It should also be noted that there are few limitations in using microfluidic chips for the delivery of trehalose. For instance, clogging of the microfluidic channels by larger cells during each

experiment is inevitable. This problem arises from the inhomogeneity in the diameter of the cell population. As a result, the same chip cannot be used for another experiment, and hence, it increases the time and labor for fabrication of more chips. The other limitation is instead associated with the fabrication of the microfluidic chips. Precisely, fabricating micron-sized features with an exact desirable length is merely possible. This shortcoming is caused by the limitation of instruments involved in the fabrication process, such as UV mask aligner and SU8 spin coater. These limitations should be taken to account when designing microfluidic chips to fabricate high throughput delivery platforms for cell therapy and other applications.

Overall, the work presented in this thesis achieved two major milestones. The first main point is that transfection efficiency using lipid-based carrier can be augmented by increasing the stiffness of the substrate. This important concept could be potentially applied to other type of carrier-based strategies to improve the intracellular delivery of genetic material and advance the field of gene-based therapies. Secondly, the work presented in this thesis is the first described attempt to deliver trehalose intracellularly by using a microfluidic chip. The investigated strategy is non-toxic to cells and can promote the successful cryopreservation of stem cells without any significant change in cell functionality.

REFERENCES

1. Shinoda, W., *Biochimica et Biophysica Acta (BBA) - Biomembranes* 2016, *1858* (10), 2254-2265.
2. Yang, N. J.; Hinner, M. J., *Methods Mol Biol* 2015, *1266*, 29-53.
3. Lingwood, D.; Simons, K., *Science (New York, N.Y.)* 2010, *327* (5961), 46-50.
4. van Meer, G.; Voelker, D. R.; Feigenson, G. W., *Nature Reviews Molecular Cell Biology* 2008, *9*, 112.
5. Stewart, M. P.; Langer, R.; Jensen, K. F., *Chem Rev* 2018, *118* (16), 7409-7531.
6. Yin, H.; Kanasty, R. L.; Eltoukhy, A. A.; Vegas, A. J.; Dorkin, J. R.; Anderson, D. G., *Nature Reviews Genetics* 2014, *15*, 541.
7. Mali, S., *Indian J Hum Genet* 2013, *19* (1), 3-8.
8. Medina-Kauwe, L. K.; Xie, J.; Hamm-Alvarez, S., *Gene Ther* 2005, *12* (24), 1734-1751.
9. Mislick, K. A.; Baldeschwieler, J. D., *Proceedings of the National Academy of Sciences of the United States of America* 1996, *93* (22), 12349-54.
10. Mounkes, L. C.; Zhong, W.; Cipres-Palacin, G.; Heath, T. D.; Debs, R. J., *The Journal of biological chemistry* 1998, *273* (40), 26164-70.
11. Grant, B. D.; Donaldson, J. G., *Nature reviews. Molecular cell biology* 2009, *10* (9), 597-608.
12. Samaj, J.; Baluska, F.; Voigt, B.; Schlicht, M.; Volkmann, D.; Menzel, D., *Plant Physiol* 2004, *135* (3), 1150-1161.
13. McMahon, H. T.; Boucrot, E., *Nature reviews. Molecular cell biology* 2011, *12* (8), 517-33.
14. Rejman, J.; Oberle, V.; Zuhorn, I. S.; Hoekstra, D., *Biochem J* 2004, *377* (Pt 1), 159-169.
15. El-Sayed, A.; Harashima, H., *Molecular therapy : the journal of the American Society of Gene Therapy* 2013, *21* (6), 1118-30.

16. Billiet, L.; Gomez, J.-P.; Berchel, M.; Jaffrès, P.-A.; Le Gall, T.; Montier, T.; Bertrand, E.; Cheradame, H.; Guégan, P.; Mével, M.; Pitard, B.; Benvegnu, T.; Lehn, P.; Pichon, C.; Midoux, P., *Biomaterials* 2012, *33* (10), 2980-2990.
17. Smart, E. J.; Graf, G. A.; McNiven, M. A.; Sessa, W. C.; Engelman, J. A.; Scherer, P. E.; Okamoto, T.; Lisanti, M. P., *Molecular and cellular biology* 1999, *19* (11), 7289-304.
18. Parton, R. G.; del Pozo, M. A., *Nature reviews. Molecular cell biology* 2013, *14* (2), 98-112.
19. Mundy, D. I.; Machleidt, T.; Ying, Y.-s.; Anderson, R. G. W.; Bloom, G. S., *Journal of Cell Science* 2002, *115* (22), 4327-4339.
20. Echarri, A.; Muriel, O.; Pavón, D. M.; Azegrouz, H.; Escolar, F.; Terrón, M. C.; Sanchez-Cabo, F.; Martínez, F.; Montoya, M. C.; Llorca, O.; del Pozo, M. A., *Journal of Cell Science* 2012, *125* (13), 3097-3113.
21. Muriel, O.; Echarri, A.; Hellriegel, C.; Pavón, D. M.; Beccari, L.; Del Pozo, M. A., *Journal of Cell Science* 2011, *124* (16), 2763-2776.
22. Engel, S.; Heger, T.; Mancini, R.; Herzog, F.; Kartenbeck, J.; Hayer, A.; Helenius, A., *Journal of virology* 2011, *85* (9), 4198-211.
23. Koltover, I.; Salditt, T.; Radler, J. O.; Safinya, C. R., *Science (New York, N.Y.)* 1998, *281* (5373), 78-81.
24. Litzinger, D. C.; Huang, L., *Biochimica et Biophysica Acta (BBA) - Reviews on Biomembranes* 1992, *1113* (2), 201-227.
25. Mok, K. W.; Cullis, P. R., *Biophys J* 1997, *73* (5), 2534-2545.
26. Xu, Y.; Szoka, F. C., *Biochemistry* 1996, *35* (18), 5616-5623.
27. Tros de Ilarduya, C.; Sun, Y.; Duzgunes, N., *European journal of pharmaceutical sciences : official journal of the European Federation for Pharmaceutical Sciences* 2010, *40* (3), 159-70.
28. Read, M. L.; Bremner, K. H.; Oupicky, D.; Green, N. K.; Searle, P. F.; Seymour, L. W., *The journal of gene medicine* 2003, *5* (3), 232-45.
29. Lukacs, G. L.; Haggie, P.; Seksek, O.; Lechardeur, D.; Freedman, N.; Verkman, A. S., *Journal of Biological Chemistry* 2000, *275* (3), 1625-1629.
30. Salman, H.; Abu-Arish, A.; Oliel, S.; Loyter, A.; Klafter, J.; Granek, R.; Elbaum, M., *Biophys J* 2005, *89* (3), 2134-2145.
31. Suh, J.; Wirtz, D.; Hanes, J., *Proceedings of the National Academy of Sciences* 2003, *100* (7), 3878-3882.
32. Vaughan, E. E.; Dean, D. A., *Molecular therapy : the journal of the American Society of Gene Therapy* 2006, *13* (2), 422-428.
33. Tros de Ilarduya, C.; Sun, Y.; Düzgüneş, N., *European Journal of Pharmaceutical Sciences* 2010, *40* (3), 159-170.
34. Zanta, M. A.; Belguise-Valladier, P.; Behr, J. P., *Proceedings of the National Academy of Sciences of the United States of America* 1999, *96* (1), 91-96.
35. Vacik, J.; Dean, B. S.; Zimmer, W. E.; Dean, D. A., *Gene Therapy* 1999, *6* (6), 1006-1014.
36. Lundstrom, K., *Diseases* 2018, *6* (2), 42.
37. Wang, D.; Tai, P. W. L.; Gao, G., *Nature Reviews Drug Discovery* 2019, *18* (5), 358-378.
38. Mancheno-Corvo, P.; Martin-Duque, P., *Clinical & translational oncology : official publication of the Federation of Spanish Oncology Societies and of the National Cancer Institute of Mexico* 2006, *8* (12), 858-67.
39. Lyons, M.; Onion, D.; Green, N. K.; Aslan, K.; Rajaratnam, R.; Bazan-Peregrino, M.; Phipps, S.; Hale, S.; Mautner, V.; Seymour, L. W.; Fisher, K. D., *Molecular therapy : the journal of the American Society of Gene Therapy* 2006, *14* (1), 118-28.
40. Lukashev, A. N.; Zamyatnin, A. A., Jr., *Biochemistry. Biokhimiia* 2016, *81* (7), 700-8.
41. Keeler, A. M.; ElMallah, M. K.; Flotte, T. R., *Clin Transl Sci* 2017, *10* (4), 242-248.
42. Cattoglio, C.; Pellin, D.; Rizzi, E.; Maruggi, G.; Corti, G.; Miselli, F.; Sartori, D.; Guffanti, A.; Di Serio, C.; Ambrosi, A.; De Bellis, G.; Mavilio, F., *Blood* 2010, *116* (25), 5507-17.
43. Vigna, E.; Naldini, L., *The journal of gene medicine* 2000, *2* (5), 308-316.

44. Cartier, N.; Hacein-Bey-Abina, S.; Bartholomae, C. C.; Veres, G.; Schmidt, M.; Kutschera, I.; Vidaud, M.; Abel, U.; Dal-Cortivo, L.; Caccavelli, L.; Mahlaoui, N.; Kiermer, V.; Mittelstaedt, D.; Bellesme, C.; Lahlou, N.; Lefrère, F.; Blanche, S.; Audit, M.; Payen, E.; Leboulch, P.; l'Homme, B.; Bougnères, P.; Von Kalle, C.; Fischer, A.; Cavazzana-Calvo, M.; Aubourg, P., *Science (New York, N.Y.)* 2009, *326* (5954), 818-823.
45. Baum, C.; Kustikova, O.; Modlich, U.; Li, Z.; Fehse, B., *Hum Gene Ther* 2006, *17* (3), 253-63.
46. Bessis, N.; GarciaCozar, F. J.; Boissier, M. C., *Gene Ther* 2004, *11 Suppl 1*, S10-7.
47. Nayerossadat, N.; Maedeh, T.; Ali, P. A., *Adv Biomed Res* 2012, *1*, 27-27.
48. Ramamoorth, M.; Narvekar, A., *J Clin Diagn Res* 2015, *9* (1), GE01-GE6.
49. Perez-Martinez, F. C.; Carrion, B.; Cena, V., *Journal of Alzheimer's disease : JAD* 2012, *31* (4), 697-710.
50. Erathodiyil, N.; Ying, J. Y., *Accounts of Chemical Research* 2011, *44* (10), 925-935.
51. Guo, X.; Huang, L., *Accounts of chemical research* 2012, *45* (7), 971-979.
52. Son, S.; Nam, J.; Kim, J.; Kim, S.; Kim, W. J., *ACS Nano* 2014, *8* (6), 5574-5584.
53. Wu, P.; Yan, X. P., *Chem Soc Rev* 2013, *42* (12), 5489-521.
54. Ghafary, S. M.; Nikkhah, M.; Hatamie, S.; Hosseinkhani, S., *Scientific Reports* 2017, *7* (1), 9552.
55. Cao, X.; Wang, J.; Deng, W.; Chen, J.; Wang, Y.; Zhou, J.; Du, P.; Xu, W.; Wang, Q.; Wang, Q.; Yu, Q.; Spector, M.; Yu, J.; Xu, X., *Scientific reports* 2018, *8* (1), 7057-7057.
56. Yang, H. N.; Park, J. S.; Jeon, S. Y.; Park, W.; Na, K.; Park, K.-H., *Biomaterials* 2014, *35* (29), 8439-8449.
57. Srinivasan, C.; Lee, J.; Papadimitrakopoulos, F.; Silbart, L. K.; Zhao, M.; Burgess, D. J., *Molecular Therapy* 2006, *14* (2), 192-201.
58. Liang, Q.; Ma, W.; Shi, Y.; Li, Z.; Yang, X., *Carbon* 2013, *60*, 421-428.
59. Roy, I.; Mitra, S.; Maitra, A.; Mozumdar, S., *International journal of pharmaceutics* 2003, *250* (1), 25-33.
60. Sokolova, V.; Epple, M., *Angewandte Chemie (International ed. in English)* 2008, *47* (8), 1382-95.
61. Orrantia, E.; Chang, P. L., *Experimental Cell Research* 1990, *190* (2), 170-174.
62. Olton, D.; Li, J.; Wilson, M. E.; Rogers, T.; Close, J.; Huang, L.; Kumta, P. N.; Sfeir, C., *Biomaterials* 2007, *28* (6), 1267-1279.
63. Sokolova, V. V.; Radtke, I.; Heumann, R.; Epple, M., *Biomaterials* 2006, *27* (16), 3147-53.
64. Graham, F. L.; van der Eb, A. J., *Virology* 1973, *52* (2), 456-467.
65. Balavoine, F.; Schultz, P.; Richard, C.; Mallouh, V.; Ebbesen, T. W.; Mioskowski, C., *Angewandte Chemie International Edition* 1999, *38* (13-14), 1912-1915.
66. Hu, H.; Ni, Y.; Montana, V.; Haddon, R. C.; Parpura, V., *Nano Lett* 2004, *4* (3), 507-511.
67. Liu, Z.; Winters, M.; Holodniy, M.; Dai, H., *Angewandte Chemie International Edition* 2007, *46* (12), 2023-2027.
68. Klumpp, C.; Kostarelos, K.; Prato, M.; Bianco, A., *Biochimica et Biophysica Acta (BBA) - Biomembranes* 2006, *1758* (3), 404-412.
69. Taft, B. J.; Lazareck, A. D.; Withey, G. D.; Yin, A.; Xu, J. M.; Kelley, S. O., *Journal of the American Chemical Society* 2004, *126* (40), 12750-1.
70. Gao, H.; Kong, Y., *Annual Review of Materials Research* 2004, *34* (1), 123-150.
71. Qiu, X.; Ke, F.; Timsina, R.; Khripin, C. Y.; Zheng, M., *The Journal of Physical Chemistry C* 2016, *120* (25), 13831-13835.
72. Pantarotto, D.; Singh, R.; McCarthy, D.; Erhardt, M.; Briand, J.-P.; Prato, M.; Kostarelos, K.; Bianco, A., *Angewandte Chemie International Edition* 2004, *43* (39), 5242-5246.
73. Liu, Y.; Wu, D.-C.; Zhang, W.-D.; Jiang, X.; He, C.-B.; Chung, T. S.; Goh, S. H.; Leong, K. W., *Angewandte Chemie International Edition* 2005, *44* (30), 4782-4785.
74. Jia, G.; Wang, H.; Yan, L.; Wang, X.; Pei, R.; Yan, T.; Zhao, Y.; Guo, X., *Environmental science & technology* 2005, *39* (5), 1378-83.
75. Riley, M. K.; Vermerris, W., *Nanomaterials (Basel, Switzerland)* 2017, *7* (5).

76. Hoekstra, S. A. D., *Molecular Membrane Biology* 2001, *18* (2), 129-143.
77. Sork, H.; Nordin, J. Z.; Turunen, J. J.; Wiklander, O. P. B.; Bestas, B.; Zaghloul, E. M.; Margus, H.; Padari, K.; Duru, A. D.; Corso, G.; Bost, J.; Vader, P.; Pooga, M.; Smith, C. I. E.; Wood, M. J. A.; Schiffelers, R. M.; Hällbrink, M.; Andaloussi, S. E. L., *Molecular Therapy - Nucleic Acids* 2016, *5*, e290.
78. Torchilin, V. P.; Levchenko, T. S.; Rammohan, R.; Volodina, N.; Papahadjopoulos-Sternberg, B.; D'Souza, G. G., *Proceedings of the National Academy of Sciences of the United States of America* 2003, *100* (4), 1972-7.
79. Zou, S.; Scarfo, K.; Nantz, M. H.; Hecker, J. G., *International journal of pharmaceutics* 2010, *389* (1-2), 232-243. 80. Gascón, A. R.; Pedraz, J. L., *Expert Opinion on Therapeutic Patents* 2008, *18* (5), 515-524.
81. Rejman, J.; Oberle, V.; Zuhorn, I. S.; Hoekstra, D., *Biochemical Journal* 2004, *377* (1), 159-169.
82. Kamimura, K.; Suda, T.; Zhang, G.; Liu, D., *Pharmaceut Med* 2011, *25* (5), 293-306.
83. Foldvari, M.; Chen, D. W.; Nafissi, N.; Calderon, D.; Narsineni, L.; Rafiee, A., *Journal of Controlled Release* 2016, *240*, 165-190.
84. Stopeck, A. T.; Hersh, E. M.; Akporiaye, E. T.; Harris, D. T.; Grogan, T.; Unger, E.; Warneke, J.; Schluter, S. F.; Stahl, S., *Journal of clinical oncology : official journal of the American Society of Clinical Oncology* 1997, *15* (1), 341-9.
85. Nabel, G. J.; Nabel, E. G.; Yang, Z. Y.; Fox, B. A.; Plautz, G. E.; Gao, X.; Huang, L.; Shu, S.; Gordon, D.; Chang, A. E., *Proceedings of the National Academy of Sciences of the United States of America* 1993, *90* (23), 11307-11311.
86. Caplen, N. J.; Alton, E. W.; Middleton, P. G.; Dorin, J. R.; Stevenson, B. J.; Gao, X.; Durham, S. R.; Jeffery, P. K.; Hodson, M. E.; Coutelle, C.; et al., *Nature medicine* 1995, *1* (1), 39-46.
87. Lai, W. F.; Wong, W. T., *Trends in biotechnology* 2018, *36* (7), 713-728.
88. Glodde, M.; Sirsi, S. R.; Lutz, G. J., *Biomacromolecules* 2006, *7* (1), 347-356.
89. Dash, P. R.; Read, M. L.; Barrett, L. B.; Wolfert, M. A.; Seymour, L. W., *Gene Therapy* 1999, *6* (4), 643-650.
90. Jokerst, J. V.; Lobovkina, T.; Zare, R. N.; Gambhir, S. S., *Nanomedicine (Lond)* 2011, *6* (4), 715-728.
91. Oroojalian, F.; Rezayan, A. H.; Shier, W. T.; Abnous, K.; Ramezani, M., *International journal of pharmaceutics* 2017, *523* (1), 102-120.
92. Gonzalez-Fernandez, T.; Sathy, B. N.; Hobbs, C.; Cunniffe, G. M.; McCarthy, H. O.; Dunne, N. J.; Nicolosi, V.; O'Brien, F. J.; Kelly, D. J., *Acta Biomaterialia* 2017, *55*, 226-238.
93. Zakeri, A.; Kouhbanani, M. A. J.; Beheshtkhoo, N.; Beigi, V.; Mousavi, S. M.; Hashemi, S. A. R.; Karimi Zade, A.; Amani, A. M.; Savardashtaki, A.; Mirzaei, E.; Jahandideh, S.; Movahedpour, A., *Nano Reviews & Experiments* 2018, *9* (1), 1488497.
94. Wing-Fu, L.; David, W. G.; Han-Sung, J., *Current Gene Therapy* 2014, *14* (4), 258-268.
95. Varkouhi, A. K.; Scholte, M.; Storm, G.; Haisma, H. J., *Journal of Controlled Release* 2011, *151* (3), 220-228.
96. Florea, B. I.; Meaney, C.; Junginger, H. E.; Borchard, G., *AAPS pharmSci* 2002, *4* (3), E12.
97. He, Y.; Cheng, G.; Xie, L.; Nie, Y.; He, B.; Gu, Z., *Biomaterials* 2013, *34* (4), 1235-1245.
98. Zeng, L.; Li, J.; Wang, Y.; Qian, C.; Chen, Y.; Zhang, Q.; Wu, W.; Lin, Z.; Liang, J.; Shuai, X.; Huang, K., *Nanomedicine: Nanotechnology, Biology and Medicine* 2014, *10* (2), 463-472.
99. Zhang, X.; Oulad-Abdelghani, M.; Zelkin, A. N.; Wang, Y.; Haîkel, Y.; Mainard, D.; Voegel, J.-C.; Caruso, F.; Benkirane-Jessel, N., *Biomaterials* 2010, *31* (7), 1699-1706.
100. Merdan, T.; Kunath, K.; Fischer, D.; Kopecek, J.; Kissel, T., *Pharmaceutical research* 2002, *19* (2), 140-6.
101. Merdan, T.; Kopeček, J.; Kissel, T., *Advanced Drug Delivery Reviews* 2002, *54* (5), 715-758.
102. Pichon, C.; Gonçalves, C.; Midoux, P., *Advanced Drug Delivery Reviews* 2001, *53* (1), 75-94.
103. Kshitiz; Afzal, J.; Chang, H.; Goyal, R.; Levchenko, A., *Current Stem Cell Reports* 2016, *2* (1), 62-72.
104. Vining, K. H.; Mooney, D. J., *Nature reviews. Molecular cell biology* 2017, *18* (12), 728-742.

105. Dhaliwal, A.; Lam, J.; Maldonado, M.; Lin, C.; Segura, T., *Soft Matter* 2012, *8* (5), 1451-1459.
106. Adler, A. F.; Leong, K. W., *Nano today* 2010, *5* (6), 553-569.
107. Dhaliwal, A.; Maldonado, M.; Lin, C.; Segura, T., *PLoS One* 2012, *7* (4), e35046-e35046.
108. Burridge, K.; Guilluy, C., *Experimental cell research* 2016, *343* (1), 14-20.
109. Hsu, S.-h.; Ho, T.-T.; Tseng, T.-C., *Biomaterials* 2012, *33* (14), 3639-3650.
110. Scotchford, C. A.; Gilmore, C. P.; Cooper, E.; Leggett, G. J.; Downes, S., *Journal of Biomedical Materials Research* 2002, *59* (1), 84-99.
111. Kasputis, T.; Pannier, A. K., *Journal of biological engineering* 2012, *6* (1), 17.
112. Kasputis, T.; Farris, E.; Guerreiro, G.; Taylor, J.; Pannier, A. K., Substrate-Mediated Gene Delivery. In *The World Scientific Encyclopedia of Nanomedicine and Bioengineering I*, pp 219-260.
113. Mantz, A.; Pannier, A. K., *Experimental biology and medicine (Maywood, N.J.)* 2019, *244* (2), 100-113.
114. Pannier, A. K.; Anderson, B. C.; Shea, L. D., *Acta Biomaterialia* 2005, *1* (5), 511-522.
115. Bengali, Z.; Pannier, A. K.; Segura, T.; Anderson, B. C.; Jang, J.-H.; Mustoe, T. A.; Shea, L. D., *Biotechnol Bioeng* 2005, *90* (3), 290-302.
116. Bengali, Z.; Rea, J. C.; Shea, L. D., *The journal of gene medicine* 2007, *9* (8), 668-78.
117. Reich, U.; Fadeeva, E.; Warnecke, A.; Paasche, G.; Müller, P.; Chichkov, B.; Stöver, T.; Lenarz, T.; Reuter, G., *Journal of Biomedical Materials Research Part B: Applied Biomaterials* 2012, *100B* (4), 940-947.
118. Yip, A. K.; Iwasaki, K.; Ursekar, C.; Machiyama, H.; Saxena, M.; Chen, H.; Harada, I.; Chiam, K.-H.; Sawada, Y., *Biophys J* 2013, *104* (1), 19-29.
119. Skoog, S. A.; Kumar, G.; Narayan, R. J.; Goering, P. L., *Pharmacology & Therapeutics* 2018, *182*, 33-55.
120. Nasrollahi, S.; Banerjee, S.; Qayum, B.; Banerjee, P.; Pathak, A., *ACS Biomaterials Science & Engineering* 2017, *3* (11), 2980-2986.
121. Coyer, S. R.; Singh, A.; Dumbauld, D. W.; Calderwood, D. A.; Craig, S. W.; Delamarche, E.; García, A. J., *Journal of Cell Science* 2012, *125* (21), 5110-5123.
122. Iwaya, Y.; Machigashira, M.; Kanbara, K.; Miyamoto, M.; Noguchi, K.; Izumi, Y.; Ban, S., *Dental materials journal* 2008, *27* (3), 415-21.
123. Lee, J. W.; Lee, K. B.; Jeon, H. S.; Park, H. K., *Analytical sciences : the international journal of the Japan Society for Analytical Chemistry* 2011, *27* (4), 369.
124. Teo, B. K. K.; Goh, S.-H.; Kustandi, T. S.; Loh, W. W.; Low, H. Y.; Yim, E. K. F., *Biomaterials* 2011, *32* (36), 9866-9875.
125. Huang, N.-C.; Sieber, M.; Hsu, S.-h., *Acta Biomaterialia* 2015, *28*, 55-63.
126. Vertelov, G.; Gutierrez, E.; Lee, S.-A.; Ronan, E.; Groisman, A.; Tkachenko, E., *Scientific Reports* 2016, *6*, 33411.
127. Wen, J. H.; Vincent, L. G.; Fuhrmann, A.; Choi, Y. S.; Hribar, K. C.; Taylor-Weiner, H.; Chen, S.; Engler, A. J., *Nature Materials* 2014, *13*, 979.
128. Engler, A. J.; Sen, S.; Sweeney, H. L.; Discher, D. E., *Cell* 2006, *126* (4), 677-689.
129. Huang, C.; Butler, P. J.; Tong, S.; Muddana, H. S.; Bao, G.; Zhang, S., *Nano Lett* 2013, *13* (4), 1611-1615.
130. Modaresi, S.; Pacelli, S.; Whitlow, J.; Paul, A., *Nanoscale* 2018, *10* (19), 8947-8952.
131. Kong, H. J.; Liu, J.; Riddle, K.; Matsumoto, T.; Leach, K.; Mooney, D. J., *Nature Materials* 2005, *4* (6), 460-464.
132. Chu, C.; Kong, H., *Acta Biomaterialia* 2012, *8* (7), 2612-2619.
133. Barber, M. A., *The Journal of Infectious Diseases* 1911, *8* (3), 348-360.
134. Kobayashi, N.; Rivas-Carrillo, J. D.; Soto-Gutierrez, A.; Fukazawa, T.; Chen, Y.; Navarro-Alvarez, N.; Tanaka, N., *Birth Defects Research Part C: Embryo Today: Reviews* 2005, *75* (1), 10-18.
135. Fire, A.; Xu, S.; Montgomery, M. K.; Kostas, S. A.; Driver, S. E.; Mello, C. C., *Nature* 1998, *391* (6669), 806-11.
136. Capecchi, M. R., *Cell* 1980, *22* (2, Part 2), 479-488.

137. Zhang, Y.; Hong, Y.; Bounhar, Y.; Blacker, M.; Roucou, X.; Tounekti, O.; Vereker, E.; Bowers, W. J.; Federoff, H. J.; Goodyer, C. G.; LeBlanc, A., *The Journal of neuroscience : the official journal of the Society for Neuroscience* 2003, *23* (19), 7385-94.
138. Roucou, X.; Giannopoulos, P. N.; Zhang, Y.; Jodoin, J.; Goodyer, C. G.; LeBlanc, A., *Cell death and differentiation* 2005, *12* (7), 783-95.
139. Zhang, Y.; Yu, L.-C., *Current Opinion in Biotechnology* 2008, *19* (5), 506-510.
140. Luo, D.; Saltzman, W. M., *Nature Biotechnology* 2000, *18* (1), 33-37.
141. Biju, V.; Itoh, T.; Ishikawa, M., *Chemical Society Reviews* 2010, *39* (8), 3031-3056.
142. Stewart, M. P.; Langer, R.; Jensen, K. F., *Chemical Reviews* 2018, *118* (16), 7409-7531.
143. Shalek, A. K.; Gaublomme, J. T.; Wang, L.; Yosef, N.; Chevrier, N.; Andersen, M. S.; Robinson, J. T.; Pochet, N.; Neuberg, D.; Gertner, R. S.; Amit, I.; Brown, J. R.; Hacohen, N.; Regev, A.; Wu, C. J.; Park, H., *Nano Lett* 2012, *12* (12), 6498-6504.
144. Shalek, A. K.; Robinson, J. T.; Karp, E. S.; Lee, J. S.; Ahn, D.-R.; Yoon, M.-H.; Sutton, A.; Jorgolli, M.; Gertner, R. S.; Gujral, T. S.; MacBeath, G.; Yang, E. G.; Park, H., *Proceedings of the National Academy of Sciences* 2010, *107* (5), 1870-1875.
145. McKnight, T. E.; Melechko, A. V.; Griffin, G. D.; Guillorn, M. A.; Merkulov, V. I.; Serna, F.; Hensley, D. K.; Doktycz, M. J.; Lowndes, D. H.; Simpson, M. L., *Nanotechnology* 2003, *14* (5), 551-556.
146. VanDersarl, J. J.; Xu, A. M.; Melosh, N. A., *Nano Lett* 2012, *12* (8), 3881-3886.
147. Wang, Y.; Yang, Y.; Yan, L.; Kwok, S. Y.; Li, W.; Wang, Z.; Zhu, X.; Zhu, G.; Zhang, W.; Chen, X.; Shi, P., *Nature Communications* 2014, *5*, 4466.
148. Sanford, J. C.; Smith, F. D.; Russell, J. A., [36] Optimizing the biolistic process for different biological applications. In *Methods in Enzymology*, Academic Press: 1993; Vol. 217, pp 483-509.
149. O'Brien, J. A.; Lummis, S. C. R., *Nature Protocols* 2006, *1* (2), 977-981.
150. Heiser, W. C., *Analytical Biochemistry* 1994, *217* (2), 185-196.
151. Belyantseva, I. A., Helios® Gene Gun–Mediated Transfection of the Inner Ear Sensory Epithelium. In *Auditory and Vestibular Research: Methods and Protocols*, Sokolowski, B., Ed. Humana Press: Totowa, NJ, 2009; pp 103-124.
152. Liang, Z.; Chen, K.; Li, T.; Zhang, Y.; Wang, Y.; Zhao, Q.; Liu, J.; Zhang, H.; Liu, C.; Ran, Y.; Gao, C., *Nature Communications* 2017, *8*, 14261.
153. Neumann, E.; Schaefer-Ridder, M.; Wang, Y.; Hofschneider, P. H., *The EMBO journal* 1982, *1* (7), 841-5.
154. Zhao, Y.; Zheng, Z.; Cohen, C. J.; Gattinoni, L.; Palmer, D. C.; Restifo, N. P.; Rosenberg, S. A.; Morgan, R. A., *Molecular Therapy* 2006, *13* (1), 151-159.
155. Sontag, R. L.; Mihai, C.; Orr, G.; Savchenko, A.; Skarina, T.; Cui, H.; Cort, J. R.; Adkins, J. N.; Brown, R. N., *Journal of visualized experiments : JoVE* 2015, (95), 52296.
156. Sun, C.; Cao, Z.; Wu, M.; Lu, C., *Analytical chemistry* 2014, *86* (22), 11403-9.
157. Marschall, A. L. J.; Zhang, C.; Frenzel, A.; Schirrmann, T.; Hust, M.; Perez, F.; Dübel, S., *MAbs* 2014, *6* (4), 943-956.
158. Yarmush, M. L.; Golberg, A.; Serša, G.; Kotnik, T.; Miklavčič, D., *Annual Review of Biomedical Engineering* 2014, *16* (1), 295-320.
159. Geng, T.; Lu, C., *Lab on a chip* 2013, *13* (19), 3803-21.
160. Movahed, S.; Li, D., *Microfluidics and Nanofluidics* 2011, *10* (4), 703-734.
161. Bischof, J. C.; Padanilam, J.; Holmes, W. H.; Ezzell, R. M.; Lee, R. C.; Tompkins, R. G.; Yarmush, M. L.; Toner, M., *Biophys J* 1995, *68* (6), 2608-14.
162. He, X.; Amin, A. A.; Fowler, A.; Toner, M., *Cell Preservation Technology* 2006, *4* (3), 178-187.
163. Cui, X.; Dean, D.; Ruggeri, Z. M.; Boland, T., *Biotechnol Bioeng* 2010, *106* (6), 963-9.
164. Stevenson, D. J.; Gunn-Moore, F. J.; Campbell, P.; Dholakia, K., *Journal of the Royal Society, Interface* 2010, *7* (47), 863-71.
165. Miller, D. L.; Pislaru, S. V.; Greenleaf, J. E., *Somatic cell and molecular genetics* 2002, *27* (1-6), 115-34.
166. Liu, Y.; Yan, J.; Prausnitz, M. R., *Ultrasound Med Biol* 2012, *38* (5), 876-888.

167. Ohl, C.-D.; Arora, M.; Ikink, R.; de Jong, N.; Versluis, M.; Delius, M.; Lohse, D., *Biophys J* 2006, *91* (11), 4285-4295.
168. Prentice, P.; Cuschieri, A.; Dholakia, K.; Prausnitz, M.; Campbell, P., *Nature Physics* 2005, *1* (2), 107-110.
169. Wu, Y.-C.; Wu, T.-H.; Clemens, D. L.; Lee, B.-Y.; Wen, X.; Horwitz, M. A.; Teitell, M. A.; Chiou, P.-Y., *Nature Methods* 2015, *12*, 439.
170. Lee, J.; Sharei, A.; Sim, W. Y.; Adamo, A.; Langer, R.; Jensen, K. F.; Bawendi, M. G., *Nano Lett* 2012, *12* (12), 6322-6327.
171. DiTommaso, T.; Cole, J. M.; Cassereau, L.; Buggé, J. A.; Hanson, J. L. S.; Bridgen, D. T.; Stokes, B. D.; Loughhead, S. M.; Beutel, B. A.; Gilbert, J. B.; Nussbaum, K.; Sorrentino, A.; Toggweiler, J.; Schmidt, T.; Gyuelveszi, G.; Bernstein, H.; Sharei, A., *Proceedings of the National Academy of Sciences* 2018, *115* (46), E10907-E10914.
172. Liu, A.; Islam, M.; Stone, N.; Varadarajan, V.; Jeong, J.; Bowie, S.; Qiu, P.; Waller, E. K.; Alexeev, A.; Sulchek, T., *Materials Today* 2018, *21* (7), 703-712.
173. Toner, M., *Nature Biomedical Engineering* 2017, *1*, 0047.
174. Liu, Z.; Han, X.; Zhou, Q.; Chen, R.; Fruge, S.; Jo, M. C.; Ma, Y.; Li, Z.; Yokoi, K.; Qin, L., *Advanced Biosystems* 2017, *1* (6), 1700054.
175. Sharei, A.; Poceviciute, R.; Jackson, E. L.; Cho, N.; Mao, S.; Hartoularos, G. C.; Jang, D. Y.; Jhunjhunwala, S.; Eyerman, A.; Schoettle, T.; Langer, R.; Jensen, K. F., *Integrative biology : quantitative biosciences from nano to macro* 2014, *6* (4), 470-5.
176. Stewart, M. P.; Sharei, A.; Ding, X.; Sahay, G.; Langer, R.; Jensen, K. F., *Nature* 2016, *538*, 183.
177. Sharei, A.; Zoldan, J.; Adamo, A.; Sim, W. Y.; Cho, N.; Jackson, E.; Mao, S.; Schneider, S.; Han, M.-J.; Lytton-Jean, A.; Basto, P. A.; Jhunjhunwala, S.; Lee, J.; Heller, D. A.; Kang, J. W.; Hartoularos, G. C.; Kim, K.-S.; Anderson, D. G.; Langer, R.; Jensen, K. F., *Proceedings of the National Academy of Sciences* 2013, *110* (6), 2082-2087.
178. Han, X.; Liu, Z.; Jo, M. c.; Zhang, K.; Li, Y.; Zeng, Z.; Li, N.; Zu, Y.; Qin, L., *Science Advances* 2015, *1* (7), e1500454.
179. Ding, X.; Stewart, M. P.; Sharei, A.; Weaver, J. C.; Langer, R. S.; Jensen, K. F., *Nature Biomedical Engineering* 2017, *1*, 0039.
180. Schönmeyr, B. H.; Soares, M.; Avraham, T.; Clavin, N. W.; Gewalli, F.; Mehrara, B. J., *Tissue Engineering. Part A* 2010, *16* (2), 653-662.
181. Nikol, S., *Cardiovasc Res* 2007, *73* (3), 443-5.
182. Seow, Y.; Wood, M. J., *Molecular Therapy 17* (5), 767-777.
183. Ramamoorth, M.; Narvekar, A., *J Clin Diagn Res* 2015, *9* (1), GE01-6.
184. Missirlis, D., *PLoS One* 2014, *9* (5), e96548.
185. Echarri, A.; Del Pozo, M. A., *Journal of Cell Science* 2015, *128* (15), 2747-2758.
186. Yao, L. H.; Rao, Y.; Bang, C.; Kurilova, S.; Varga, K.; Wang, C. Y.; Weller, B. D.; Cho, W.; Cheng, J.; Gong, L. W., *The Journal of neuroscience : the official journal of the Society for Neuroscience* 2013, *33* (40), 15793-8.
187. Smythe, E.; Ayscough, K. R., *Journal of Cell Science* 2006, *119* (22), 4589-4598.
188. Kong, H. J.; Liu, J.; Riddle, K.; Matsumoto, T.; Leach, K.; Mooney, D. J., *Nature materials* 2005, *4* (6), 460-4.
189. Butler, J. P.; Tolić-Nørrelykke, I. M.; Fabry, B.; Fredberg, J. J., *American Journal of Physiology - Cell Physiology* 2002, *282* (3), C595.
190. Carapuca, E.; Azzoni, A. R.; Prazeres, D. M.; Monteiro, G. A.; Mergulhao, F. J., *Molecular biotechnology* 2007, *37* (2), 120-6.
191. Vertelov, G.; Gutierrez, E.; Lee, S. A.; Ronan, E.; Groisman, A.; Tkachenko, E., *Sci Rep* 2016, *6*, 33411.
192. Pacelli, S.; Maloney, R.; Chakravarti, A. R.; Whitlow, J.; Basu, S.; Modaresi, S.; Gehrke, S.; Paul, A., *Sci Rep* 2017, *7* (1), 6577.

193. Prager-Khoutorsky, M.; Lichtenstein, A.; Krishnan, R.; Rajendran, K.; Mayo, A.; Kam, Z.; Geiger, B.; Bershadsky, A. D., *Nat Cell Biol* 2011, *13* (12), 1457-1465.
194. Ehrlicher, A. J.; Krishnan, R.; Guo, M.; Bidan, C. M.; Weitz, D. A.; Pollak, M. R., *Proceedings of the National Academy of Sciences of the United States of America* 2015, *112* (21), 6619-24.
195. Chi, X.; Wang, S.; Huang, Y.; Stamnes, M.; Chen, J. L., *Int J Mol Sci* 2013, *14* (4), 7089-108.
196. Son, K. K.; Patel, D. H.; Tkach, D.; Park, A., *Biochimica et Biophysica Acta (BBA) - Biomembranes* 2000, *1466* (1), 11-15.
197. Chu, C.; Kong, H., *Acta Biomater* 2012, *8* (7), 2612-9.
198. Cui, S.; Wang, B.; Zhao, Y.; Chen, H.; Ding, H.; Zhi, D.; Zhang, S., *Biotechnology letters* 2014, *36* (1), 1-7.
199. Cardarelli, F.; Digiacomo, L.; Marchini, C.; Amici, A.; Salomone, F.; Fiume, G.; Rossetta, A.; Gratton, E.; Pozzi, D.; Caracciolo, G., 2016, *6*, 25879.
200. Rejman, J.; Oberle, V.; Zuhorn, I. S.; Hoekstra, D., *The Biochemical journal* 2004, *377* (Pt 1), 159-69.
201. Yarak, S.; Okamoto, O. K., *Anais brasileiros de dermatologia* 2010, *85* (5), 647-56.
202. Paul, A.; Hasan, A.; Kindi, H. A.; Gaharwar, A. K.; Rao, V. T.; Nikkhah, M.; Shin, S. R.; Krafft, D.; Dokmeci, M. R.; Shum-Tim, D.; Khademhosseini, A., *ACS Nano* 2014, *8* (8), 8050-62.
203. Chen, G.; Shi, X.; Sun, C.; Li, M.; Zhou, Q.; Zhang, C.; Huang, J.; Qiu, Y.; Wen, X.; Zhang, Y.; Zhang, Y.; Yang, S.; Lu, L.; Zhang, J.; Yuan, Q.; Lu, J.; Xu, G.; Xue, Y.; Jin, Z.; Jiang, C.; Ying, M.; Liu, X., *PLoS One* 2013, *8* (10), e73673.
204. Dall'Era, J. E.; Meacham, R. B.; Mills, J. N.; Koul, S.; Carlsen, S. N.; Myers, J. B.; Koul, H. K., *Int J Impot Res* 2008, *20* (3), 307-314.
205. Schaffert, D.; Wagner, E., *Gene Therapy* 2008, *15*, 1131.
206. Whitehead, K. A.; Langer, R.; Anderson, D. G., *Nature Reviews Drug Discovery* 2010, *9*, 412.
207. Dhar, S.; Daniel, W. L.; Giljohann, D. A.; Mirkin, C. A.; Lippard, S. J., *Journal of the American Chemical Society* 2010, *132* (48), 17335-17335.
208. Jiang, Z.-X.; Zhang, Z.-Y., *Cancer and Metastasis Reviews* 2008, *27* (2), 263-272.
209. Derfus, A. M.; Chan, W. C. W.; Bhatia, S. N., *Advanced Materials* 2004, *16* (12), 961-966.
210. Michalet, X.; Pinaud, F. F.; Bentolila, L. A.; Tsay, J. M.; Doose, S.; Li, J. J.; Sundaresan, G.; Wu, A. M.; Gambhir, S. S.; Weiss, S., *Science (New York, N.Y.)* 2005, *307* (5709), 538-544.
211. Liu, Y.; Yan, J.; Prausnitz, M. R., *Ultrasound in Medicine and Biology* 2012, *38* (5), 876-888.
212. Yarmush, M. L.; Golberg, A.; Sersa, G.; Kotnik, T.; Miklavcic, D., *Annu Rev Biomed Eng* 2014, *16*, 295-320.
213. Venslauskas, M. S.; Šatkauskas, S., *European Biophysics Journal* 2015, *44* (5), 277-289.
214. Deng, Y.; Kizer, M.; Rada, M.; Sage, J.; Wang, X.; Cheon, D.-J.; Chung, A. J., *Nano Lett* 2018, *18* (4), 2705-2710.
215. Kollmannsperger, A.; Sharei, A.; Raulf, A.; Heilemann, M.; Langer, R.; Jensen, K. F.; Wieneke, R.; Tampé, R., *Nature Communications* 2016, *7*, 10372.
216. Lee, J.; Sharei, A.; Sim, W. Y.; Adamo, A.; Langer, R.; Jensen, K. F.; Bawendi, M. G., *Nano Lett* 2012, *12* (12), 6322-7.
217. Han, X.; Liu, Z.; Zhao, L.; Wang, F.; Yu, Y.; Yang, J.; Chen, R.; Qin, L., *Angewandte Chemie (International ed. in English)* 2016, *55* (30), 8561-5.
218. Adamo, A.; Sharei, A.; Adamo, L.; Lee, B.; Mao, S.; Jensen, K. F., *Analytical chemistry* 2012, *84* (15), 6438-43.
219. Jo, C. H.; Chai, J. W.; Jeong, E. C.; Oh, S.; Kim, P. S.; Yoon, J. Y.; Yoon, K. S., *STEM CELLS* 2018, *36* (9), 1441-1450.
220. Park, J.; Lee, N.; Lee, J.; Choe, E. K.; Kim, M. K.; Lee, J.; Byun, M. S.; Chon, M.-W.; Kim, S. W.; Lee, C. J.; Kim, J. H.; Kwon, J. S.; Chang, M.-S., *Scientific Reports* 2017, *7* (1), 10166.
221. Waters, R.; Alam, P.; Pacelli, S.; Chakravarti, A. R.; Ahmed, R. P. H.; Paul, A., *Acta Biomaterialia* 2018, *69*, 95-106.

222. Li, M.; Luo, X.; Lv, X.; Liu, V.; Zhao, G.; Zhang, X.; Cao, W.; Wang, R.; Wang, W., *Stem Cell Research & Therapy* 2016, *7* (1), 160.
223. Pacelli, S.; Maloney, R.; Chakravarti, A. R.; Whitlow, J.; Basu, S.; Modaresi, S.; Gehrke, S.; Paul, A., *Scientific Reports* 2017, *7* (1), 6577.
224. Yourek, G.; Hussain, M. A.; Mao, J. J., *ASAIO journal (American Society for Artificial Internal Organs : 1992)* 2007, *53* (2), 219-228.
225. Müller, P.; Langenbach, A.; Kaminski, A.; Rychly, J., *PLoS One* 2013, *8* (7), e71283.
226. Sharei, A.; Zoldan, J.; Adamo, A.; Sim, W. Y.; Cho, N.; Jackson, E.; Mao, S.; Schneider, S.; Han, M. J.; Lytton-Jean, A.; Basto, P. A.; Jhunjhunwala, S.; Lee, J.; Heller, D. A.; Kang, J. W.; Hartoularos, G. C.; Kim, K. S.; Anderson, D. G.; Langer, R.; Jensen, K. F., *Proceedings of the National Academy of Sciences of the United States of America* 2013, *110* (6), 2082-7.
227. Han, X.; Liu, Z.; Ma, Y.; Zhang, K.; Qin, L., *Advanced Biosystems* 2017, *1* (1-2), 1600007.
228. Han, X.; Liu, Z.; Jo, M. C.; Zhang, K.; Li, Y.; Zeng, Z.; Li, N.; Zu, Y.; Qin, L., *Sci Adv* 2015, *1* (7), e1500454.
229. Li, J.; Wang, B.; Juba, B. M.; Vazquez, M.; Kortum, S. W.; Pierce, B. S.; Pacheco, M.; Roberts, L.; Strohbach, J. W.; Jones, L. H.; Hett, E.; Thorarensen, A.; Telliez, J. B.; Sharei, A.; Bunnage, M.; Gilbert, J. B., *ACS chemical biology* 2017, *12* (12), 2970-2974.
230. Pathak-Sharma, S.; Zhang, X.; Lam, J. G. T.; Weisleder, N.; Seveau, S. M., *Frontiers in Cellular and Infection Microbiology* 2017, *7* (305).
231. McNeil, P. L.; Steinhardt, R. A., *Annual review of cell and developmental biology* 2003, *19*, 697-731.
232. Cooper, S. T.; McNeil, P. L., *Physiological reviews* 2015, *95* (4), 1205-40.
233. Boucher, E.; Mandato, C. A., *Biochimica et biophysica acta* 2015, *1853* (10 Pt A), 2649-61.
234. Abreu-Blanco, M. T.; Watts, J. J.; Verboon, J. M.; Parkhurst, S. M., *Cellular and molecular life sciences : CMLS* 2012, *69* (15), 2469-83.
235. Andrews, N. W.; Corrotte, M., *Current biology : CB* 2018, *28* (8), R392-r397.
236. Miyake, K.; McNeil, P. L.; Suzuki, K.; Tsunoda, R.; Sugai, N., *Journal of Cell Science* 2001, *114* (19), 3487-3494.
237. Pu, F.; Chen, N.; Xue, S., *Food Science and Human Wellness* 2016, *5* (1), 8-16.
238. Dvorak, M. M.; Siddiqua, A.; Ward, D. T.; Carter, D. H.; Dallas, S. L.; Nemeth, E. F.; Riccardi, D., *Proceedings of the National Academy of Sciences of the United States of America* 2004, *101* (14), 5140-5.
239. Liu, Z.; Han, X.; Zhou, Q.; Chen, R.; Fruge, S.; Jo, M. C.; Ma, Y.; Li, Z.; Yokoi, K.; Qin, L., *Adv Biosyst* 2017, *1* (6).
240. Walski, T.; Chludzinska, L.; Komorowska, M.; Witkiewicz, W., *BioMed research international* 2014, *2014*, 162102.
241. Rao, W.; Huang, H.; Wang, H.; Zhao, S.; Dumbleton, J.; Zhao, G.; He, X., *ACS applied materials & interfaces* 2015, *7* (8), 5017-28.
242. Hammerick, K. E.; Huang, Z.; Sun, N.; Lam, M. T.; Prinz, F. B.; Wu, J. C.; Commons, G. W.; Longaker, M. T., *Tissue Eng Part A* 2011, *17* (3-4), 495-502.
243. Hunt, C. J., *Transfus Med Hemother* 2011, *38* (2), 107-123.
244. Wang, Y.; Yin, P.; Bian, G. L.; Huang, H. Y.; Shen, H.; Yang, J. J.; Yang, Z. Y.; Shen, Z. Y., *Stem Cell Res Ther* 2017, *8* (1), 194.
245. Ude, C. C.; Miskon, A.; Idrus, R. B. H.; Abu Bakar, M. B., *Mil Med Res* 2018, *5* (1), 7.
246. Mahla, R. S., *Int J Cell Biol* 2016, *2016*, 6940283.
247. Sykova, E.; Forostyak, S., *Laser Ther* 2013, *22* (2), 87-92.
248. Jin, Y. Z.; Lee, J. H., *Clin Orthop Surg* 2018, *10* (3), 271-278.
249. Lee, S.; Kwon, T.; Chung, E. K.; Lee, J. W., *Biomater Res* 2014, *18*, 11.
250. Hanna, J.; Hubel, A., *Organogenesis* 2009, *5* (3), 134-7.
251. Wang, Y.; Han, Z. B.; Song, Y. P.; Han, Z. C., *Stem Cells Int* 2012, *2012*, 652034.

252. Waters, R.; Alam, P.; Pacelli, S.; Chakravarti, A. R.; Ahmed, R. P. H.; Paul, A., *Acta Biomater* 2018, *69*, 95-106.
253. Froelich, K.; Mickler, J.; Steusloff, G.; Technau, A.; Ramos Tirado, M.; Scherzed, A.; Hackenberg, S.; Radeloff, A.; Hagen, R.; Kleinsasser, N., *Cytotherapy* 2013, *15* (7), 767-81.
254. Pan, Q.; Fouraschen, S. M.; de Ruiter, P. E.; Dinjens, W. N.; Kwekkeboom, J.; Tilanus, H. W.; van der Laan, L. J., *Experimental biology and medicine (Maywood, N.J.)* 2014, *239* (1), 105-15.
255. Capelli, C.; Pedrini, O.; Cassina, G.; Spinelli, O.; Salmoiraghi, S.; Golay, J.; Rambaldi, A.; Giussani, U.; Introna, M., *Haematologica* 2014, *99* (6), e94-7.
256. Izadpanah, R.; Kaushal, D.; Kriedt, C.; Tsien, F.; Patel, B.; Dufour, J.; Bunnell, B. A., *Cancer Res* 2008, *68* (11), 4229-38.
257. Jang, T. H.; Park, S. C.; Yang, J. H.; Kim, J. Y.; Seok, J. H.; Park, U. S.; Choi, C. W.; Lee, S. R.; Han, J., *Integr Med Res* 2017, *6* (1), 12-18.
258. Motta, J. P.; Paraguassu-Braga, F. H.; Bouzas, L. F.; Porto, L. C., *Cryobiology* 2014, *68* (3), 343-8.
259. Eroglu, A.; Russo, M. J.; Bieganski, R.; Fowler, A.; Cheley, S.; Bayley, H.; Toner, M., *Nat Biotechnol* 2000, *18* (2), 163-7.
260. Zhang, M.; Oldenhof, H.; Sieme, H.; Wolkers, W. F., *Biochimica et biophysica acta* 2016, *1858* (6), 1400-9.
261. Pancrazio, J. J.; Wang, F.; Kelley, C. A., *Biosens Bioelectron* 2007, *22* (12), 2803-11.
262. Ntai, A.; La Spada, A.; De Blasio, P.; Biunno, I., *Stem Cell Res* 2018, *31*, 102-112.
263. Szurek, E. A.; Eroglu, A., *PLoS One* 2011, *6* (11), e27604.
264. de Abreu Costa, L.; Henrique Fernandes Ottoni, M.; Dos Santos, M. G.; Meireles, A. B.; Gomes de Almeida, V.; de Fatima Pereira, W.; Alves de Avelar-Freitas, B.; Eustaquio Alvim Brito-Melo, G., *Molecules* 2017, *22* (11).
265. Best, B. P., *Rejuvenation Res* 2015, *18* (5), 422-36.
266. Chetty, S.; Pagliuca, F. W.; Honore, C.; Kweudjeu, A.; Rezania, A.; Melton, D. A., *Nat Methods* 2013, *10* (6), 553-6.
267. Perotti, C.; Fante, C. D.; Viarengo, G.; Parisi, C.; Marchesi, A.; Bergamaschi, P.; Salvaneschi, L., *Blood* 2006, *108* (11), 5213-5213.
268. Chen, C.; Sharma, S.; Doo, H.; Reynafarje, A.; Jallilzeinali, B.; Shore, T. B.; Schuster, M. W., *Blood* 2004, *104* (11), 4998-4998.
269. Berz, D.; McCormack, E. M.; Winer, E. S.; Colvin, G. A.; Quesenberry, P. J., *Am J Hematol* 2007, *82* (6), 463-72.
270. Zhang, M.; Oldenhof, H.; Sydykov, B.; Bigalk, J.; Sieme, H.; Wolkers, W. F., *Scientific Reports* 2017, *7* (1), 6198.
271. Stewart, S.; He, X., *Langmuir* 2018, *35* (23):7414-22
272. Zhang, W.; Rong, J.; Wang, Q.; He, X., *Nanotechnology* 2009, *20* (27), 275101.
273. Oliver, A. E.; Jamil, K.; Crowe, J. H.; Tablin, F., *Cell Preservation Technology* 2004, *2* (1), 35-49.
274. Abazari, A.; Meimetis, L. G.; Budin, G.; Bale, S. S.; Weissleder, R.; Toner, M., *PLoS One* 2015, *10* (6), e0130323.
275. Wolkers, W. F.; Tablin, F.; Crowe, J. H., *Comp Biochem Physiol A Mol Integr Physiol* 2002, *131* (3), 535-43.
276. Eroglu, A.; Lawitts, J. A.; Toner, M.; Toth, T. L., *Cryobiology* 2003, *46* (2), 121-134.
277. Bailey, S. E.; Eroglu, A.; Toner, M.; Toth, T. L., *Biology of Reproduction* 2009, *80* (1), 70-78.
278. Eroglu, A.; Toner, M.; Toth, T. L., *Fertility and Sterility* 2002, *77* (1), 152-158.
279. Uchida, T.; Furukawa, M.; Kikawada, T.; Yamazaki, K.; Gohara, K., *Cryobiology* 2017, *77*, 50-57.
280. Guo, N.; Puhlev, I.; Brown, D. R.; Mansbridge, J.; Levine, F., *Nat Biotechnol* 2000, *18* (2), 168-71.
281. Kay, M. A., *Nature Reviews Genetics* 2011, *12*, 316.
282. Sharp, D. M. C.; Picken, A.; Morris, T. J.; Hewitt, C. J.; Coopman, K.; Slater, N. K. H., *Cryobiology* 2013, *67* (3), 305-311.

283. Lynch, A. L.; Chen, R.; Dominowski, P. J.; Shalaev, E. Y.; Yancey, R. J.; Slater, N. K. H., *Biomaterials* 2010, *31* (23), 6096-6103.
284. Mercado, S. A.; Slater, N. K. H., *Cryobiology* 2016, *73* (2), 175-180.
285. Wei, Y.; Li, C.; Zhang, L.; Xu, X., *Biochimica et biophysica acta* 2014, *1838* (7), 1911-20.
286. Holovati, J. L.; Gyongyossy-Issa, M. I. C.; Acker, J. P., *Cell Preservation Technology* 2008, *6*, 131.
287. Zhang, S.; Fan, J.; Xu, X.; Chen, G.; Zhu, F.; Yan, L., *Cryobiology* 2009, *59* (2), 135-140.
288. Shirakashi, R.; Köstner, C. M.; Müller, K. J.; Kürschner, M.; Zimmermann, U.; Sukhorukov, V. L., *Journal of Membrane Biology* 2002, *189* (1), 45-54.
289. Dovgan, B.; Barlic, A.; Knezevic, M.; Miklavcic, D., *J Membr Biol* 2017, *250* (1), 1-9.
290. Crowe, J. H.; Crowe, L. M.; Chapman, D., *Science (New York, N.Y.)* 1984, *223* (4637), 701-3.
291. Crowe, J. H.; Leslie, S. B.; Crowe, L. M., *Cryobiology* 1994, *31* (4), 355-66.
292. Eroglu, A.; Toner, M.; Toth, T. L., *Fertil Steril* 2002, *77* (1), 152-8.
293. Turner, C. E., *Nature Cell Biology* 2000, *2* (12), E231-E236.
294. Verseijden, F.; Jahr, H.; Posthumus-van Sluijs, S. J.; Ten Hagen, T. L.; Hovius, S. E.; Seynhaeve, A. L.; van Neck, J. W.; van Osch, G. J.; Hofer, S. O., *Tissue Eng Part A* 2009, *15* (2), 445-52.
295. Rehman, J.; Traktuev, D.; Li, J.; Merfeld-Clauss, S.; Temm-Grove Constance, J.; Bovenkerk Jason, E.; Pell Carrie, L.; Johnstone Brian, H.; Considine Robert, V.; March Keith, L., *Circulation* 2004, *109* (10), 1292-1298.
296. Lynch, A. L.; Chen, R.; Slater, N. K. H., *Biomaterials* 2011, *32* (19), 4443-4449.
297. Ding, X.; Stewart, M.; Sharei, A.; Weaver, J. C.; Langer, R. S.; Jensen, K. F., *Nat Biomed Eng* 2017, *1*.
298. Agarwal, J.; Walsh, A.; Lee, R. C., *Ann N Y Acad Sci* 2005, *1066*, 295-309.
299. Stewart, M. P.; Sharei, A.; Ding, X.; Sahay, G.; Langer, R.; Jensen, K. F., *Nature* 2016, *538* (7624), 183-192.

APPENDIX A: Supplementary figures

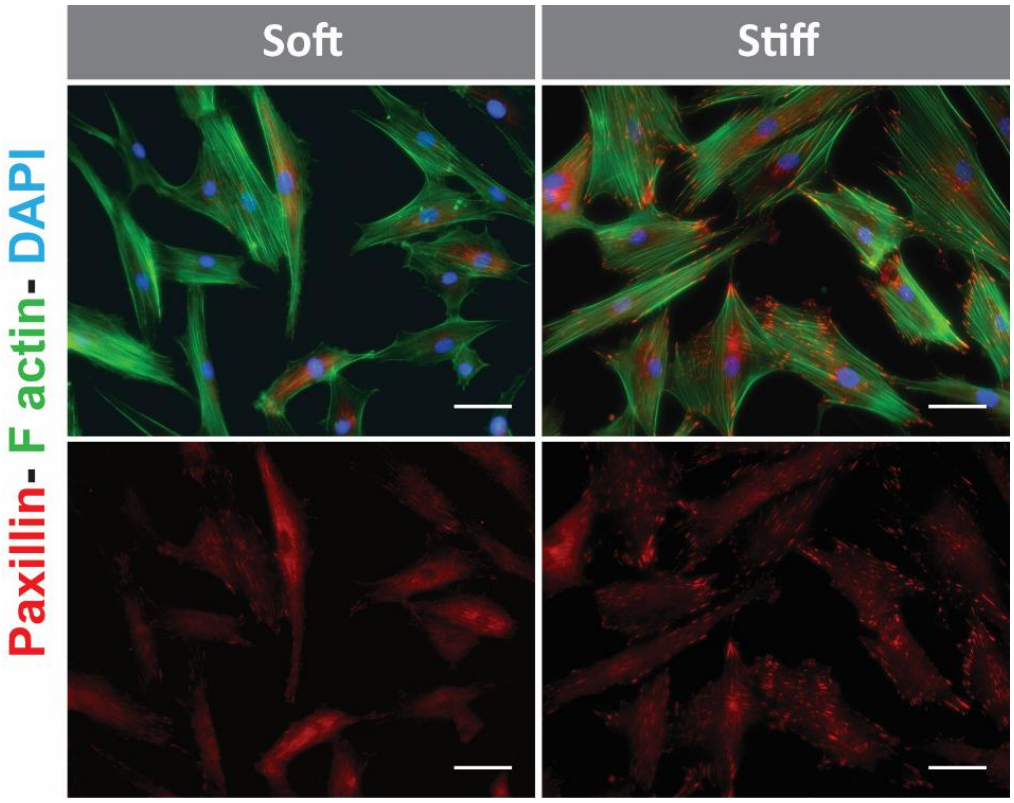

Figure S2.1 Immunofluorescence staining of hASCs seeded on soft (0.5 kPa) and stiff (32 kPa) substrates. Cells were stained with Alexa Fluor 488 Phalloidin to visualize actin stress fibers (green) and with Diamidino-2-phenylindole dilactate (DAPI) to stain the nuclei (blue). In addition, paxillin staining (red) was carried out to identify the area of focal adhesion. Scale bar = 60 µm.

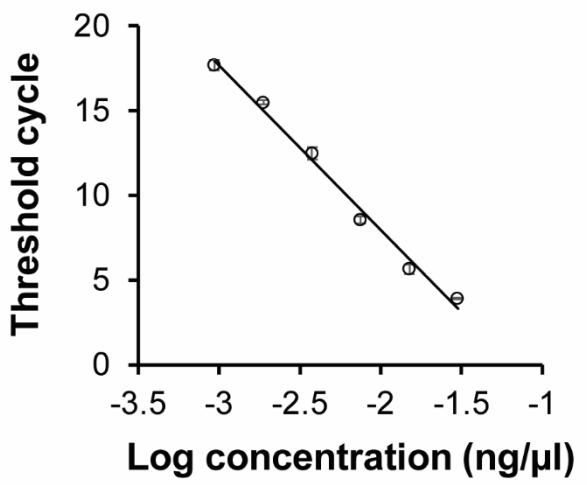

Figure S2.2 Calibration curve for plasmid internalization analyzed by qPCR. This curve was obtained by acquiring the corresponding threshold cycle for different concentration of GFP plasmid (0.9 ng to 30 ng) in the cell lysates.

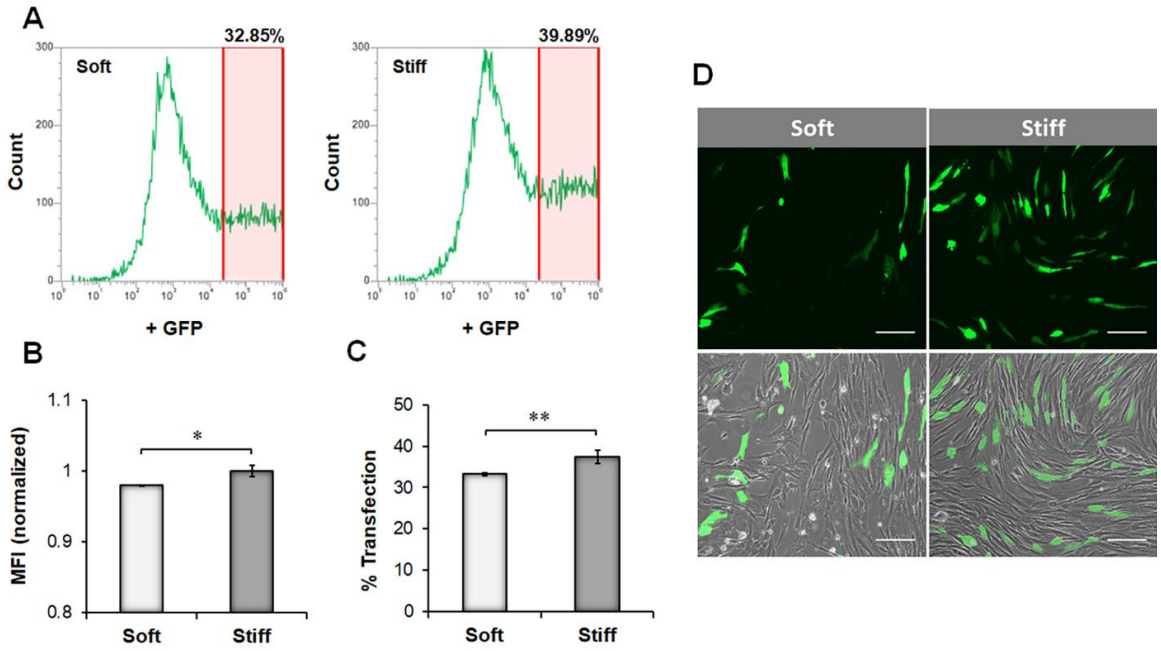

Figure S2.3 Effect of substrate stiffness on green fluorescent protein (GFP) expression on hASCs upon transfection with Lipofectamine2000®. A) FACs analysis of hASCs seeded on the two different substrates after being transfected with GFP plasmid. The population of GFP positive cells are indicated on the graph (pink area). B) Quantification of mean fluorescence intensity (MFI) of GFP positive hASCs obtained using FACs analysis. C) Percentage of transfected cells obtained by analyzing FACs data. Results are reported as mean ± standard deviation (n = 3) * = $p < 0.05$, ** = $p < 0.01$. D) Fluorescent images and corresponding phase contrast images of hASCs expressing GFP after 24 hours of transfection. Scale bar = 200 µm.

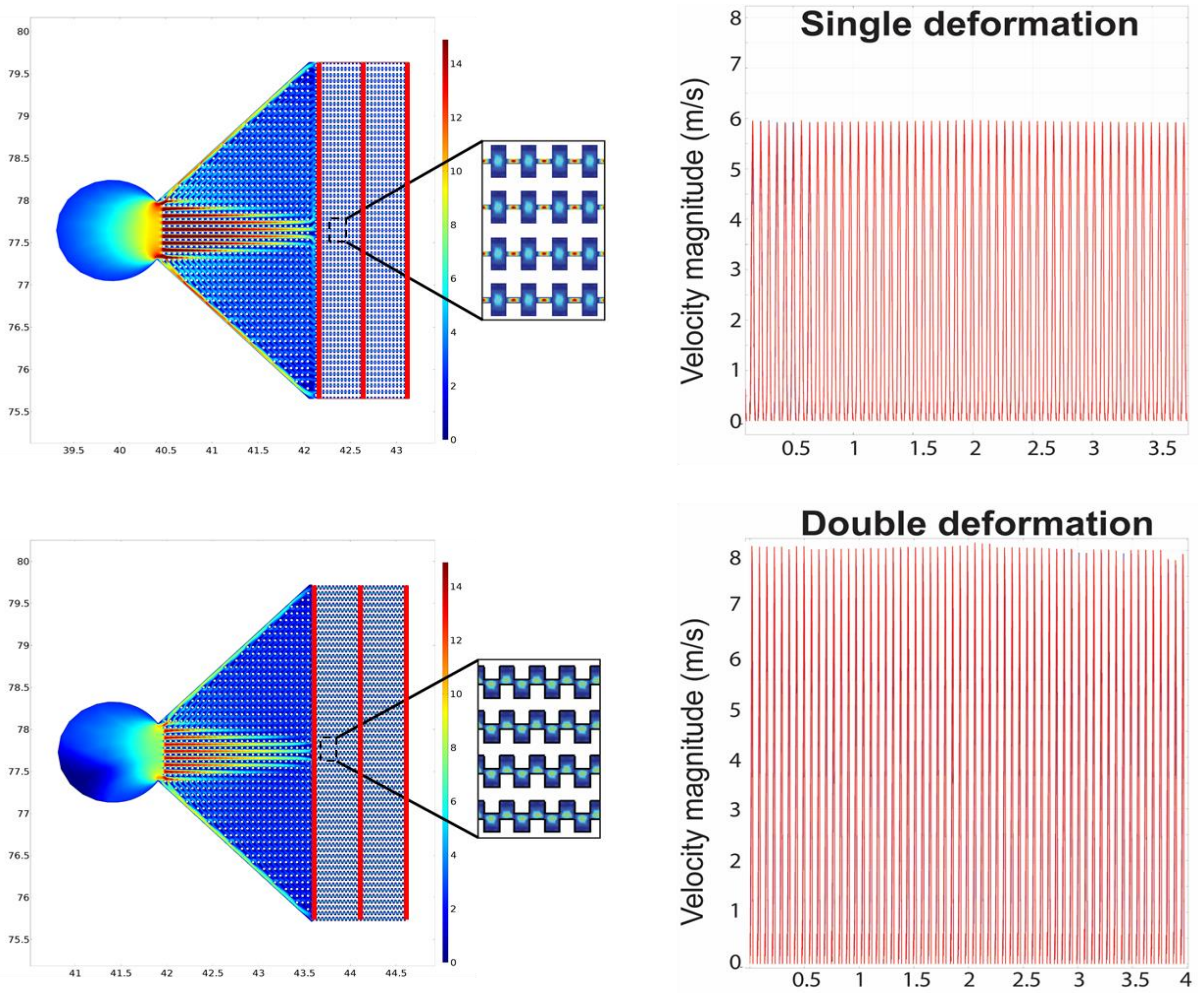

Figure S3.1. COMSOL simulations of flow velocity in every channel of both single and double deformation devices. Insets show the uniform distribution of the fluid velocity in the channels for both devices. On the right, line graphs of the velocity magnitude along the three cross-sections across the length of the device were plotted. The velocities remained the same throughout the tunnel.

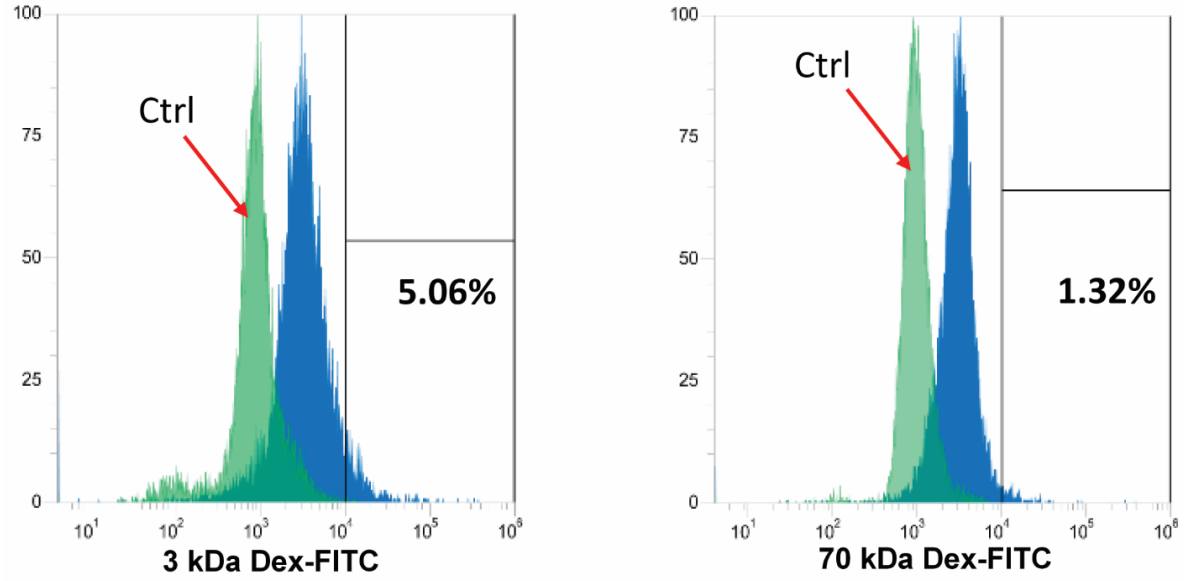

Figure S3.2 Flow cytometry analysis displaying endocytosis of Dex-FITC in hASCs. hASCs were treated with A) 3 kDa Dex-FITC and B) 70 kDa Dex-FITC. 150 µL of a trypan blue 0.4% w/v solution was added to the cell suspension to quench the extracellular fluorescence of Dex-FITC.

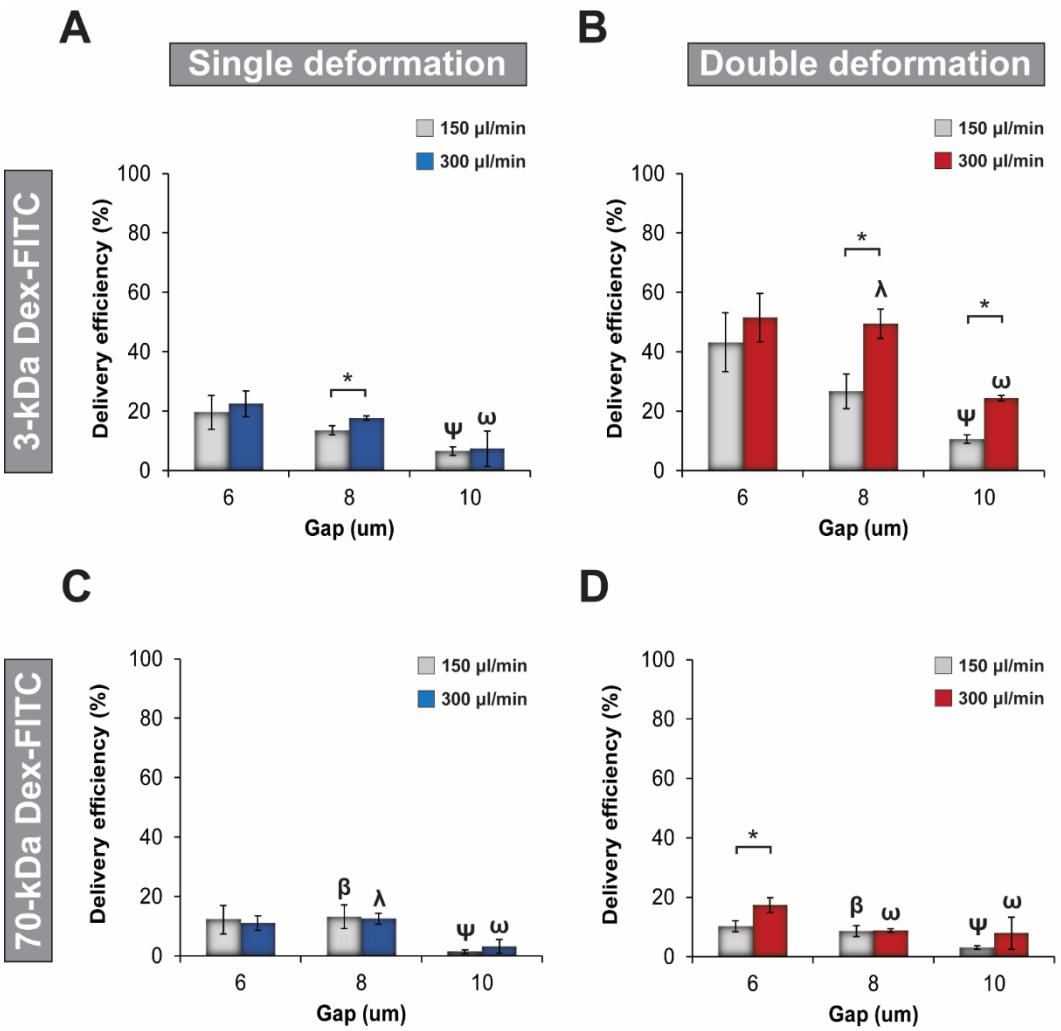

Figure S3.3 Effect of gap size, flow rates, and geometry (single and double deformation) on the internalization of Dex-FITC into fibroblasts. A) and B) Delivery efficiency of Dex-FITC (3 kDa) in fibroblasts using single and double deformation, respectively. Three different gaps (6, 8 and 10 µm) and two different flow rates (150 µL/min and 300 µL/min) were tested for each design. C) and D) Delivery efficiency of Dex-FITC (70 kDa) using single and double deformation, respectively. A decrease in the percentage of positive fluorescent fibroblasts was found in all the gaps tested compared to the results reported for Dex-FITC 3 kDa. Results are reported as mean ± deviation standard (n =3). ψ and ω are used to indicate a significant change in delivery compared to gap 6 for the other two gaps at the flow rate of 150 µL/min and 300 µL/min, respectively ($p<0.05$). β and λ are used to indicate a significant change in delivery compared to gap 8 for gap 10 at the flow rate of 150 µL/min and 300 µL/min, respectively ($p<0.05$). * indicates significance between two different flows for the same gap ($p<0.05$).

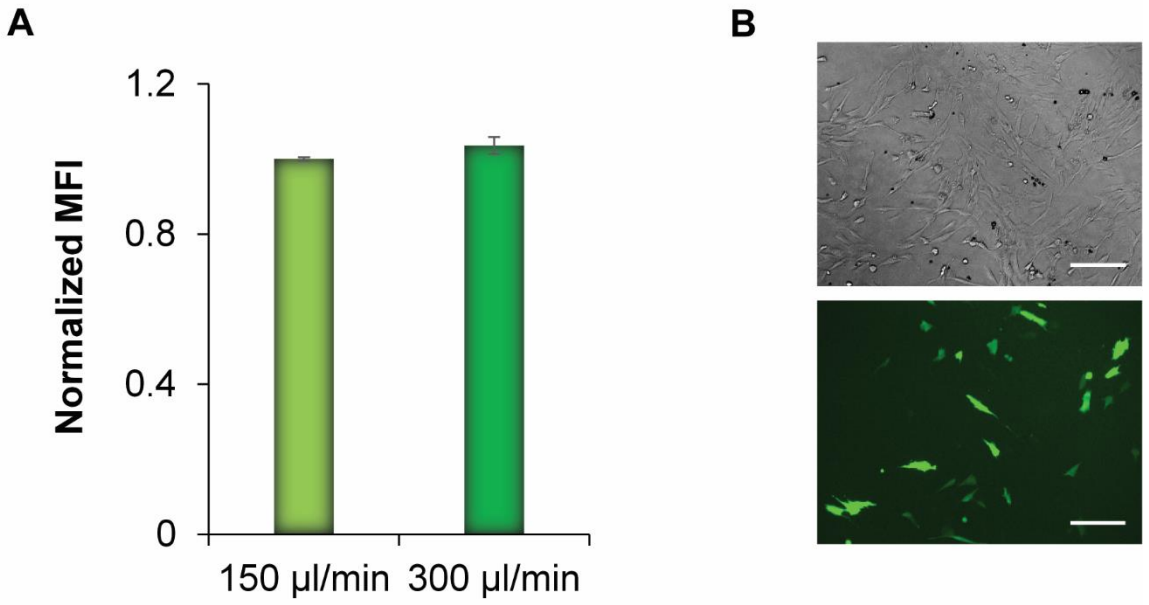

Figure S3.4 Green fluorescent protein (GFP) transfection of hASCs using the optimized microfluidic device. A) Normalized mean fluorescent intensity (MFI) of hASCs analyzed by flow cytometry. No significant difference in MFI values were observed between low (150 µl/min) and high (300 µl/min) flow rates. B) Phase contrast (top) and corresponding fluorescent image of hASCs (bottom) after 24 hours of transfection with GFP. Scale bar = 200 µm.

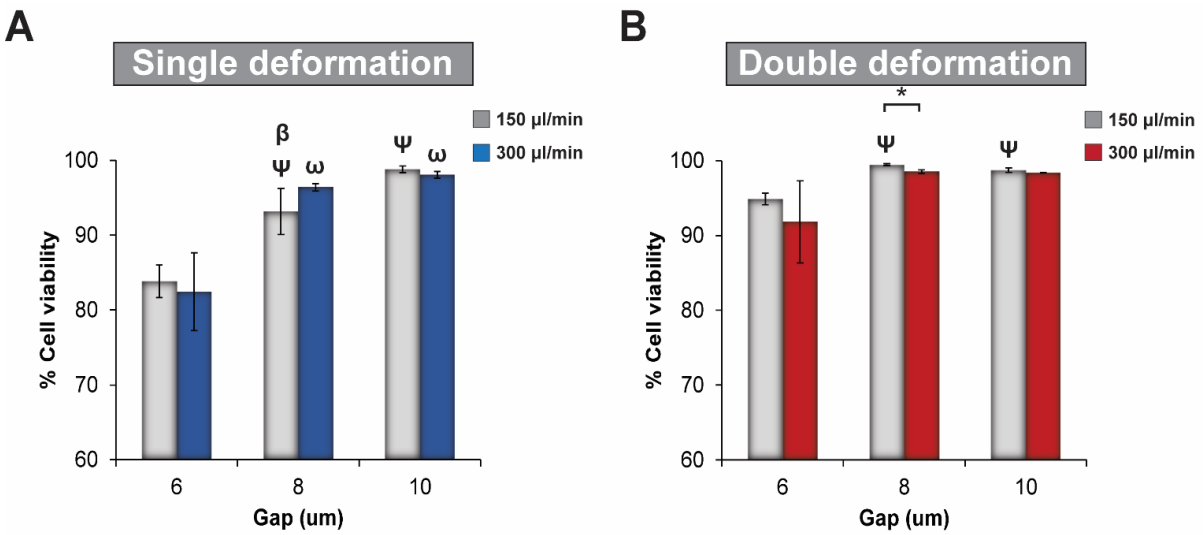

Figure S3.5 Effect of gap size, flow rates, and geometry design on the viability of fibroblasts passing through the microfluidic device. A) and B) Percentage of cell viability obtained after passing the cells through the single and the double deformation design, respectively. Similar to the delivery efficiency tests, three different gaps (6, 8 and 10 µm), and two different flow rates (150 µL/min and 300 µL/min) were tested for each design. Results are reported as mean ± deviation standard (n =3). ψ and ω are used to indicate a significant increase in cell viability compared to gap 6 for the other two gaps at a flow rate of 150 µL/min and 300 µL/min, respectively ($p<0.05$). β and λ are used to indicate a significant increase in cell viability compared to gap 8 for gap 10 at the flow rate of 150 µL/min and 300 µL/min, respectively ($p<0.05$). * indicates significance between two different flows for the same gap ($p<0.05$).

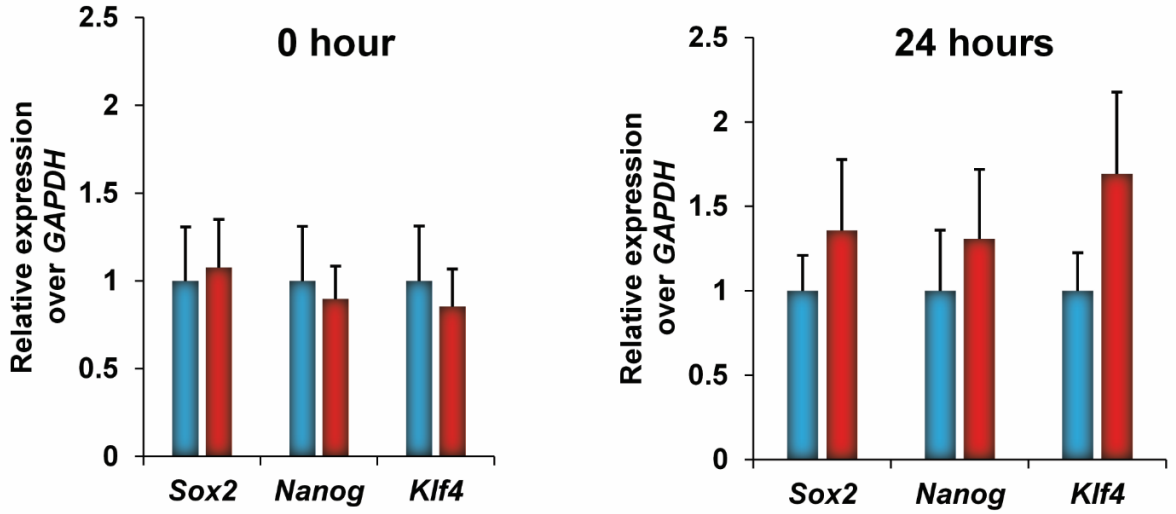

Figure S3.6 Relative expression of stemness genes (*Sox2*, *Nanog*, *Klf4*) over *GAPDH* in hASCs. The qPCR analysis was carried out on the cells squeezed through the microfluidic device (red bars) and compared to hASCs untreated (blue bars). The gene expression was monitored immediately after the process of deformation and 24 hours post-treatment. No significant difference in gene expression was observed at 0 and 24 hours between the two groups tested (n=3).

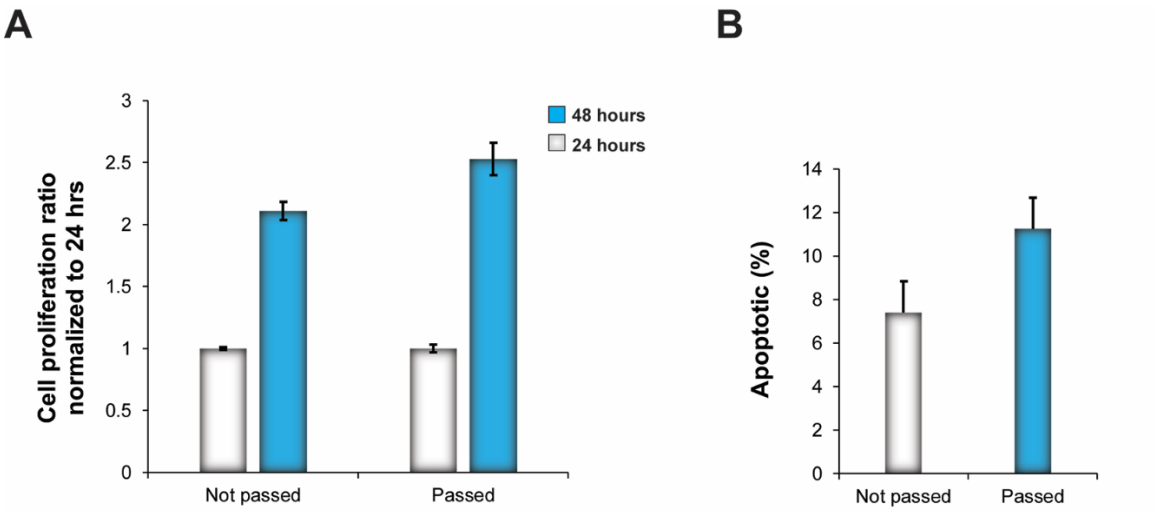

Figure S4.1 Assessment of cell viability and apoptosis of hASCs after being squeezed in the optimized microfluidic device. A) MTS analysis of the cell proliferation rate of hASCs after passing through the microfluidic device (passed) compared to untreated hASCs (not passed) Results were normalized based on the cell number obtained at 24 hours B) Quantification of apoptotic cells by flow cytometry analysis of hASCs after being passed through the microfluidic device The results were compared to untreated hASCs (not passed). (n=3). * = $p < 0.05$ ** = $p < 0.01$, and *** $p < 0.001$.

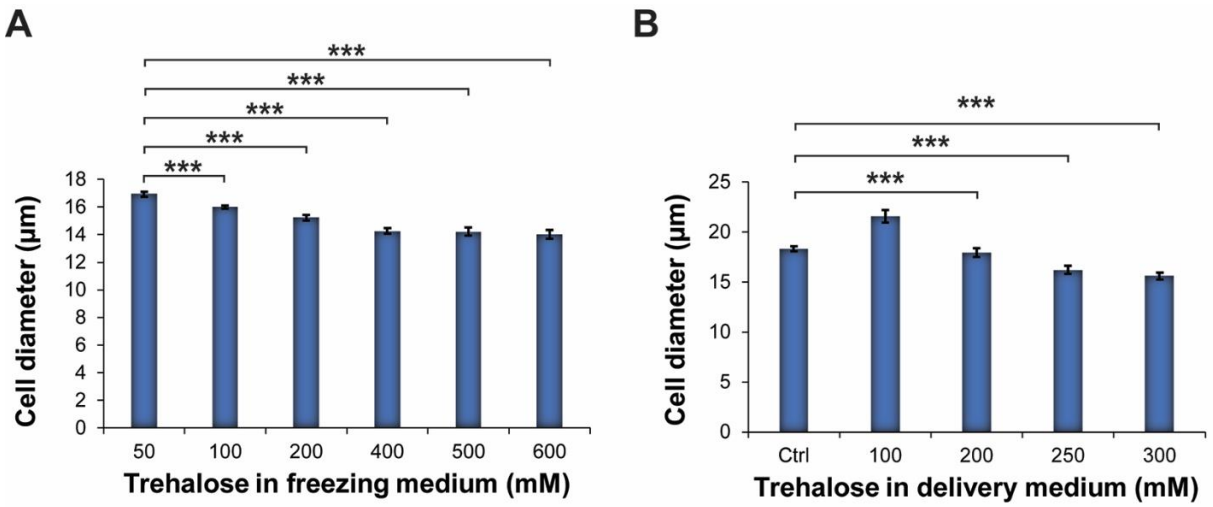

Figure S4.2 Cell diameter measurements in different concentrations of trehalose A) Cell diameter measurements of hASCs exposed to freezing media supplemented with different concentrations of trehalose ranging from 50 to 600 mM. B) Cell diameter measurements of hASCs exposed to phosphate buffer (10 mM K_2HPO_4, 10 mM KH_2PO_4 and 1 mM $MgCl_2$) supplemented with different concentrations of trehalose varying from 0 to 300 mM. Results are reported as mean ± standard deviation (n=9). * = $p < 0.05$ ** = $p < 0.01$, and *** $p < 0.001$.

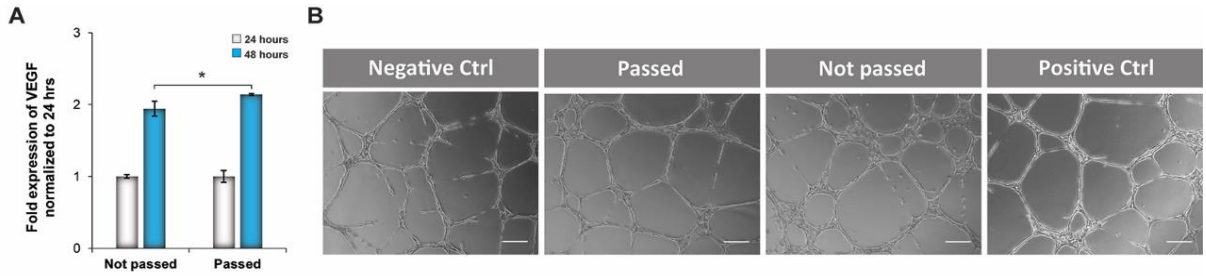

Figure S4.3 Evaluation of the angiogenic potential of hASCs after squeezing. A) Fold expression of VEGF secretion after 48 hours normalized to the amount of growth factor produced after 24 hours of culture. The two groups tested are hASCs passed and not passed through the microfluidic device. Results are reported as mean ± standard deviation (n=3). * = $p < 0.05$ ** = $p < 0.01$, and *** $p < 0.001$. B) Bright-field images of HUVECs cultured on Matrigel and treated with different types of secretome derived from hASCs passed and not passed through the microfluidic device. The negative control group was represented by endothelial cells cultured without any angiogenic growth factor. Scale bars = 400 µm.

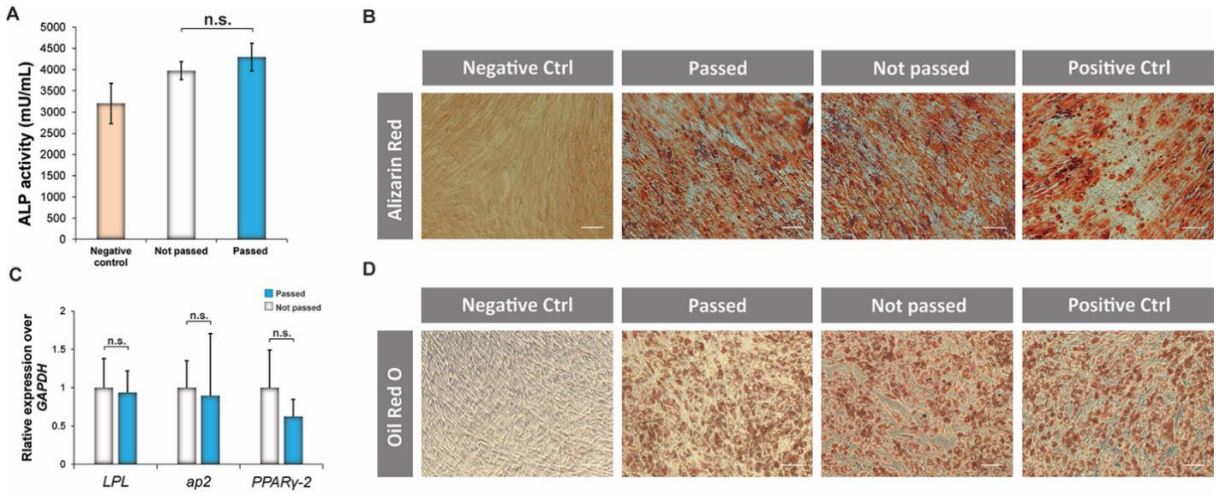

Figure S4.4 Assessment of osteogenic and adipogenic differentiation of hASCs after being squeezed in the optimized microfluidic device. A) Alkaline phosphatase quantification of hASCs for the different groups after 7 days of osteogenic differentiation. Scale bar = 200 μm. The results are reported as mean ± deviation standard (n=3). * = $p<0.05$, ** = $p<0.01$ *** = $p<0.001$. B) Alizarin red staining to detect the presence of intracellular deposits of calcium in the different groups after 14 days of osteogenic differentiation. C) qPCR analysis of *PPARγ-2*, *aP2*, *LPL* genes, which are commonly upregulated during the process of adipogenic differentiation of stem cells after 10 days. Results are reported as mean ± deviation standard (n=3). * = $p<0.05$, ** = $p<0.01$ *** = $p<0.001$. D) Oil Red O staining of hASCs differentiated in the adipogenic medium after 10 days to visualize the presence of intracellular lipid-filled droplets in hASCs passed through the microfluidic device compared to untreated cells.

APPENDIX B: TABLES

Table S2.1. Main genes regulating the process of Caveolin-mediated endocytosis

Genes	***Forward primer***	***Reverse primer***	***Role(s)***
CAV1 (Caveolin 1)	GACGTCGTCAAGGTAAGCCA	GTAACGTTTCTGCCGACTGC	Flask shaped protein essential for caveolae formation
CAVIN1	GCAATACGCTGAGCAAGCTG	CTGTGGGCTCACCTGGTAGAT	Regulator of caveolae formation
ABL1 (Abl tyrosin kinase)	CTCAGACGAAGTGGAAAAG	GAGTGAGGCATCTCAGG	Responsible for actin polymerization to form stress fibers and organization of CAV1 linked to these fibers
FLNA (Filamin A)	TAAGGTTACTGTGCTCTTTG	AAGATCTCAAAGTAGGTGGTC	Key factor for the interplay between actin and CAV1
ITGB1 (β1 integrin)	ATTCCCTTTCCTCAGAAGTC	TTTTCTTCCATTTTCCCCTG	Mediator of microtubule stabilization and translocation of caveolae within the cytoskeletal system
DIAPH1 (Diaphanous Related Formin 1)	ATTTCAGTCCAGGTGGTTGC	GTGAGGCAGGTGCTTTCTTC	Cooperate with ABL1 along with local stabilization of microtubules
RHOA (Ras Homolog Family Member A)	AGGAAGATTATGATCGCCTG	TTCTAAACTATCAGGGCTGTC	Regulator of the link between caveolae and actin stress fibers

Table S2.2 Main genes regulating the process of Clathrin-mediated endocytosis.

Genes	***Forward primer***	***Reverse primer***	***Role(s)***
CLTC (Clathrin)	TAAAGTGTTTCCCCCTGCTGCAC	GCTGGTCTCTCAACCAAAGC	Main component of clathrin triskelion formation
SNX9	GGAATGGAAAACTGGAAAGAG	TCTACTAAGTCCAAGTCAGG	Involved in clathrin-coated vesicle budding and formation of the clathrin neck
EPS15	AAGGTCAACAATGAAGATCC	GACCGATGTTTCCTCAAATAC	A scaffolding protein, Involved in clathrin recruitment
EPN1 (Epsin)	GTTTACAAGGCCATGACG	CTTAGCTTTCTCACGCAC	An accessory protein which mediates clathrin binding to cell membrane and cargo receptors

Table S3.1 Comparison of the percentage of 3-kDa Dex-FITC delivery in hASCs for single and double deformation designs

	Flow rate (Low)			**Flow rate (High)**		
Design	**Single deformation**	**Double deformation**	***p-value***	**Single deformation**	**Double deformation**	***p-value***
Gap 6 µm	62.28 ± 5.26	68.92 ± 1.18	0.099	71.94 ± 3.01	74.38 ± 2.2	0.32
Gap 8 µm	59.28 ± 6.84	71.14 ± 4.21	0.062	61.26 ± 3.99	84.28 ± 1.63	0.0008*
Gap 10 µm	20.68 ± 8.19	47.21 ± 11.19	0.0296*	28.07 ± 6.96	49.28 ± 17.06	0.1169

Table S3.2. Comparison of the percentage of 70 kDa Dex-FITC delivery in single and double deformation designs

	Flow rate (Low)			**Flow rate (High)**		
Design	**Single deformation**	**Double deformation**	***p*-value**	**Single deformation**	**Double deformation**	***p*-value**
Gap 6 µm	35.28 ± 5.53	38.79 ± 7.19	0.5394	42.24 ± 5.2	55.19 ± 2.15	0.0163*
Gap 8 µm	22.08 ± 5.02	23.49 ± 3.21	0.7029	36.58 ± 7.89	40.53 ± 4.85	0.5011
Gap 10 µm	4.41 ± 1.83	6.99 ± 2.9	0.2625	8.13 ± 1.18	18. 62 ± 5.85	0.0382*

Table S3.3 Percentage of cell viability in all the groups by comparing single and double deformation designs

	Flow rate (Low)			Flow rate (High)		
Design	**Single deformation**	**Double deformation**	***p*-value**	**Single deformation**	**Double deformation**	***p*-value**
Gap 6 µm	86.03 ± 8.18	81.87 ± 3.06	0.4557	71.16 ± 8.5	82.96 ± 4.66	0.1027
Gap 8 µm	93.63 ± 4.07	90.38 ± 2.18	0.2897	89.72 ± 3.54	83.58 ± 3.58	0.1022
Gap 10 µm	97.42 ± 0.68	98.21 ± 0.37	0.1519	96.70 ± 0.48	96.11 ± 1.84	0.6195